CIRCUIT QUANTUM ELECTRODYNAMICS *(cQED)* HYBRID SYSTEMS *for* QUANTUM TECHNOLOGY APPLICATIONS: *A Theoretical Study.*

A Thesis submitted for the Degree of

DOCTOR *of* PHILOSOPHY

by

Roson Nongthombam

Thesis Supervisor
Prof. Amarendra Kumar Sarma

Department of physics
Indian Institute of Technology, Guwahati
Assam-781039
India

CIRCUIT QUANTUM ELECTRODYNAMICS *(cQED)* HYBRID SYSTEMS *for* QUANTUM TECHNOLOGY APPLICATIONS: *A Theoretical Study.*

A Thesis submitted in Partial Fulfilment of the Requirements for the Degree of

DOCTOR *of* PHILOSOPHY

by

Roson Nongthombam

Thesis Supervisor
Prof. Amarendra Kumar Sarma

Department of physics
Indian Institute of Technology, Guwahati
Assam-781039
India

Dedicated to my parents.

Declaration

Roson Nongthombam
Roll No. 196121025
Department of Physics
IIT Guwahati
Guwahati, India.
n.roson@iitg.ac.in

I hereby declare that works presented in the thesis entitled "*Circuit Quantum Electrodynamics (cQED) Hybrid Systems for Quanutm Technological Applications: A Theoretical Study*" has been carried out by me under the supervision of Prof. Amarendra Kumar Sarma at the Department of Physics, Indian Institute of Technology Guwahati, India. The thesis has not been submitted anywhere else for any degree. Works presented in the thesis are all my own unless referenced to the contrary in the thesis.

Roson Nongthombam

Date: 18-10-2024

Disclaimer

The bibliography included in this thesis is by no means complete; however, it contains the sources that I consulted thoroughly. I apologize for inadvertently omitting some research papers, review articles, and other relevant scientific documents that should also have been cited.

-Roson Nongthombam

Certificate

Prof. Amarendra Kumar Sarma
Department of Physics
IIT Guwahati
Guwahati, India.
aksarma@iitg.ac.in

It is certified that the work contained in the thesis entitled "*Circuit Quantum Electrodynamics (cQED) Hybrid Systems for Quanutm Technological Applications: A Theoretical Study*" by Mr. Roson Nongthombam (Roll No - 196121025), a Ph.D. student in the Department of Physics, Indian Institute of Technology Guwahati is carried out under my supervision and has not been submitted elsewhere for the award of any other degree.

Prof. Amarendra Kumar Sarma

Date: 18-10-2024

Acknowledgement

I would like to first express my sincere gratitude to my PhD advisor, Prof. Amarendra Kumar Sarma, for providing me with unwavering guidance, consistent support, and valuable feedback throughout my research. I would also like to express my appreciation for his encouragement in tackling problems with an open mind, as well as for granting me the freedom to explore new areas during my PhD tenure.

I acknowledge my doctoral committee, Dr. Pankaj Kumar Mishra, Dr. Kanhaiya Panday and Dr. Shrikrishna N Joshi , for their constructive criticism, encouragement, and insightful comments, which have helped me deepen my understanding of various intricacies. I also acknowledge the support, guidance, and advice I received from the Heads of the Department, all faculty members and staff members throughout my doctoral journey.

I am grateful to have met my seniors - Monika, Ambaresh, Dipti, Subhadeep, Jyoti, and Abdelsalam - and will always be indebted to them for their support, guidance, and insightful discussions. I extend my heartfelt gratitude to my fellow group members, Sampreet, Pooja, Alolika, Urmimala and Gaurav, for their engaging support and collaboration throughout my research. The cherished moments we shared, especially the discussions and laughter at Khokha and at the food court, made this journey both enjoyable and memorable. I wish to extend my heartfelt thanks to my friends whom I met through my passion for football. Competing as a team in the inter-department tournament, where we secured the runner-up position, and in the open tournament, where we became champions, is an experience I will always cherish. I am also truly grateful to all my jigris for being a part of this journey. The emotional roller coaster we experienced together, filled with ups and downs, truly shaped our time together. From our passionate arguments to our moments of agreement, every discussion was a testament to our friendship. Thank you all for being there every step of the way.

Lastly, I would like to extend my deepest gratitude to my parents for their unwavering love and support.Their keep-on-going attitude has been a constant source of motivation, inspiring me to persevere through challenges. I am truly fortunate to have such loving and supportive parents, and I owe my achievements to their sacrifices and encouragement.

Abstract

In this thesis, we study various quantum phenomena and their applications in a hybrid system implemented on a circuit quantum electrodynamics (cQED) platform. cQED explores the interaction between nonlinear superconducting circuits—functioning as artificial atoms—and quantized electromagnetic fields in the microwave-frequency range. The artificial atom in these circuits is realized through a Josephson tunnel junction, formed by a thin insulating barrier at the interface between two superconductors. The non-linear properties of this junction transform the equally spaced energy levels of a simple LC harmonic oscillator into atomic-like energy levels that are unequally spaced. A notable feature of this artificial atom is its ability to tune the frequency of its energy levels by driving it with a microwave field. In this study, we couple the artificial atom, also known as a superconducting qubit, with various quantum systems to form hybrid quantum systems. We have explored two such hybrid systems. First, we integrate quantum nanomechanical resonators—available in various shapes and sizes—into the superconducting circuit to create a hybrid electro-mechanical system. These resonators couple with the qubit capacitively or inductively, depending on their type. Using this hybrid system, we have generated bipartite cat states of two phononic crystal resonators remotely and performed the CHSH Bell test on these resonators. Next, we incorporate an optical cavity into the hybrid electro-mechanical system, allowing it to interact with the mechanical resonator and thus forming a hybrid electro-optomechanical system. In this configuration, the mechanical resonator interacts with the cavity via the radiation-pressure force from the cavity photons. Here, we investigate ground state cooling of the resonator through the qubit and optical cavity, quantum transduction of qubit information to optical photons, and synchronization of the optical field with the qubit.

List of Publications

Journal Publications

1. **Roson Nongthombam**, Ambaresh Sahoo, and Amarendra K. Sarma. *'Ground-state cooling of a mechanical oscillator via a hybrid electro-optomechanical system'* Phys. Rev. A **104**, 023509 (2021).

2. **Roson Nongthombam**, Sampreet Kalita, and Amarendra K. Sarma. *'Synchronization of a superconducting qubit to an optical field'* Phys. Rev. A **107**, 013528 (2023).

3. **Roson Nongthombam**, Pooja Kumari Gupta, and Amarendra K. Sarma. *'Quantum transduction of superconducting qubit in electro-optomechanical and electro-optomagnonical system'* Phys. Rev. A **108**, 043501 (2023).

4. **Roson Nongthombam**, Urmimala Dewan, and Amarendra K. Sarma. *'Generation of bipartite mechanical cat state by performing projective Bell state measurement.'*Phys. Rev. A **110**, 023726 (2024).

Symposium and Workshop Attended

1. Symposium on international day of light (IIT Guwahati), 16 May 2021.

2. Semiconductor Horizon Workshop (IIT Guwahati), 1 May 2024.

3. Symposium on international day of light (IIT Guwahati), 16 May 2023.

Contents

List of Figures

1 Introduction

1.1 Introduction

The demonstration of quantum phenomena like superposition and entanglement in macroscopic systems has greatly advanced quantum technology and information science. These effects, once limited to the microscopic realm, are now manipulated in larger systems. For example, quantum computers use superposition and entanglement for parallel computations, solving specific problems much faster than classical computers. Precise control and measurement of quantum states are crucial for these technologies, and superconducting qubits are well-suited for this purpose. Made by integrating Josephson junctions into superconducting circuits, they behave like artificial atoms due to their uneven energy levels. Superconducting qubits can be easily controlled and measured in a microwave cavity, leading to the development of circuit quantum electrodynamics (cQED). Since its emergence in the early 2000s [1–8], cQED has sparked significant interest in quantum information science, making superconducting qubits the frontrunners for practical quantum devices. Additionally, cQED is enabling research into hybrid quantum systems that integrate various physical systems—like nitrogen-vacancy centers [9, 10], mechanical oscillators [11], and quantum dots [12]—with superconducting circuits, thanks to the design flexibility and significant zero-point fluctuations within these circuits [13, 14].

A notable and rapidly developing hybrid cQED system is the quantum electromechanical system. In these systems, various mechanical resonators can be utilized, each offering distinct coupling mechanisms with qubits. For

instance, a suspended micromechanical or nanomechanical resonator, typically made of Al and operating at a few MHz, can couple to a superconducting qubit in two primary ways: First is capacitive coupling, where one end of the qubit's capacitor is replaced by the suspended resonator [15–19]. The other is inductive coupling, where one arm of a superconducting loop or SQUID (Superconducting Quantum Interference Device) loop is made movable out of plane [20–22] (see figure 1.4). The coupling in the first setup primarily arises from the qubit's charging energy, while the second arises from the flux inside the loop. These coupling types exhibit different characteristics: the former leads to transverse coupling, while the latter results in longitudinal coupling. Additionally, qubits can couple transversely to mechanical modes confined in a phononic crystal, which operate at higher frequencies in the GHz range, aligning well with qubit frequencies. These modes, whether surface acoustic or bulk acoustic, provide low-loss and high-quality phononic resonators [23–26]. One of the common methods for coupling involves a flip-chip architecture, where one chip hosts the qubit and another the resonator. The electric field from the qubit excites the resonator's bulk mode through a piezoelectric film deposited on the resonators chip or capacitively through a metallic electrode that connects qubit chip with the piezoelectric resonator chip through a vacuum gap capacitor [27–30] (see figure 1.4). The surface mode can also be excited in a similar manner using an inductive coupler instead of a capacitor [31]. The qubit-mechanical coupling can also be realized using a single chip with a piezoelectric resonator coupled via an interdigital transducer (IDT), a metallic electrode arranged in a comb like structure, which transfers the qubit's electric field to the resonator through its piezoelectric response [24, 32, 33]. The differences in the coupling nature of both the suspended membrane/drum and the phononic crystal with the qubit enable unique applications. For example, transverse coupling facilitates state swapping between the qubit and the resonator, leading to vacuum Rabi oscillations, whereas longitudinal coupling can be employed for cooling the resonator and exploring nonlinear effects. Additionally, by driving the qubit in the dispersive regime of transverse coupling, the phonon number distribution and parity measurement can be performed.

Another hybrid system, namely, electro-optomechanical system, can be realized by introducing an optical channel in the electromechanical system. For instance, a suspended nano- or micromechanical resonator can couple to an optical mode by forming a Fabry-Pérot optomechanical cavity, where the resonator acts as one end mirror [34–37]. In this configuration, the

coupling between the resonator and the cavity mode arises from the radiation pressure force exerted by the cavity photons on the resonator. Alternatively, optomechanical crystals [38, 40–44, 109] can be used to couple a qubit with the breathing mechanical mode of the crystal via an interdigital transducer (IDT), which generates surface acoustic waves (SAW) on either a piezoelectric or non-piezoelectric substrate using a piezoelectric film [45–47]. The SAW is guided toward the optomechanical crystal through a phononic waveguide, exciting the phononic mode. This excited phononic mode interacts with the optical mode confined in the crystal via the photoelastic effect. To enhance coupling between the mechanical and optical modes, optomechanical crystals are often fabricated from non-piezoelectric materials like silicon [48–51] (see figure 1.7). These systems are particularly useful for quantum transduction, where the qubit's state is transferred to long-lived optical photons—crucial for long-distance quantum communication and building extensive quantum networks.

In this thesis, we explore various applications of quantum phenomena within the two hybrid systems discussed above. We begin with a brief overview of their general dynamics, emphasizing their significance in quantum technological applications. In the following sections, we systematically implement and discuss the dynamics of these systems, starting with a simple lumped LC circuit.

1.2 Quantum LC Oscillator.

Consider a lumped LC oscillator circuit represented by the Hamiltonian

$$H = \frac{Q^2}{2C} + \frac{\Phi^2}{2L}. \tag{1.1}$$

This is analogous to a simple harmonic mechanical resonator with mass C, spring constant $1/L$, coordinate Φ, and momentum Q. The charge Q on the capacitor is related to the current I flowing in the circuit as $I = dQ/dt$ and the flux ϕ through the inductor is related to the voltage across it as $V = d\Phi/dt$. For a classical LC oscillator, the momentum and coordinate variables are related by the Poisson bracket $\{\Phi, Q\} = 1$. In the case of a quantum LC oscillator, the variables are promoted to operators, and their

relationship is given by the commutation relation $[\hat{\Phi}, \hat{Q}] = i\hbar$.

$$\begin{aligned}\hat{\Phi} =& \sqrt{\frac{L\hbar\omega}{2}}(\hat{a} + \hat{a}^\dagger),\\ \hat{Q} =& i\sqrt{\frac{C\hbar\omega}{2}}(\hat{a}^\dagger - \hat{a}).\end{aligned} \tag{1.2}$$

Here, $\hat{a}$ and $\hat{a}^\dagger$ are the annihilation and creation operators of the oscillator that obey the relation $[\hat{a}, \hat{a}^\dagger] = 1$. The zero-point fluctuations of the two conjugate operators, as given by Eq. (1.2), are expressed as $Q_{ZPF} = \sqrt{C\hbar\omega/2}$ and $\Phi_{ZPF} = \sqrt{L\hbar\omega/2}$. In the creation and annihilation operator notation, the Hamiltonian of the quantum LC oscillator can be written as

$$\hat{H} = \hbar\omega(\hat{a}^\dagger\hat{a} + 1/2), \tag{1.3}$$

where $\omega = \sqrt{1/LC}$ is the frequency of the oscillator. The eigenstate of the Hamiltonian (1.3) is $|n\rangle$, where $n = 0, 1, 2, ...$ $\hat{a}$ and $\hat{a}^\dagger$ satisfy

$$\begin{aligned}\hat{a}^\dagger|n\rangle =& \sqrt{n+1}|n+1\rangle,\\ \hat{a} =& \sqrt{n}|n-1\rangle,\\ \hat{a}^\dagger\hat{a}|n\rangle =& n|n\rangle.\end{aligned} \tag{1.4}$$

Using the above relations, the zero point fluctuations of the two conjugate operators can be define as $\langle 0|\hat{Q}^2|0\rangle = Q^2_{ZPF}$ and $\langle 0|\hat{\Phi}^2|0\rangle = \Phi^2_{ZPF}$.

The energy of the classical oscillator changes continuously when driven by thermal noise or external forces. In contrast, the energy of a quantum oscillator changes in discrete amounts. The smallest amount of energy that the oscillator can change is known as the quantum, $\hbar\omega$, which is determined by the frequency of the oscillator. This quantum of energy can be interpreted as the smallest unit of energy that a particle can possess or transfer. Thus, the quantum oscillator can be described in terms of quantized quasi-particles called photons. In an eigenstate $|n\rangle$, the number of photons, denoted by n, determines the energy of the oscillator. However, even in the absence of photons, the oscillator still possesses vacuum fluctuation energy of $\hbar\omega/2$. In other words, the quantum oscillator can never have zero energy, unlike the classical oscillator; there will always be some vacuum fluctuations. In the LC oscillator, this vacuum fluctuation is characterized by the voltage $\hat{V} = d\hat{\Phi}/dt = (1/i\hbar)[\hat{\Phi}, \hat{H}] = \hat{Q}/C$. In a typical few GHz oscillator, the vacuum fluctuation is characterized by $\Delta V_0 = \sqrt{\hbar\omega/2C} \approx 1\mu$V.

In practice, the oscillator interacts with an uncontrolled thermal environment, making it difficult to observe its behavior in the quantum regime. The thermal environment spreads the discrete energy levels and transitions them into continuous classical energy levels. To observe discrete quantum behavior, the oscillator must be sufficiently decoupled from the thermal environment so that the separation of the energy levels is considerably larger than, first, the broadening of the energy levels (dephasing) and, second, the thermal energy k_BT (relaxation). The first condition requires that the quality factor of the oscillator, defined as $Q = \frac{\omega}{\kappa}$, be large, where κ is the oscillator linewidth that describes the energy level broadening. Quality factors ranging from 10^3 to 10^8 can be achieved using superconducting circuits [1]. The second condition can be met by cooling the oscillator so that the thermal excitation energy is significantly reduced to $k_BT \ll \hbar\omega$. This condition is achievable in practice with microwave-frequency superconducting circuits operated below 20 mK in a dilution refrigerator [1].

1.3 Artificial Atom.

We have performed the quantization of a lumped LC oscillator circuit and discussed how it can be realized in practice using a superconducting microwave circuit cooled below 20 mK. Here, we will demonstrate how this oscillator can be transformed into an artificial atom by incorporating a non-linear element into the circuit. The energy levels of the LC oscillator are evenly spaced. To create unevenly spaced energy levels and use the oscillator as an artificial atom for quantum information processing, we introduce a non-linear inductor formed by a Josephson junction, as shown in Fig. 1.1. A Josephson junction consists of a thin insulating barrier at the interface between two superconductors. The current flowing through this junction is a dissipationless supercurrent,

$$I(t) = I_c sin\phi(t). \tag{1.5}$$

Here, ϕ is the phase difference between the superconducting condensates on either side of the junction, and I_c is the critical current, which depends on the energy gap required to break a Cooper pair. The Josephson inductance is related to the current flowing through the junction and the phase difference across it as: $L = (\partial I/\partial\Phi)^{-1}$ or using Eq. (1.5), $L = (\Phi_0/2\pi)(I_c cos\phi)^{-1}$. Since, the inductor has now become a non-linear, the Hamiltonian of the

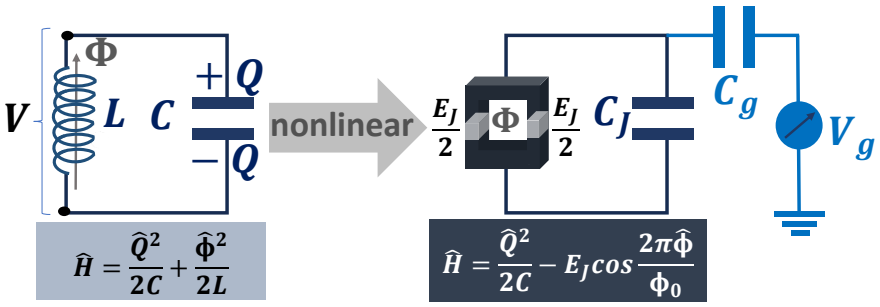

Figure 1.1: Linear simple harmonic oscillator (left side) is converted to a nonlinear oscillator (right side) by replacing the linear inductor with a nonlinear Josephson junction inductor. Square potential $\hat{\Phi}^2$ is changed to a cosin one ($cos(2\pi\hat{\Phi}/\Phi_0)$). To observe the quantum behaviour, the oscillator circuit is kept in a below 20 mK environment.

oscillator changes to:

$$\hat{H}_A = \frac{\hat{Q}^2}{2C_\Sigma} + \int \hat{V}(t)\hat{I}(t)dt, \tag{1.6}$$

where, $V(t) = (d\phi(t)/dt)(\Phi_0/2\pi)$ is the voltage across the junction. $\Phi_0 = h/2e$ is the flux quantum. Using Eq. (1.5), the Hamiltonian of the nonlinear Josephson junction oscillator become

$$\hat{H}_A = \frac{\hat{Q}^2}{2C_\Sigma} - \frac{I_c\Phi_0}{2\pi}cos\hat{\phi} \tag{1.7}$$

or

$$\hat{H}_A = \frac{\hat{Q}^2}{2C_\Sigma} - E_Jcos(2\pi\hat{\Phi}/\Phi_0), \tag{1.8}$$

where, $\hat{\Phi} = (\Phi_0/2\pi)\hat{\phi}$ and $E_J = \Phi_0 I_c/2\pi$ is the Josephson energy. $C_\Sigma = C_J + C_g$ is the sum of Josephson junction's capacitance C_J and gate capacitance C_g. Any external capacitor addition to the Josephson junction is included in C_J. We can include external voltage bias and thermal noise effect from the circuit by introducing an offset charge $2en_g = Q_g$ in the charge operator, i.e.,

$$\hat{H}_A = \frac{(\hat{Q} - Q_g)^2}{2C_\Sigma} - E_Jcos\hat{\phi}. \tag{1.9}$$

In term of number operator for the Cooper pairs transferred across the junction, $\hat{n} = \hat{Q}/2e$, we can write

$$\hat{H}_A = 4E_c(\hat{n} - n_g)^2 - E_J cos\hat{\phi}. \tag{1.10}$$

Here, $E_c = e^2/2C_\Sigma$ is the charging energy. Since the number operator $\hat{n}$ and the phase operator of the junction $\hat{\phi}$ are canonical conjugate, $|n\rangle$ in the phase basis can be written as

$$\begin{aligned} \hat{n} &= -i\frac{\partial}{\partial\phi} \\ |n\rangle &= \int_0^{2\pi} d\phi e^{-i\phi n}|\phi\rangle \end{aligned} \tag{1.11}$$

Substituting Eq. (1.11) in Eq. (1.10) and projecting the phase basis into the wave function $\Psi = \langle\phi|\Psi\rangle$ such that $H_T|\Psi\rangle = E|\Psi\rangle$ or $H_T\Psi = E\Psi$, where E is the eigenenergy, we get the time independent Schrodinger equation

$$[4E_c(-i\frac{\partial}{\partial\Phi} - n_g)^2 - E_J cos\phi]\Psi = E\Psi. \tag{1.12}$$

The analytical solution of this equation can be solved in terms of Mathieu functions [2, 52–54]. Alternatively, Eq. (1.10) can also be solved numerically in the number basis.

$$\hat{H}_A = \sum_n 4E_c(\hat{n} - n_g)^2|n\rangle\langle n| - \frac{E_J}{2}\sum_n(|n\rangle\langle n+1| + |n+1\rangle\langle n|). \tag{1.13}$$

The eigenenergies spectrum of Eq. (1.12) and (1.13) as a function of offset charge n_g for different E_J/E_c ratios are shown in Fig. 1.2. We observe two distinct energy spectrum corresponding to two ratios $E_J < E_c$ and $E_J >> E_c$. The energy spectrum for $E_c > E_J$ is highly anharmonic. As a result this spectrum is suitable for implementing a two-level system or a qubit. From the figure we see that by confining $n_g \in [0, 1]$, the only relevant number operator basis of the Cooper pair we can consider are $|n = 0\rangle$ and $|n = 1\rangle$. Truncating the Hamiltonian (1.13) in this two dimensional Hilbert space yields

$$\hat{H}_q = -\frac{E_{cl}}{2}\sigma_z' - \frac{E_J}{2}\sigma_x', \tag{1.14}$$

where, $E_{cl} = 4E_c(1 - 2n_g)$. By transforming into the qubit basis, Hamiltonian (1.14) can be written as

$$\hat{H}_q = \frac{\hbar\Omega}{2}\sigma_z, \tag{1.15}$$

where, $\hbar\Omega = (E_J^2 + (4E_c(1-2n_g))^2)^{1/2}$. Here, the transformation is $\sigma_z' = -\sigma_z cos\theta + \sigma_x sin\theta$ and $\sigma_x' = -\sigma_x cos\theta - \sigma_z sin\theta$, where $\tan\theta = E_J/E_{cl}$. This qubit is referred to as a *charge qubit* because the charging energy is significant. Due to the large E_c, the transition frequency Ω is highly susceptible to offset charge fluctuations induced by the circuit environment, which leads to the dephasing of the qubit. One can reduce the sensitivity to charge fluctuations

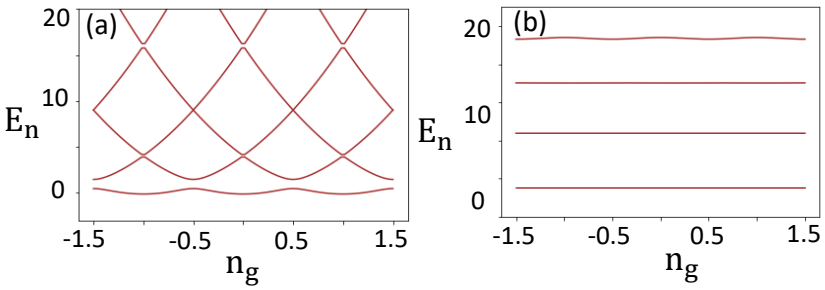

Figure 1.2: The energy levels of superconducting qubits as a function of offset charge are illustrated, with (a) showing the charge qubit energy levels at the ratio $E_C = 2E_J$. and (b) depicting the transmon qubit energy levels at the ratio $E_J = 40E_C$.

by increasing the Josephson energy or decreasing the charging energy, i.e., $E_J >> E_C$. The energy spectrum under this variation is shown in the Fig 1.2. As evident from the figure, the energy levels become independent of the offset charge and, consequently, the fluctuations. This reduction in sensitivity to charge noise comes with a trade-off: the anharmonicity of the transition frequencies is reduced. However, the charge dispersion from the fluctuations vanishes exponentially with $(E_J/E_c)^{1/2}$, whereas the anharmonicity decreases with the ratio $(E_J/E_c)^{1/2}$ [2]. We can significantly suppress charge noise before losing all anharmonicity. Therefore, the energy spectrum in this approximation can be safely realized as a qubit. Such qubits are known as *transmon qubit*. Since the anharhonicity is small in the transmon qubit regime, we can retain only upto the first nonlinear contribution from the potential energy term $-E_J cos\hat{\phi}$ in the Hamiltonian (1.10). Hamiltonian of the transmon qubit reads

$$\hat{H}_T = 4E_c\hat{n}^2 - E_J + \frac{1}{2}E_J\hat{\phi}^2 - \frac{1}{4!}E_J\hat{\phi}^4 \tag{1.16}$$

We have excluded the offset charge since the dispersion is significantly suppressed. However, we can reintroduce it when the qubit is coupled to an external oscillation source, such as a cavity.. It is convinient to write the Hamiltonian in the annihilation $\hat{b}$ and creation $\hat{b}$ operators, where

$$\begin{aligned}\hat{\phi} =&(\frac{2E_c}{E_J})^{1/4}(\hat{b}+\hat{b}^\dagger),\\ \hat{n} =&\frac{i}{2}(\frac{E_J}{2E_c})^{1/4}(\hat{b}^\dagger-\hat{b}).\end{aligned} \tag{1.17}$$

The reduced in the anharmonicity or the phase $\hat{\phi}$ can be inferred from this relation. Substituting in Eqn. 1.17, we get

$$\begin{aligned}\hat{H}_T =&\sqrt{8E_cE_J}(\hat{b}^\dagger\hat{b}+\frac{1}{2})-E_J-\frac{E_c}{12}(\hat{b}+\hat{b}^\dagger)^4\\ \hat{H}_T \approx&\hbar\Omega_T(\hat{b}^\dagger\hat{b}+\frac{1}{2})-E_J-\frac{E_c}{12}(6(\hat{b}^\dagger\hat{b})^2+6\,\hat{b}^\dagger\hat{b}+3)\end{aligned} \tag{1.18}$$

where, $\hbar\Omega_T = \sqrt{8E_cE_J}$ is the Josephson plasma frequency. In the second line of Eqn. 1.18, the rotating wave approximation (RWA) is applied which is valid here since $\hbar\Omega_t >> E_c/4$. The operators $\hat{b}^\dagger$ and $\hat{b}$ constitute simple harmonic approximation to the transmon qubit. In terms of this basis the eigenenergies of the transmon yields

$$E_n = \hbar\Omega_T(n+\frac{1}{2})-E_J-\frac{E_c}{12}(6n^2+6\,n+3) \tag{1.19}$$

Using this relation we can calculate the anharmonicity of the transmon $\alpha = (E_2-E_1)-(E_1-E_0)$ and relative anharmonicity $\alpha_r = \alpha/(E_1-E_0)$. We get $\alpha = -E_c$ and $\alpha_r = -8(E_J/E_c)^{-1/2}$. In circuit Quantum Electrodynamics (QED) experiments, transmon qubits are designed with transition frequencies typically in the gigahertz (GHz) range. The anharmonicity of a transmon, given by (E_c/h) is in the range of a few hundred megahertz (MHz). Although the anharmonicity is much smaller than the transition frequency, it is sufficiently large compared to the linewidth of the energy levels, making it possible to resolve the anharmonicity experimentally. This ability to resolve anharmonicity is crucial in circuit QED experiments, as it allows for precise control over the qubit's energy levels and interactions.

Another important feature frequently implemented in quantum circuit architecture is the ability to tune the frequency of the qubit. This can be

achieved by replacing the single Josephson junction with two parallel junctions, forming a superconducting quantum interference device (SQUID) or a split Cooper pair box (CPB), as shown in Fig. 1.1. The nonlinear element in Eq. (1.8) then become $-E_1 cos\hat{\phi}_1 - E_2 cos\hat{\phi}_2$. If we thread an external flux ϕ_e through the SQUID loop such that $\hat{\phi}_1 - \hat{\phi}_2 = (2\pi/\Phi_0)\Phi_e$, the nonlinear term can be written as $-E_J(\Phi_e)cos(\hat{\phi} - \phi_0)$, where

$$E_J(\Phi_e) = (E_1 + E_2)cos(\frac{\pi\Phi_e}{\Phi_0})\sqrt{1 + \phi_0^2}. \tag{1.20}$$

Here, $d = (E_2 - E_1)/(E_1 + E_2)$ is the junction asymmetry, $\phi_0 = d\,tan(\frac{\pi\Phi_e}{\Phi_0})$ and $\phi = (\phi_1 + \phi_2)/2$. Both the charge qubit and transmon frequencies depend on the Junction energy $E_J(\Phi_e)$. Therefore, by threading an external flux Φ_e, we can tune their frequencies, leading to what are known as flux-tunable qubits [2, 55–58]. So far, we have discussed two types of qubits based on different ratios of E_J/E_c: the charge qubit and the transmon qubit. There are other qubits realized based on the number of junctions implemented and the topology of the circuit. These include phase qubit [59], flux qubit [60–62], fluxonium [63], 0-π qubit [64, 65], among others.

We have seen how an artificial atom can be implemented by adding a nonlinear element to a simple quantum LC harmonic oscillator. By varying different circuit elements, we have realized various types of qubits. Next, we will place the artificial atom inside a microwave cavity resonator and study the interaction between them, which is essential for measuring and controlling the qubit.

1.4 Cavity-Qubit Interaction.

The qubit is placed in a microwave resonator and coupled capacitively to the resonator mode as shown in Fig. 1.3. The microwave resonator can be either a 2D planar waveguide or a 3D cavity where the electromagnetic wave is confined. In a 2D planar waveguide, a conducting plate of finite length is positioned at the center between two ground plates, all of which are deposited on the surface of a low-loss dielectric substrate [1, 66–74]. The electromagnetic wave is confined between the central plate and the ground plates. In a 3D resonator, the electromagnetic field is confined within a vacuum formed by a metallic cavity and a conductor. Superconductors such as aluminum and niobium are typically used as the conducting plates [75–80].

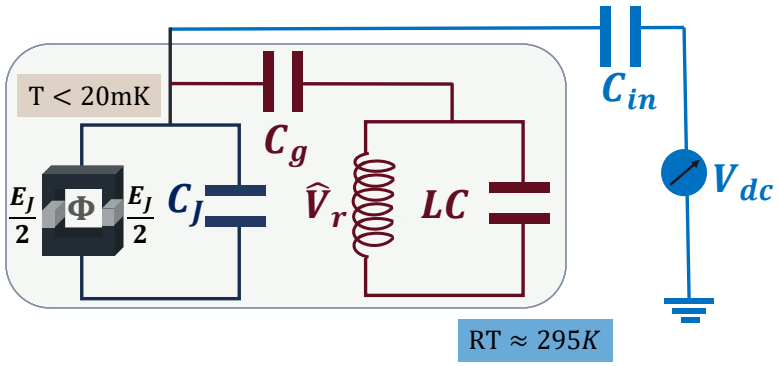

Figure 1.3: Schematic of qubit-cavity coupling. A microwave cavity represented by the LC oscillator is coupled to the qubit through the capacitor C_g. Additionally, a DC bias is connected to the qubit through a input capacitor C_{in}. The qubit-cavity system is kept in a cold environment (below 20mK) to maintain quantum behaviour and the external DC bias is kept at room temperature RT.

In both types of resonators, the qubit is situated at the center, where the antinode of the confined electromagnetic wave is located. While the resonators support multiple modes, we focus only on the mode (ω_r) that is close to the qubit frequency, neglecting all other modes by assuming their frequencies are far from that of the qubit. The resonator is first prepared in the quantum regime by carefully implementing the conditions discussed in Section 1.2. The presence of this quantized resonator is felt by the qubit through the offset charge, as any external bias to the qubit is transmitted through it. If we also consider a DC bias connected through an input capacitor C_{in} along with the quantum resonator, as shown in the Fig. 1.3, then the bias voltage of the qubit will change to

$$\hat{V}_g = \hat{V}_r + V_{dc}, \tag{1.21}$$

where $\hat{V}_r = V_{ZPF}(\hat{a}^\dagger + \hat{a})$ and $V_{ZPF} = (\hbar\omega_r/LC)^{1/2}$. Subsequently, $\hat{n}_g = \hat{n}_r + n_g$, where $\hat{n}_r = C_g\hat{V}_r/2e$ and $n_g = (C_{in})V_{dc}/2e$. Substituting this change in Eq. (1.13) and then truncating into the qubit subspace yields the charge qubit-resonator Hamiltonian

$$\hat{H}_q = -\frac{E_{cl}}{2}\hat{\sigma}'_z - \frac{E_J}{2}\hat{\sigma}'_x + \hbar\omega_r\hat{a}^\dagger\hat{a} - e\frac{C_g}{C_\Sigma}V_{ZPF}(\hat{a}^\dagger + \hat{a})(1 - 2n_g - \hat{\sigma}'_z). \tag{1.22}$$

The rapidly rotating terms and the frequency shift of the resonator are neglected. Hamiltonian of the resonator $\hbar\omega_r\hat{a}^\dagger\hat{a}$ is included. Transforming

Eq. (1.22) in the qubit basis, similar to Eq. (1.15), leads to

$$\hat{H}_q = \frac{\hbar\Omega}{2}\hat{\sigma}_z + \hbar\omega_r \hat{a}^\dagger \hat{a} + \hbar g(\hat{a}^\dagger + \hat{a})\hat{\sigma}_x, \tag{1.23}$$

where $\Omega = E_J/\hbar$ and $\hbar g = e(C_g/C_\Sigma)V_{ZPF}$. We have taken the charging energy at the charge degeneracy or the sweet point $n_g = 1/2$. It is useful to write the coupling strength g in terms of dipole moment (d) of the artificial atom and the zero-point electric field (E_{ZPF}),of the resonator, i.e., $\hbar g = d\, E_{ZPF}$, where $d = el$ and $E_{ZPF} = (C_g/C_\Sigma)V_{ZPF}/l$. l is the tunneling distance of a Cooper pair across the junction. Since the scale of the parameters are in μm, both the dipole moment and the zero-point field can be made large [3]. In a typical circuit QED experiment, dipole moment can reach upto the order of $10^4 e a_0$ and $E_{ZPF} \approx 0.1V/m$ in a 2D resonator. The corresponding vacuum Rabi oscillation rate $g\pi$ can reach $\approx$ 100MHz.

Assuming $\Omega >> g$, the fast rotating terms in the Hamiltonian 1.23 can be dropped and we get the Jaynes-Cummings (JC) interaction,

$$\hat{H}_{jc} = \frac{\hbar\Omega}{2}\hat{\sigma}_z + \hbar\omega_r \hat{a}^\dagger \hat{a} + \hbar g(\hat{a}^\dagger \hat{\sigma}_- + \hat{\sigma}_+ \hat{a}). \tag{1.24}$$

This Hamiltonian is exactly solvable. The interaction term only couples the nearest photon excitations and hence the only relevant states/basis are $|n-1, e\rangle$ and $|n, g\rangle$. Therefore, the JC Hamiltonian in this basis can be written as

$$H_{jc} = \begin{bmatrix} \hbar\omega_r n & \hbar g\sqrt{n} \\ \hbar g\sqrt{n} & \hbar\omega_r n + \hbar\Delta \end{bmatrix} \tag{1.25}$$

where, $\Delta = \Omega - \omega_r$. The corresponding eigenenergies are

$$E_\pm = \hbar\omega_r n + \frac{\hbar\Delta}{2} \pm \hbar\sqrt{g^2 n + (\Delta/2)^2}. \tag{1.26}$$

The interacting term does not couple the ground state $|0, g\rangle$ with any other states. The eigenstates are given by

$$\begin{aligned} |\psi\rangle_- &= cos(\theta_n/2)|g, n\rangle - sin(\theta_n/2)|e, n-1\rangle, \\ |\psi\rangle_+ &= sin(\theta_n/2)|g, n\rangle + cos(\theta_n/2)|e, n-1\rangle, \end{aligned} \tag{1.27}$$

where $tan\theta_n = \Delta/(2g\sqrt{n})$. From Eq. (1.26) and (1.27) we see that the qubit and the resonator states become dressed and generate entangled states

$|\psi\rangle_-$ and $|\psi\rangle_+$. The states are maximally entangle at zero detuning $\Delta = 0$. As we increase the detuning, the entanglement vanishes and for $\Delta >> g$, $cos(\theta_n/2) \to 1$ and $sin(\theta_n/2) \to 0$, the dressed state become separable. In this case, the initial states of the qubit and the resonator remains unchanged while their transition frequencies are altered by a factor that is dependent on the qubit state and the number of excited resonator photons. This large detuning interaction is called dispersive interaction. The Hamiltonian in the dispersive regime can be obtained by diagonalizing the JC Hamiltonian in the bare qubit-resonator basis using the unitary transformation $\hat{U} = exp[\delta(\hat{N})(\hat{a}^\dagger\hat{\sigma}_- - \hat{a}\hat{\sigma}_+]$, where $\delta(\hat{N}) = tan^{-1}(2\lambda\sqrt{\hat{N}})/(2\sqrt{\hat{N}})$ and $\lambda = g/\Delta$. The transformed Hamiltonian reads [81, 82]

$$\hat{H}_{jd} = \frac{\hbar\Omega}{2}\hat{\sigma}_z + \hbar\omega_r\hat{a}^\dagger\hat{a} - \frac{\hbar\Delta}{2}\left(1 - \sqrt{1 + 4\lambda^2\hat{N}}\right)\hat{\sigma}_z. \tag{1.28}$$

Taking the limit of $\Delta >> g$ yields the dispersive Hamiltonian,

$$\hat{H}_{jd} = (\frac{\hbar\Omega}{2} + \frac{g^2}{\Delta})\hat{\sigma}_z + \hbar(\omega_r + \frac{g^2}{\Delta}\hat{\sigma}_z)\hat{a}^\dagger\hat{a}. \tag{1.29}$$

The interaction term commutes with the non-interacting terms indicating that the qubit-resonator interaction only shifts the transition frequencies without disturbing the initial state of the system. Such dispersive coupling is employed in quantum non-demolition measurement. Note that Eq. (1.29) is valid for mean photon number less than $1/(4\lambda^2)$. Higher order correction from the Taylor expansion of Eq. (1.28) are required for larger mean photon numbers.

The transmon qubit also couples with the microwave resonators in a similar manner to the charge qubit discussed above. This coupling comes from the charging term, as the transmon is capacitively coupled. Although we have removed the offset DC bias n_g, which is irrelevant in the transmon regime, the transmon sees the quantum resonator through the offset charge. Similar to the charge qubit case, we introduce the resonator charge operator $\hat{n}_r = C_g\hat{V}_r/2e$ in the charging energy term. By substituting $\hat{n} \to \hat{n} + \hat{n}_r$ in the charging term of Eq. (1.16), we get the Hamiltonian of the transmon-resonator coupled system,

$$\begin{aligned}\hat{H}_{tc} &= \hbar\Omega_T(\hat{b}^\dagger\hat{b} + \frac{1}{2}) - E_J - \frac{E_c}{12}(6(\hat{b}^\dagger\hat{b})^2 + 6\,\hat{b}^\dagger\hat{b} + 3) \\ &\quad -\hbar g_t(\hat{a}^\dagger - \hat{a})(\hat{b}^\dagger - \hat{b}),\end{aligned} \tag{1.30}$$

where

$$g_t = e\frac{C_g}{C_\Sigma}\left(\frac{E_J}{2E_c}\right)^{1/4} V_{ZPF}. \tag{1.31}$$

Here, we have taken $\hat{n}_r = i(C_g V_{ZPF}/2e)(\hat{a}^\dagger - \hat{a})$. The coupling constant g_t can be interpreted similarly to that in the charge qubit case. In the transmon scenario, it is important to note that the dipole moment depends on the E_J/E_c ratio. We derive the JC interaction (Eq. (1.24)) by applying the rotating wave approximation and then truncating to the qubit basis. In the dispersive regime for the transmon qubit, virtual transitions to higher energy levels occur due to the reduced anharmonicity. Therefore, we diagonalize the Hamiltonian (1.30) using the Schrieffer-Wolff (SW) transformation to second order. We then truncate the Hilbert space to the qubit subspace, resulting in the dispersive Hamiltonian of the transmon.

$$\hat{H}_{td} = \hbar\left(\frac{\Omega_T}{2} + \frac{g^2}{\Delta}\right)\sigma_z + \hbar\left(\omega_r + \frac{g^2}{\Delta - E_c/\hbar}\frac{g^2}{\Delta}\right)\hat{a}^\dagger\hat{a} + \hbar\lambda_T\hat{\sigma_z}\hat{a}^\dagger\hat{a} \tag{1.32}$$

where,

$$\lambda_T = -\frac{g^2 E_c/\hbar}{\Delta(\Delta - E_c/\hbar)}). \tag{1.33}$$

Unlike the charge qubit, the transmon dispersive pull is highly dependent on the charging energy E_c [2].

1.5 Coupling to the Environment.

The discussion so far has not taken into account the unavoidable coupling of the qubit-cavity system with circuit environmental noise or uncontrollable degrees of freedom. The qubit experiences these circuit noises through the offset charge, which includes a quantum fluctuation component induced by the environmental noise. This noise can be modeled as a bath consisting of an infinite number of simple harmonic oscillators, each with different modes coupled to the qubit-cavity system. The offset charge can then be expressed as: $\hat{n} \to \hat{n} + \hat{n}_e$, where $\hat{n}_e = j\sum_i n_i(\hat{c}_i^\dagger - \hat{c}_i)$ represents the contribution from the bath. Substituting in Eq. (1.16), we get the bath-system interaction terms and the Hamiltonian (1.32), i.e., $\hat{H}_B = \hat{H}_{tc} + \hat{H}_{bs}$, where

$$\hat{H}_{bs} = \sum_i \hbar\omega_i\hat{c}_i^\dagger\hat{c}_i + \hbar\sum_i G_i'(\hat{b}^\dagger\hat{c}_i - \hat{c}_i^\dagger\hat{b}) + \sum_i \hbar G_i(\hat{a}^\dagger\hat{d}_i - \hat{d}_i^\dagger\hat{a}). \tag{1.34}$$

The last two terms represent the system-bath couplings, and we have assumed the rotating wave approximation. The interaction of the cavity with the bath is also included in the last term. For simplicity, we assume that the qubit and cavity baths are uncorrelated. The cavity bath couplings arise from the resonator's capacitive coupling to the input and output ports for driving and measuring the qubit, as well as from internal losses associated with the material used to fabricate the resonator [83]. By solving for the density matrix of the qubit-cavity system and tracing out the bath degrees of freedom under the Born-Markov approximation, we arrive at the well-known Lindblad master equation [84–86].

$$\begin{aligned}\dot{\hat{\rho}}_{tc} &= -\frac{i}{\hbar}[\hat{H}_{tc}, \hat{\rho}_{tc}] + \kappa(n_{th}+1)\mathcal{L}[\hat{a}] + \kappa n_{th}\mathcal{L}[\hat{a}^\dagger] \\ &\quad +\Gamma(n_{thq}+1)\mathcal{L}[\hat{b}] + \Gamma n_{thq}\mathcal{L}[\hat{b}^\dagger], \end{aligned} \tag{1.35}$$

where $\mathcal{L}[\hat{o}] = (2\hat{o}\hat{\rho}_{tc}\hat{o}^\dagger - \hat{o}^\dagger\hat{o}\hat{\rho}_{tc} - \hat{\rho}_{tc}\hat{o}^\dagger\hat{o})/2$ with $\hat{o} \in \{\hat{a}, \hat{a}^\dagger, \hat{b}, \hat{b}^\dagger\}$. κ and Γ are the decay rates of the resonator and the qubit, respectively. n_{th} and n_{thq} are the thermal occupation of the bosonic bath at the resonator and qubit frequency, respectively. Notice that the qubit-resonator system couples to the bath capacitively, as the interaction term in Eq. (1.34) arises from the capacitively charging term E_c. In addition to the excitation and relaxation processes induced by the bath, the qubit can also experience energy level dephasing. This dephasing is caused by fluctuations in the parameters that control the transition frequency, as well as by dispersive coupling to other degrees of freedom [87, 88]. For example, the dispersive coupling between the qubit and the resonator can lead to dephasing of the qubit due to fluctuations in the resonator photon number or shot noise [89–91]. The dephasing of the qubit can be phenomenologically introduced by adding the interaction $\sum_i \hat{c}_i^\dagger \hat{c}_i \hat{b}^\dagger \hat{b}$ [86]. Following the same procedure as before, the resulting dephasing term yields $(\Gamma_\phi/2)\mathcal{L}\left[\hat{b}^\dagger\hat{b}\right]$, where Γ_ϕ is the dephasing rate. The master equation (Eq. (1.43)) in the two-level subspace can be generated by trucating $\hat{b} \to \hat{\sigma}_-$ and $\hat{b} \to \hat{\sigma}_+$.

In the dispersive regime, the qubit-cavity system is diagonalized using a perturbative second-order Schrieffer-Wolff transformation. In the presence of dissipation, this transformation must also be applied to the system-bath interaction. As a result, a modified decay rates for the system is obtained: $\kappa \to \kappa + \lambda^2\gamma(\omega_r)$ and $\gamma \to \gamma + \lambda^2\kappa(\Omega_T)$, where $\gamma(\omega_r)$ and $\kappa(\Omega_T)$ are the resonator decay rate at qubit frequency and qubit decay rate at resonator

frequency, respectively. $\lambda^2\kappa(\Omega_T)$ is known as Purcell decay rate [92]. It is the rate at which the qubit decays to the ground state induced by the resonator. Additionally, two induced dephasing terms also pops up from the transformation: $\Gamma_\delta\mathcal{L}[\hat{a}^\dagger\hat{b}]$ and $\Gamma_\delta\mathcal{L}[\hat{b}^\dagger\hat{a}]$, where $\Gamma_\delta = 2\lambda^2\Gamma_\phi$. These dephasing terms arise due to the detuning Δ [2, 3].

An alternative approach for addressing the bath involves solving the Heisenberg equation of the system-bath Hamiltonian $\hat{H}_B$. By applying the Markovian approximation and assuming weak coupling between the system and the bath, the Heisenberg equation of motion for an operator can be expressed as the Langevin equation [93, 94].

$$\dot{\hat{o}}(t) = \frac{1}{i\hbar}[\hat{o}, \hat{H}_{tc}] - \frac{d}{2}\hat{o}(t) + \sqrt{k}\hat{o}_{in}(t). \tag{1.36}$$

Here, $\hat{o}$ is the operators of the system and $d \in \{\gamma, \Gamma\}$. $\hat{o}_{in}(t)$ is the sum of the intrinsic noise operator of the system and the input noise affecting the system. The thermal contribution represented by n_{th} arises from the intrinsic noise. If there is an external drive applied to the system, the drive contribution will come from the input noise part of the operator $\hat{o}_{in}(t)$. For example, if we drive the cavity resonator through an input port, then the input noise term can be separated as the input drive part and the intrinsic part. The input drive itself can further be divided into classical and quantum components. As a result, the Langevin equation can be separated into classical and quantum dynamics. More details on this concept will be discussed in the following sections.

1.6 Qubit-Mechanical interaction

As discussed in the introduction, a superconducting qubit can interact with a mechanical resonator in various ways, depending on the type of resonators used. For instance, a suspended superconducting micromechanical or nanomechanical resonator, typically made of aluminum and operating at a few MHz, can couple with the qubit either longitudinally or transversely, depending on the integration method of the resonator with the qubit. On the other hand, when the resonator mode is realized in a phononic crystal and interacts with the qubit via piezoelectric response, the coupling is exclusively transverse. Different schemes for achieving qubit-mechanical coupling in hybrid electromechanical systems, based on the types of resonators, are illustrated in Fig. 1.4.

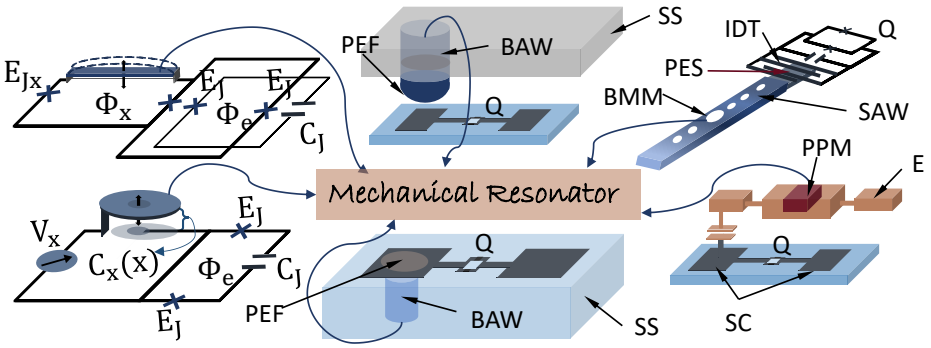

Figure 1.4: Schematic of hybrid electromechanical system: A suspended mechanical resonator is coupled to the qubit either by inducing a flux Φ_x from the mechanical displacement (top left) or by changing the capacitance $C_x(x)$ due to mechanical motion (bottom left). In the middle, two bulk acoustic wave (BAW) phononic crystals are coupled to the qubit (Q), either using a flip-chip architecture (top) or on a single-chip sapphire substrate (denoted by SS) (bottom). In both arrangements, the electric field from the qubit excites the piezoelectric film (PEF), typically AlN, which in turn excites the BAW in the substrate. On the top right, a patterned mechanical crystal is coupled to a qubit through a piezoelectric slab (PES). The excitation from the qubit is first transferred to the PES via an interdigitated transducer (IDT) and then to a breathing mechanical mode (BMM) in the crystal through surface acoustic waves (SAW). Another realization of the flip-chip architecture, where the supeconducting (SC) squbit is coupled to a piezoelectric phononic mode (PPM) deposited on the defects of the electrode (E), is shown on the bottom right [11, 13, 14].

1.6.1 Transverse Coupling

The transverse coupling between a qubit and a mechanical resonator can be realized in two main ways, depending on how the resonators are integrated into the superconducting chip that includes the qubit. In one approach, a mechanical resonator is fabricated by suspending it on the circuit chip, allowing it to couple to the qubit by making the capacitance of the capacitor that connects them dependent on the resonator's displacement. Since the mechanical resonator is suspended, it oscillates out of the circuit plane. The other type of coupling involves phononic crystals, where the qubit-mechanical coupling is achieved through the piezoelectric response of the resonator. In

both cases, the Hamiltonian can be expressed as follows [25, 95]:

$$\hat{H}_{tm} = \hat{H}_T + \hbar\omega_m \hat{m}^\dagger \hat{m} - \hbar G_{tm}(\hat{b}^\dagger - \hat{b})(\hat{m}^\dagger - \hat{m}), \tag{1.37}$$

where $\hat{H}_T$ is the transmon Hamiltonian and $\hat{m}$ is the mechanical operator. Notice that this interaction is similar to that obtained for the qubit-cavity system. Therefore, all the discussions relevant to the qubit-cavity case are also applicable here. By applying the rotating wave approximation and restricting to the qubit basis, we obtain the Jaynes-Cummings interaction:

$$\hat{H}_{tm} = \hbar\frac{\Omega_T}{2}\hat{\sigma}_z + \hbar\omega_m \hat{m}^\dagger \hat{m} + \hbar G_{tm}(\hat{m}^\dagger \hat{\sigma}_- + \hat{\sigma}_+ \hat{m}). \tag{1.38}$$

The eigenenergies are given by

$$E_\pm = \hbar\omega_m m + \frac{\hbar\Delta_m}{2} \pm \hbar\sqrt{G_{tm}^2 m + (\Delta_m/2)^2} \tag{1.39}$$

and the corresponding eigenstates by

$$\begin{aligned} |\Psi\rangle_- &= cos(\theta_m/2)|g, m\rangle - sin(\theta_m/2)|e, m-1\rangle, \\ |\Psi\rangle_+ &= sin(\theta_m/2)|g, m\rangle + cos(\theta_m/2)|e, m-1\rangle, \end{aligned} \tag{1.40}$$

where $tan\theta_n = \Delta_m/(2g\sqrt{m})$ and $\Delta_m = \Omega_T - \omega_m$. These are the entangled dressed states of the qubit-mechanical system. The dressed state become maximally entangled at zero detuning $\Delta_m = 0$. The energy splitting between any two dressed states is given by $\hbar 2G_{tm}\sqrt{m}$, where $m = 1, 2, 3...$ is the phonon number of the mechanical resonator. For weak excitation of the mechanical resonator, although the dressed states are entangled, the energy splitting is simply a feature of avoided crossing resulting from the mode splitting between two coupled classical or quantum systems. To demonstrate quantum behavior, the coupled system must be driven to higher excitations, revealing a signature of $\sqrt{m}$ dependence in the energy splitting [96].

The avoided crossing between the qubit-mechanical dressed states can be observed from the qubit spectrum generated by probing the qubit spectroscopy [21, 26, 27]. To perform the spectroscopy we continuously drive the qubit at the spectroscopy frequency ω_s and with amplitude Ω_R using the gate voltage. Adding the spectroscopic drive in the qubit-mechanical Hamiltonian reads

$$\hat{H}_{sp} = \hat{H}_{tm} + \hbar\frac{\Omega_R}{2}cos(\omega_s t)\sigma_x. \tag{1.41}$$

In the drive frame, we have

$$\hat{H}_{sp} = \hbar\frac{\delta_T}{2}\hat{\sigma}_z + \hbar\delta_m\hat{m}^\dagger\hat{m} + \hbar G_{tm}(\hat{m}^\dagger\hat{\sigma}_- + \hat{\sigma}_+\hat{m}). + \hbar\frac{\Omega_R}{2}\sigma_x. \tag{1.42}$$

Here, $\delta_T = \Omega_T - \omega_s$ and $\delta_m = \omega_m - \omega_s$. The spectrum of the qubit can be generated from the steady state value of $P_e = (1/2)(\langle\sigma_z\rangle_{ss} + I)$. In the presence of the noisy environment, P_e can be calculated either from the master equation,

$$\begin{aligned}\dot{\hat{\rho}}_{sp} &= -\frac{i}{\hbar}[\hat{H}_{sp}, \hat{\rho}_{sp}] + \kappa(n_{th}+1)\mathcal{L}[\hat{a}] + \gamma n_{th}\mathcal{L}[\hat{a}^\dagger] \\ &\quad +\Gamma(n_{thq}+1)\mathcal{L}\left[\hat{c}\right] + \Gamma n_{thq}\mathcal{L}\left[\hat{c}^\dagger\right],\end{aligned} \tag{1.43}$$

or from the set of Langevin equations,

$$\langle\dot{\hat{m}}\rangle = -\left(\frac{\gamma}{2} + i\delta_m\right)\langle\hat{m}\rangle - iG_{tm}\langle\hat{\sigma}_-\rangle \tag{1.44a}$$

$$\langle\dot{\hat{\sigma}}_-\rangle = -\left(\frac{\Gamma}{2} + i\delta_T\right)\langle\hat{\sigma}_-\rangle + iG_{tm}\langle\hat{\sigma}_z\hat{m}\rangle + \frac{i\Omega_R}{2}\langle\hat{\sigma}_z\rangle \tag{1.44b}$$

$$\begin{aligned}\langle\dot{\hat{\sigma}}_z\rangle &= -\frac{\Gamma}{2}\langle\hat{\sigma}_z\rangle - 2i\,G_{tm}\langle\hat{\sigma}_+\hat{m}\rangle + 2i\,G_{tm}\langle\hat{\sigma}_-\hat{m}^\dagger\rangle \\ &\quad +i\Omega_R(\langle\hat{\sigma}_-\rangle - \langle\hat{\sigma}_+\rangle)\end{aligned} \tag{1.44c}$$

obtained by substituting $\hat{H}_{sp}$ in the place $\hat{H}_{tc}$ in Eq. (1.36) and taking the average value. For obtaining the avoided-crossing spectrum, we take the semi-classical assumption, i.e., $\langle\hat{m}\hat{\sigma}_z\rangle = \langle\hat{m}\rangle\langle\hat{\sigma}_z\rangle$, $\langle\hat{m}\hat{\sigma}_+\rangle = \langle\hat{m}\rangle\langle\hat{\sigma}_+\rangle$ and $\langle\hat{m}^\dagger\hat{\sigma}_-\rangle = \langle\hat{m}^\dagger\rangle\langle\hat{\sigma}_-\rangle$, and solve for $\langle\hat{\sigma}_z\rangle$ at the steady state. The spectrum is shown in Fig. 1.5. The separation between the two peaks at the $\Omega_T = \omega_m$, where the avoided crossing occur is twice the coupling constant G_{tm}. Thus, by probing the spectrum, we can determine the coupling strength of the qubit-mechanical hybrid system. The vacuum Rabi oscillation of the excitation state probability, P_e, is also shown in the figure. To probe the qubit spectrum, we utilize qubit spectroscopy, where the qubit is dispersively coupled to a cavity resonator, as discussed in the previous section. We drive the cavity and measure the transmitted or the reflected signal. In the weak dispersive coupling limit, the phase of the transmitted signal is directly related to the qubit population, allowing us to obtain the qubit spectrum by measuring the phase [89, 90]. This probing process, which involves a two-tone signal drive consisting of a spectroscopic tone and a probe tone, is referred to as *two-tone*

spectroscopy. It is important to note that the avoided crossing is observed only for the hybrid system when the resonator frequency and qubit frequency are within the same range.

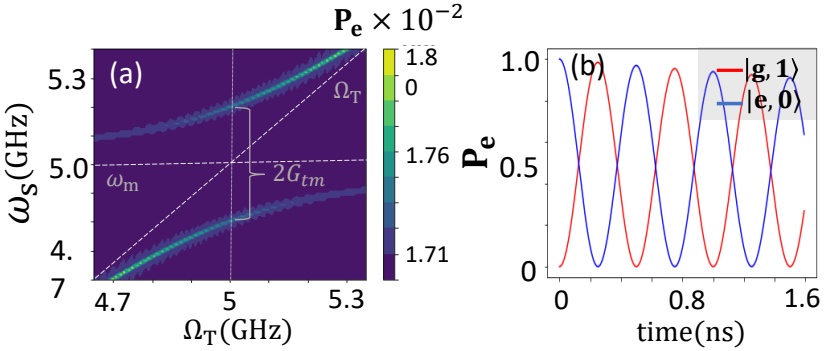

Figure 1.5: (a) Spectrum Of excited state probability P_e. The horizontal dotted line shows the qubit frequency and the diagonal line represents the change in the qubit frequency. (b) Rabi oscillation of the qubit excited state. Parameters: $\gamma/2\pi = \Gamma/2\pi = 0.1$MHz, $\Omega_R/2\pi = 0.1$MHz, $G_{tm}/2\pi = 0.2$MHz and $\omega_m/2\pi = 5$GHz

In the dispersive regime, where the detuning between the qubit and mechanical frequencies is much larger than the resonant coupling strength, the phonon number distribution of the mechanical resonator can be measured by probing the qubit excited state probability spectrum P_e. This is achieved by dispersively coupling the qubit with the mechanical resonator and populating the resonator by driving it in resonance with a microwave pulse at frequency ω_d and amplitude ϵ. By performing qubit spectroscopy, we can determine the phonon occupancy distribution of the mechanical resonator from the qubit excitation spectrum [27, 30]. The Hamiltonian for this setup in the drive frame, applying the rotating wave approximation, is given by:

$$\hat{H}_d = \frac{\hbar}{2}(\Delta_T + 2\chi\hat{m}^\dagger\hat{m})\sigma_z + \hbar\Delta_m\hat{m}^\dagger\hat{m} + \hbar\epsilon(\hat{m}^\dagger + \hat{m}) + \hbar\frac{\Omega_R}{2}\sigma_x, \qquad (1.45)$$

where,

$$\chi = -\frac{G_{tm}^2 E_c/\hbar}{\delta(\delta - E_c/\hbar)}, \qquad \Delta_m = \omega_m - \omega_d + \frac{G_{tm}^2}{\delta - E_c/\hbar}. \qquad (1.46)$$

$\Delta_T = \Omega_T + G_{tm}^2/\delta - \omega_s$ and $\delta = \Omega_T - \omega_m$. For the charge qubit: $\chi = G_{tm}^2/\delta$ and $\Delta_m = \omega_m - \omega_d$. The last two drive terms corresponds to the mechanical

phonon pump and the qubit spectroscopy, respectively. Using the master equation Eq, (1.43), the qubit excitation probability P_e can be generated. The qubit spectra, revealing the phonon spectrum, is shown in the Fig. 1.6. For a weak dispersive coupling ($\chi < \gamma$), the dispersive pull is from the average phonon occupancy $2\chi\langle\hat{m}^\dagger\hat{m}\rangle$, while in the case of a strong dispersive coupling $\chi > \gamma$, the pull from each Fock state is resolved. Observe that as the average phonon number increases, the linewidth broadening in the qubit spectrum also increases. In fact, the distribution of the spectrum changes from the Lorentzian to the Gaussian, and the linewidth scales from $\bar{m}$ to $(\bar{m})^{1/2}$ [2]. The dispersive coupling can be employed to generate Bell-cat states in the

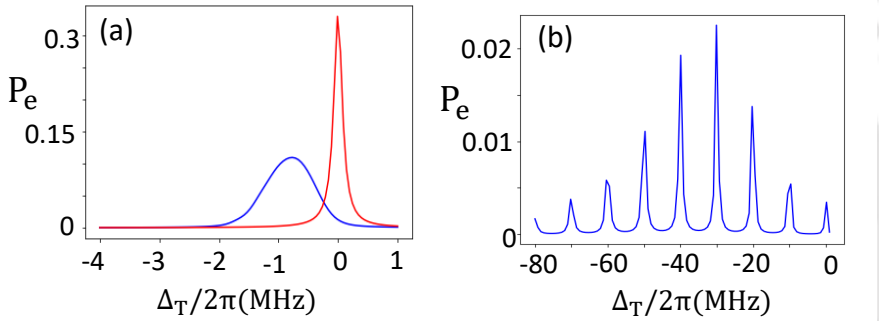

Figure 1.6: (a)Dispersive shift of the qubit frequency for a weak coupling. (b) Strong dispersive coupling shift resolving the phonon number distribution of the resonator. Parameters: (a) $\Omega_R/2\pi = 0.1$MHz, $\epsilon/2\pi = 0.2$MHz, $\gamma/2\pi = \Gamma/2\pi = 0.1$MHz $\chi/2\pi = 0.08$MHz and $\Delta_m = 0$. (b) $\Omega_R/2\pi = 0.1$MHz, $\epsilon/2\pi = 0.1$MHz, $\chi/2\pi = 5$MHz and $\Delta_m = \chi$.

qubit-mechanical system, as well as cat states of the mechanical system. To create the Bell-cat state, the qubit is initially prepared in the superposition state, $|\psi\rangle = (1/2)(|e\rangle + |g\rangle)$ by applying a $\pi/2$ pulse through the gate voltage while the mechanical resonator is prepared in the vacuum state, $|0\rangle$. In the absence of dissipation, the combined system, $|\Psi\rangle_0 = |\psi\rangle|0\rangle$, evolves unitarily under the dispersive interaction given by the first two terms in Eq. (1.45). The state of the combined system after some time $t = \pi/\chi$ yields the Bell-cat state,

$$|\Psi\rangle = (|-\beta\rangle|e\rangle + |\beta\rangle|g\rangle)/\sqrt{2}, \tag{1.47}$$

where $|\beta\rangle$ is the coherent state of the resonator. The energy of the ground state is assumed to be zero. Utilizing the Bell-cat state preparation scheme

discussed above, we study the generation of bipartite Bell-cat state of two mechanical resonators in Chapter 2. By applying another $\pi/2$ rotation to the qubit, the state $|\Psi\rangle$ transform to

$$|\Psi\rangle = \frac{1}{2\sqrt{2}}\left[\left(|-\beta\rangle - |\beta\rangle\right)|e\rangle + \left(|\beta\rangle + |-\beta\rangle\right)|g\rangle\right]. \tag{1.48}$$

Measuring the qubit in the excited (ground) state will project the mechanical resonator in the cat state $|-\beta\rangle - |\beta\rangle$ $(|-\beta\rangle + |\beta\rangle)$. Therefore, using the dispersive interaction the mechanical resonator can be prepared in the cat state.

1.6.2 Longitudinal Coupling

The longitudinal coupling between the qubit and the resonator arises from the Josephson energy term of the transmon or charge qubit. As previously discussed, the Josephson energy E_J can be varied by threading an external flux through the SQUID loop formed by two split Josephson junctions. This external flux is applied via a dedicated on-chip flux line. Extending this concept, we can induce a flux in a SQUID loop by allowing one arm of the loop to be movable. This movable arm can oscillate out of the plane when subjected to an in-plane magnetic field, effectively acting as the resonator. By connecting another SQUID loop, which represents the qubit, to this motional SQUID loop, the Josephson energy is modified as $E_J = E_J(\Phi_e) + E_J(x)$, where

$$E_J(x) = E_{Jx}[c_J\, cos(\pi\Phi_x/\Phi_0) - s_J\, sin(\pi\Phi_x/\Phi_0)\alpha\hat{x}] \tag{1.49}$$

and,

$$c_J = (1 + a_J^2\, tan(\pi\Phi_x/\Phi_0))^2, \quad s_J = (1 - a_J^2)/c_J, \quad \alpha = \pi\beta_0 Bl/\Phi_0. \tag{1.50}$$

Here, $a_J = (E_2 - E_1)/(E_1 + E_2)$ is the junction asymmetry. B, l and $\hat{x}$ are the applied magnetic filed strength, length of the movable arm and the displacement of the moving arm, respectively. Φ_x is the external flux bias applied on the movable SQUID loop. The first term in Eq. 1.49 modifies the transmon frequency and the second term results in the interaction between the qubit and the resonator. Replacing the E_J term in Eq. 1.16, with $E_J = E_J(\Phi_e) + E_J(x)$, we get the transmon qubit-mechanical longitudinal interaction Hamiltonian,

$$\hat{H}_L = \hbar\frac{\Omega_{Tx}}{2}\hat{\sigma}_z + \hbar\omega_m\hat{m}^\dagger\hat{m} + \hbar G_L(\hat{m}^\dagger + \hat{m})\sigma_z. \tag{1.51}$$

$\Omega_{Tx} = \sqrt{8E'_J E_c} - E_c$, where $E'_J = E_J + E_{Jx}\, c_J\, cos(\pi\Phi_x/\Phi_0)$, is the modified qubit frequency. The coupling constant G_L is dependent on s_J as $G_L = G_0 s_J\, sin(\pi\Phi_x/\Phi_0)$, where G_0 comprises other constant parameters. The higher order interactions are excluded while deriving Eq. 1.51 since their contribution in the system dynamics is negligible [97].

The longitudinal interaction can be used to encode qubit information in the mechanical resonator state. To implement this we first give a weak ac bias such that the coupling constant changes to $G_L \rightarrow G_L cos(\omega_m t)$ [98, 99]. Transforming into the interaction frame and retaining the rotating wave approximation, Hamiltonian 1.51 reduces to

$$\hat{H}_L = \hbar\frac{\Omega_{Tx}}{2}\hat{\sigma}_z + \hbar G_L(\hat{m}^\dagger + \hat{m})\sigma_z. \tag{1.52}$$

The system evolves as $|\Psi_{tm}(t)\rangle = U(t)|\Psi\rangle_0$, where $U(t) = exp[-iG_L\sigma_z(\hat{m}^\dagger + \hat{m})]$ and $|\Psi\rangle_0$ is the initial state of the system. If the qubit is prepared in the ground state and the mechanical resonator in the vacuum state then after some time t the system evolve to $|\Psi_{Tm}(t)\rangle = |g\rangle|iG_L t\rangle$. Here, $|iG_L t\rangle$ is a coherent state of amplitude $\beta = iG_L t$. When the qubit is prepared in the ground state and the mechanical resonator in the vacuum state then after some time t the system evolve to $|\Psi_{tm}(t)\rangle = |e\rangle| - iG_L t\rangle$. Thus, the qubit state is encoded or associated with the coherent excitation of the resonator. The expectation value of coherent displacement of the resonator corresponding to the ground or excited state of the qubit is given by $\langle\hat{a}\rangle = \pm iG_L t$. More discussion on this topic can be found in Chapter 5. In the presence of dissipation, the evolution of the system can be evaluated by solving the master equation.

Another important application of longitudinal coupling is to cool the mechanical resonator to its ground state. Assuming that the qubit reaches a steady state much faster than the resonator ($G_L << \Gamma$), we can adiabatically eliminate the qubit dynamics. This results in an asymmetric addition of decay rates to the mechanical resonator, leading to its cooling. For a more detailed discussion, refer to Chapter 3.

1.7 Optomechanical Coupling

In this section, we will discuss the integration of an optical channel or cavity into the electromechanical system, forming a hybrid electro-optomechanical system (refer Fig. 1.7). Depending on the types of electromechanical systems

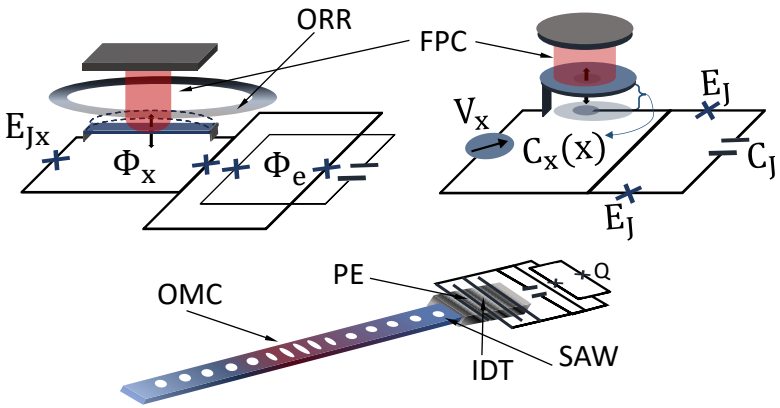

Figure 1.7: Schematic of the Electro-Optomechanical System: For a suspended mechanical beam (top left), the optical mode can be coupled to the mechanical mode by either forming a Fabry-Pérot cavity (FPC) with the beam acting as an end mirror or by placing an optical ring resonator (ORR) near the beam, where the optical resonator field picks up the vibrational signal from the beam. A suspended membrane also couples with the optical mode by forming a Fabry-Pérot cavity (top right). In an optomechanical crystal (OMC), the mechanical mode within the crystal couples with the confined optical mode through the photoelastic effect (bottom). In all three cases, the qubit couples with the optical mode through mechanical-optical coupling [11, 13, 14, 100, 101].

discussed in the previous section, the optical part can be integrated in different ways. For a longitudinal qubit-mechanical coupling type, the optical cavity can be coupled to the resonator through an optical ring resonator fabricated on the same chip hosting the qubit and the mechanical resonator, or through a Fabry-Perot cavity. In both coupling schemes, the displacement of the resonator alters the resonant frequency of the optical cavity (ω_a), resulting in a mechanical-optical interaction term. Taking the displacement up to the linear part, the frequency shift of the optical cavity can be expanded to $\omega_c(\hat{x}) = \omega_a + (\partial\omega_c/\partial\hat{x})\hat{x}$ [100]. Writing the displacement in terms of the creation and annihilation operators $\hat{a}^\dagger$ and $\hat{a}$, respectively, the Hamiltonian of the total electro-optomechanical system reads

$$\hat{H}_{elo} = \hbar\frac{\Omega_{Tx}}{2}\hat{\sigma}_z + \hbar\omega_m\hat{m}^\dagger\hat{m} + \hbar G_L(\hat{m}^\dagger + \hat{m})\sigma_z + \hbar\hat{a}^\dagger\hat{a}\omega_a + \hbar g\hat{a}^\dagger\hat{a}(\hat{m}^\dagger + \hat{m}), \quad (1.53)$$

where $g = X_{ZPF}\partial\omega_c/\partial\hat{x}$ is the single photon optomechanical coupling strength. The shift in the cavity frequency is due to the back action of the force imparted by the photons in the cavity to the mechanical resonator [102–105]. This force is referred to as the radiation pressure force and is given by $F = -\partial\hat{H}_{elo}/\partial\hat{x} = (\hbar g/X_{ZPF})\,\hat{a}^\dagger\hat{a}$. The force depends on the photon number present in the cavity; therefore, the more photons present, the greater the force imparted on the resonator, resulting in larger coupling. In a typical experiment, the single-photon coupling strength g is on the order of 1 Hz, which is very small compared to the frequency scale of the system. Since the radiation pressure force—and thus the coupling strength—can be increased by injecting more photons into the cavity, we enhance the optomechanical coupling by driving the cavity. To observe the driving effect, we first write down the Langevin equations for both the mechanical resonator and the cavity,

$$\dot{\hat{a}} = -\left(\frac{\kappa+\kappa_1}{2} + i\omega_a\right)\hat{a} - ig\hat{a}(\hat{m}^\dagger + \hat{m}) + \sqrt{\kappa_1}\hat{a}_{in1} + \sqrt{\kappa_2}\hat{a}_{in2}, \quad (1.54a)$$

$$\dot{\hat{m}} = -\left(\frac{\gamma}{2} + i\omega_m\right)\hat{m} - iG_L\hat{\sigma}_z - ig\hat{a}^\dagger\hat{a} + \sqrt{\gamma}\hat{m}_{in}. \quad (1.54b)$$

Here, κ, κ_1 and κ_2 are the decay rates corresponding to the intra cavity field, input field $\hat{a}_{in1}$ and intrinsic noise field $\hat{a}_{in2}$. $\hat{m}_{in}$ in the input noise of the resonator. The cavity is driven through the input port $\hat{a}_{in1}$. When the drive is strong, the input field can be separated into the quantum and classical parts: $\hat{a}_{in1} \to \hat{a}_{in1} + A(t)$, where $A(t)$ is the amplitude of the drive. Substituting in Eq. (1.54a), we have

$$\dot{\hat{a}} = -\left(\frac{\kappa+\kappa_1}{2} + i\omega_a\right)\hat{a} - ig\hat{a}(\hat{m}^\dagger + \hat{m}) + \sqrt{\kappa_1}(A(t) + \hat{a}_{in1}) + \sqrt{\kappa_2}\hat{a}_{in2}. \quad (1.55)$$

This change can be implemented in the Hamiltonian (1.56) by adding a drive term $\hat{H}_d = \hbar\sqrt{\kappa_1}A(t)(\hat{a}\,exp(-i\omega_d t) + \hat{a}^\dagger exp(i\omega_d t))$. The optical frequency is typically large (in THz) compared to the qubit and mechanical resonator and the drive term is time dependent. So, it is advisable to go in the drive frame. Therefore, we have

$$\hat{H}_{elo} = \hbar\frac{\Omega_{Tx}}{2}\hat{\sigma}_z + \hbar\omega_m\hat{m}^\dagger\hat{m} + \hbar G_L(\hat{m}^\dagger + \hat{m})\sigma_z + \hbar\hat{a}^\dagger\hat{a}\Delta_a + \hbar g\hat{a}^\dagger\hat{a}(\hat{m}^\dagger + \hat{m}) + \hbar\epsilon(t)(\hat{a}^\dagger + \hat{a}), \quad (1.56)$$

where $\Delta = \omega_a - \omega_d$ and $\epsilon(t) = \sqrt{\kappa}A(t)$. Since the drive is strong, the cavity is coherently populated with a large number of photons, and the system dynamics lean toward the classical regime. To isolate the quantum part, we separate the cavity field into classical (α) and quantum components: $\hat{a} \rightarrow \hat{a}+\alpha$. Similarly, the mechanical motion can be separated into quantum and classical (β) components:$\hat{m} \rightarrow \hat{m} + \beta$. The classical part of the mechanical motion is induced by the radiation pressure force exerted by the cavity photons. This separation into classical and quantum parts can be understood as the classical part representing a coherent displacement in phase space, while the quantum part represents small fluctuations around the displaced amplitude. The coherent amplitudes depends on the photon (phonon) number as $\alpha = \sqrt{n_a}$ ($\beta = \sqrt{n_m}$), n_a (n_m) is the average photon (phonon) number. The quantum part of the Langenvin equation after the classical-quantum separation is given by

$$\begin{aligned} \dot{\hat{a}} &= -\left(\frac{\kappa+\kappa_1}{2} + i\Delta_a + ig(\beta+\beta^*)\right)\hat{a} - ig\hat{a}(\hat{m}^\dagger + \hat{m}) \qquad (1.57a) \\ &\quad -ig\alpha(\hat{m}+\hat{m}^\dagger) + \sqrt{\kappa_1}\,\hat{a}_{in1} + \sqrt{\kappa_2}\,\hat{a}_{in2}, \\ \dot{\hat{m}} &= -\left(\frac{\gamma}{2} + i\omega_m\right)\hat{m} - iG_L\hat{\sigma}_z - ig(\alpha\hat{a}^\dagger + \alpha^*\hat{a}) - ig\hat{a}^\dagger\hat{a} \qquad (1.57b) \\ &\quad +\sqrt{\gamma}\,\hat{m}_{in} \end{aligned}$$

and the classical part by

$$\begin{aligned} \dot{\alpha} &= -\left(\frac{\kappa+\kappa_1}{2} + i\Delta_a + ig(\beta+\beta^*)\right)\alpha - i\epsilon, \qquad (1.58a) \\ \dot{\beta} &= -\left(\frac{\gamma}{2} + i\omega_m\right)\beta - ig\alpha\alpha^* \qquad (1.58b) \end{aligned}$$

In Eq. 1.57a, the linear term $-ig\alpha(\hat{m}+\hat{m}^\dagger)$ $(-ig(\alpha\hat{a}^\dagger + \alpha^*\hat{a})\,)$ is amplified by the amplitude α compared to nonlinear term $-ig\hat{a}(\hat{m}^\dagger + \hat{m})$ $(-ig\hat{a}^\dagger\hat{a})$. Therefore, we can ignore the nonlinear term and retain only the linear term. This is known as linearization. The corresponding linearized Hamiltonian can be written as

$$\begin{aligned} \hat{H}_{elo} &= \hbar\frac{\Omega_{Tx}}{2}\hat{\sigma}_z + \hbar\omega_m\hat{m}^\dagger\hat{m} + \hbar G_L(\hat{m}^\dagger + \hat{m})\hat{\sigma}_z + \qquad (1.59) \\ &\quad \hbar\hat{a}^\dagger\hat{a}\Delta_a + \hbar G_\alpha(\hat{a}^\dagger + \hat{a})(\hat{m}^\dagger + \hat{m}), \end{aligned}$$

where we have merged $\Delta \rightarrow \Delta_a + g(\beta+\beta^*)$ for simplicity. While substituting the classical and quantum parts, an extra term, $\hbar G_L(\beta^* + \beta)\sigma_z$ arises from

the third term of Eq. (1.56). Although this extra term is not visible in the Langevin equation (1.57a), it shows up in the qubit's dynamics. Since this term only shifts the qubit frequency, it is merged as, $\Omega_{Tx} \rightarrow \Omega_{Tx} + G_L(\beta^* + \beta)$.

The linearized dynamics of the cavity-mechanical or the optomechanical system can be written in matrix form as

$$\dot{\hat{u}} = A\hat{u} + \hat{u}_{in}, \tag{1.60}$$

where

$$A = \begin{bmatrix} -\left(\frac{\kappa+\kappa_1}{2} + i\Delta_a\right) & 0 & -iG_\alpha & -iG_\alpha \\ 0 & -\left(\frac{\kappa+\kappa_1}{2} - i\Delta_a\right) & 0 & iG_\alpha \\ -iG_\alpha^* & -iG_\alpha & -\left(\frac{\gamma}{2} + i\omega_m\right) & 0 \\ -iG_\alpha^* & -iG_\alpha & 0 & -\left(\frac{\gamma}{2} - i\omega_m\right) \end{bmatrix},$$

$\hat{u} = [\hat{a},\, \hat{a}^\dagger,\, \hat{m}^\dagger, \hat{m}]^{-1}$, $\hat{u}_{in} = [\sqrt{\kappa_1}\hat{a}_{in1},\, \sqrt{\kappa_2}\hat{a}_{in2},\, \sqrt{\kappa_1}\hat{a}^\dagger_{in1},\, \sqrt{\kappa_2}\hat{a}^\dagger_{in2},\, \sqrt{\gamma}\hat{m}_{in},\, \sqrt{\gamma}\hat{m}^\dagger_{in}]^{-1}$ and

$$B = \begin{bmatrix} -\sqrt{\kappa_1} & -\sqrt{\kappa_2} & 0 & 0 & 0 & 0 \\ 0 & 0 & -\sqrt{\kappa_1} & -\sqrt{\kappa_2}iG_\alpha & 0 & 0 \\ 0 & 0 & 0 & 0 & -\sqrt{\gamma} & 0 \\ 0 & 0 & 0 & 0 & 0 & -\sqrt{\gamma} \end{bmatrix}$$

We have switched off the qubit-mechanical coupling G_L to study the dynamics of the optomechanical system. This can be achieved in practice by turning off the externally applied weak AC bias. It is more useful to analyze the quantum linearized dynamics around the stable steady-state classical values obtained by substituting $\dot{\alpha} = \dot{\beta} = 0$. To find the stable state, we must choose the parameters so that the real eigenvalues of the Jacobian matrix A are all negative. Using the parameters that satisfy the stable steady states α_{ss} and β_{ss}, we solve the Eq. (1.60) in the Fourier domain. By applying Fourier transformation in Eq. (1.60), we get $\hat{u}(\omega) = -(i\omega I_4 - A)^{-1} B\, \hat{u}(\omega)_{in}$. Using the input-output relation $\hat{u}_{out} = B^T\hat{u} - \hat{u}_{in}$ [106–108], the output field, $\hat{u}_{out} = [\hat{a}_{out1},\, \hat{a}_{out2},\, \hat{a}^\dagger_{out1},\, \hat{a}^\dagger_{out2}\, \hat{m}_{out}, \hat{m}^\dagger_{out}]^{-1}$, can be written as

$$\hat{u}(\omega)_{out} = S\hat{u}(\omega)_{in}, \tag{1.61}$$

where S is the scattering matrix given by $S = B^T(-i\omega I_4 - A)^{-1}B - I_6$. The intra cavity photon, $\hat{a}$, interacts with the mechanical resonator, and any changes in the cavity photon behavior due to this interaction are measured

by detecting the reflected signal, given by the ratio $\hat{a}_{out1}/\hat{a}_{in1}$. Alternatively, any signal transferred from the mechanical resonator can be measured by determining the transmitted signal, represented by the ratio $\hat{a}_{out1}/\hat{m}_{in}$. These two ratios can be found out from the $\hat{a}_{out}$ relation obtained from Eq. (1.61), i.e.,

$$\hat{a}_{out1} = S_{11}\hat{a}_{in1} + S_{12}\hat{a}_{in2} + S_{13}\hat{a}^{\dagger}_{in1} + S_{14}\hat{a}^{\dagger}_{in2} + S_{15}\hat{m}_{in} + S_{16}\hat{m}^{\dagger}_{in}. \quad (1.62)$$

The reflected and the transmitted signals are given by the scattering matrix elements S_{11} and S_{15}. The reflected signal can be obtained for two different cavity drives. The first is the red-detuned cavity drive, where the drive frequency is less than the cavity frequency, specifically by an amount equal to the resonator frequency, i.e., $\Delta_a = \omega_m$. The second one is the blue-detuned cavity driv,e where the drive frequency exceeds the cavity frequency, $\Delta_a = -\omega_m$. Note that the drive referred here is not the input field, $\hat{a}_{in}$, but rather the one driven with amplitude $A(t)$ and frequency ω_d. exhibits different behaviors for the two drives. To observe this, we transform the interaction term given by the last term of Eq. (1.59) into the interaction frame:

$$\begin{aligned} \hat{H}_{int} &= \hbar G_\alpha(\hat{a}^{\dagger}\hat{m}e^{i(\Delta_a-\omega_m)} + \hat{m}^{\dagger}\hat{a}e^{-i(\Delta_a-\omega_m)} \\ &\quad + \hat{a}\hat{m}e^{-i(\Delta_a+\omega_m)} + \hat{a}^{\dagger}\hat{m}^{\dagger}e^{i(\Delta_a+\omega_m)}). \end{aligned} \quad (1.63)$$

Assuming rotating wave approximation for $\omega_m, \Delta_a >> G_\alpha$, the red-detuned drive interaction reduces to $\hbar G_\alpha(\hat{m}^{\dagger}\hat{a}+\hat{a}^{\dagger}\hat{m})$ and the blue-detuned to $\hbar G_\alpha(\hat{a}\hat{m}+\hat{m}^{\dagger}\hat{a}^{\dagger})$ showing different interaction behaviour.

In the red-detuned laser drive to the cavity, the reflected signal reads

$$S_{11} = \frac{i(\omega-\Delta_a) - \frac{\kappa-\kappa}{2} + \frac{G_\alpha^2}{i(\omega-\omega_m)-\gamma/2}}{i(\omega-\Delta_a) - \frac{\kappa+\kappa}{2} + \frac{G\alpha^2}{i(\omega-\omega_m)-\gamma/2}}. \quad (1.64)$$

As shown in the Fig. 1.8, the dip in the reflected signal for weak coupling is observed at $\omega = \omega_m = \Delta_a$, which means that the drive red shifts (Stokes scattering) the cavity frequency by an amount equal to the resonator frequency. Similarly, in the blue detuning case, the dip in the reflected signal given by

$$S_{22} = \frac{i(\omega+\Delta_a) - \frac{\kappa-\kappa}{2} + \frac{G_\alpha^2}{i(\omega-\omega_m)-\gamma/2}}{i(\omega+\Delta_a) - \frac{\kappa+\kappa}{2} + \frac{G_\alpha^2}{i(\omega-\omega_m)-\gamma/2}}. \quad (1.65)$$

is observed at $\omega = \omega_m = -\Delta_a$, indicating blue shift (anti-stokes scattering) of the cavity frequency by an amount equal to the resonator frequency. The

red-detuned interaction, also known as the beam-splitter interaction, can be used for state transfer between the resonator and the cavity. Suppose that the resonator receives a signal from the qubit while their interaction is active. This signal can then be transmitted to the optical photons using the beam-splitter interaction. The transmitted signal,

$$S_{15} = \frac{iG_\alpha^2(\kappa_1\gamma)^{1/2}(\kappa/2 - i(\omega - \Delta_a)\,)^{-1}(\gamma/2 - i(\omega - \omega_a)\,)^{-1}}{1 + G_\alpha^2(\kappa/2 - i(\omega - \Delta_a)\,)^{-1}(\gamma/2 - i(\omega - \omega_a)\,)^{-1}}, \tag{1.66}$$

for a weak coupling is shown in the Fig. 1.8. The peak of the signal is observed at $\omega = \omega_m$. In both the reflected and transmitted signals, we observe two peaks or dips around the mechanical frequency when the coupling is strong ($\kappa << G_\alpha$). These peaks or dips indicate normal mode splitting, with the separation between them being $2G_\alpha$ [34, 100, 106]. In Chapter 5, we will study the quantum transduction of a qubit to an optical photon using the hybrid electro-optomechanical system. The beam-splitter interaction discussed above, along with the longitudinal qubit-mechanical interaction, is employed to realize this transduction.

The blue-detuned interaction, also referred to as parametric down-conversion interaction, is used to produce two-mode squeezing and entanglement between the mechanical resonator and the optical cavity [109–112]. This entangled system can be utilized for transferring quantum states through quantum teleportation [107,113]. Recent studies have harnessed such entangled interactions in electro-optomechanical systems to achieve quantum transduction from microwave to optical signals [114].

A similar linearized Hamiltonian [(1.59)] can be derived for a transverse electro-optomechanical system by replacing the third term with the transverse interaction one.

$$\begin{aligned} \hat{H}'_{elo} &= \hbar\frac{\Omega_{Tx}}{2}\hat{\sigma}_z + \hbar\omega_m\hat{m}^\dagger\hat{m} + \hbar G_{tm}(\hat{m}^\dagger + \hat{m})\sigma_x + \\ &\quad \hbar\hat{a}^\dagger\hat{a}\Delta_a + \hbar G_\alpha(\hat{a}^\dagger + \hat{a})(\hat{m}^\dagger + \hat{m}), \end{aligned} \tag{1.67}$$

Under the rotating wave approximation, we get a Jaynes-Cumming and beam-splitter interaction Hamiltonian:

$$\begin{aligned} \hat{H}'_{elo} &= \hbar\frac{\Omega_{Tx}}{2}\hat{\sigma}_z + \hbar\omega_m\hat{m}^\dagger\hat{m} + \hbar G_{tm}(\hat{m}^\dagger\hat{\sigma}_- + \hat{m}\hat{\sigma}_+) + \\ &\quad \hbar\hat{a}^\dagger\hat{a}\Delta_a + \hbar G_\alpha(\hat{a}^\dagger\hat{m} + \hat{a}\hat{m}^\dagger). \end{aligned} \tag{1.68}$$

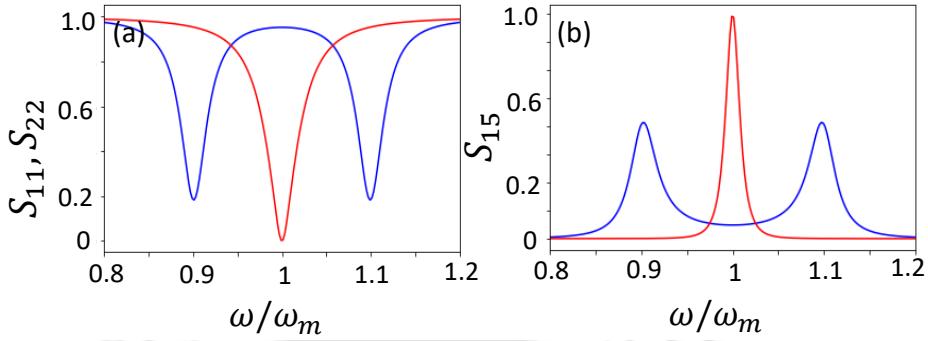

Figure 1.8: Reflection (a) and transmission (b) signals of the optical field. The signals are observed at the mechanical frequency. Red and blue curve corresponds to weak and strong coupling, respectively. Parameters: $\kappa/2\pi = 0.01\omega_m$, $\kappa_1/2\pi = 0.05\omega_m$, $\gamma/2\pi = 0.01\omega_m$ and $G_\alpha/2\pi = 0.01\omega_m$ for weak coupling and $G_\alpha/2\pi = 0.1\omega_m$ for strong coupling.

This interaction is ideal for transferring the qubit state to the optical photon, as both the qubit-mechanical and mechanical-optical couplings facilitate state swapping. Additionally, the non-rotating interaction Hamiltonians (1.59) and (1.67) depend on the displacement of the resonator. Consequently, the forces exerted on the resonator by the cavity and the qubit can be engineered to either amplify or reduce its amplitude. Using this principle, we demonstrate the cooling of resonator motion in Chapter 3.

1.8 Thesis Structure

An introductory discussion on the implementation of the hybrid system is presented in the previous sections. Below is a brief outline of the thesis, structured by chapters, where various quantum technological applications utilizing the hybrid system are explored.

In Chapter 2, we implement a dispersive qubit-mechanical interaction in a hybrid electromechanical system to generate bipartite mechanical cat states. This is achieved by piezoelectrically coupling two phononic crystals with separate qubits, connected through a microwave cavity, followed by a projective Bell test on the qubits. Furthermore, we conduct a Bell inequality test using the Clauser–Horne–Shimony–Holt (CHSH) formalism, demonstrating a violation of the inequality. The dependence of the level of violation on

coupling strength and decay rates is also analyzed.

Next, we explore the hybrid electro-optomechanical system across three phenomena. In Chapter 3, we demonstrate the cooling of a mechanical resonator to its ground state. While ground state cooling has been studied in individual qubit-mechanical and mechanical-optical cavity systems, it has not been explored in the combined system. This chapter focuses on cooling within this hybrid framework.

In Chapter 4, we analyze the bistability and synchronization of a qubit's polarization vector with an optical drive using quantum trajectory evolution. We achieve this by inducing oscillatory motion in the mechanical resonator through a blue-detuned laser drive applied to the cavity. Due to electromechanical coupling, the resonator exhibits two stable oscillations in phase space, and corresponding to each oscillation, the qubit stabilizes one of the polarization vectors for a single quantum trajectory evolution. The phase of this polarization vector on the Bloch sphere synchronizes with the drive phase

In Chapter 5, we propose a scheme for quantum transduction that maps the qubit's state onto the cavity's photon occupation number. This process occurs in two steps: the qubit-mechanical coupling is activated to map the qubit's states to the resonator's excitation, and then the resonator-cavity coupling is turned on. Through beam-splitting coupling, the resonator's excitation is transferred to the cavity photons.

We summarize all our works in chapter 6, highlighting its applications and limitations, and discuss potential near-future applications as well as avenues for further research.

2

Generation of Bipartite Mechanical Cat State.

In this chapter, we use the hybrid electromechanical system to generate four bipartite phononic cat states using an entanglement swapping scheme achieved through projective Bell state measurements on two superconducting qubits. The use of two superconducting qubits allows for the creation of bipartite phononic cat states remotely, where the two phononic resonators are separated by a far distance. Subsequently, we conduct a Bell inequality test on the bipartite cat state using the CHSH formulation. Given that the entangled cat states are generated through entanglement swapping, our approach holds promising applications for the advancement of complex quantum network processors based on continuous variable systems.

The quantum properties of solid-state mechanical systems have been routinely demonstrated in recent experiments [115–117]. These include interfacing mechanical objects with the strong quantum nonlinearity of superconducting qubits, leading to the field of circuit quantum acoustodynamics (cQAD) [25–31], which is analogous to the well-established field of circuit quantum electrodynamics (cQED) [1–8]. The integration of superconducting qubits acts as a quantum-acoustic state preparation and measurement element for the mechanical system, forming basic building blocks for constructing

An article based on this chapter is published in Phys. Rev. A **110**, 023726 (2024), titled "*Generation of a bipartite mechanical cat state by performing projective Bell-state measurement on a pair of superconducting qubits*" and authored by Roson Nongthombam, Urmimala Dewan, and Amarendra K. Sarma.(©2024 American Physical Society). The contents in this chapter are used with permission.

acoustic quantum memories and processors.

A particularly significant quantum-acoustic state that can be prepared from the superconducting qubit-mechanical integrated system is the phononic Schrödinger cat state, defined as quantum superpositions of quasi-classical coherent states. Such preparations have been studied in [118,119], and similar photonic cat states have been explored in various quantum systems, including circuit quantum electrodynamics [120, 121], vibrational states of trapped ions [122, 123], and propagating photon modes [124, 125].

The preparation of cat states has attracted wide research attention due to their applications in quantum metrology [126], quantum information processing protocols based on continuous-variable cat states [127], and testing fundamental quantum phenomena in macroscopic systems [128]. One of the most fundamental tests of quantum phenomena is the Bell inequality test [129–132]. These tests, performed on pairs of spatially separated entangled quantum systems, demonstrate that quantum systems do not adhere to the principle of local causality. In this work, we employ the Clauser–Horne–Shimony–Holt (CHSH) [133] formulation of the Bell test to conduct the Bell inequality test on a bipartite entangled phononic cat state generated through projective Bell state measurement on a pair of superconducting qubits [134]. The creation of bipartite photonic cat states using a single qubit has been demonstrated in [121, 125]. In our scheme, four bipartite phononic cat states, or four

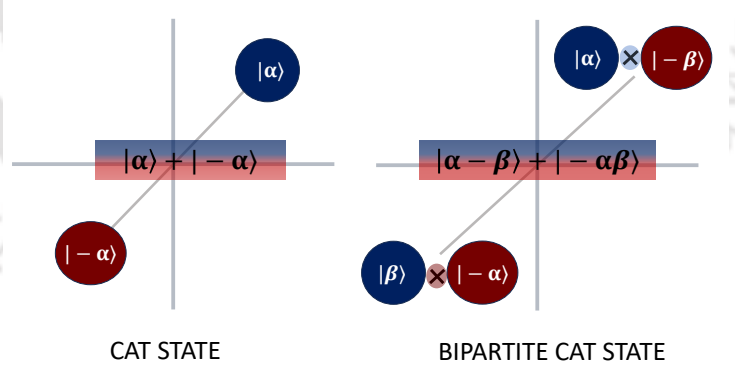

Figure 2.1: Schematic diagram of cat state and bipartite cat state. The cat state is formed by superposing two coherent states of a single resonator while the bipartite cat state is formed by entangling coherent states of two resonators.

phononic Bell states, are generated on two phononic crystal mechanical

resonators, interacting piezoelectrically with a pair of superconducting qubits via capacitive coupling. The two qubits are connected through a microwave cavity resonator, and through virtual excitation of the cavity photon, they become entangled, creating qubit Bell state. Upon projective measurement of the Bell state of the qubits, each of the four bipartite phononic cat states can be distinguished. This measurement effectively swaps the entanglement from qubit-mechanical to mechanical-mechanical pairs. Such entanglement swapping schemes are pivotal in quantum repeaters, essential for realizing long-distance quantum communication and complex quantum networks [135–137]. Since the two qubits are connected via a microwave cavity bus, the phononic crystal resonator can be placed at far ends. This setup allows for the creation of bipartite phononic cat states remotely, enabling long-distance quantum state preparation. Furthermore, we use the Clauser–Horne–Shimony–Holt (CHSH) formulation of the Bell test to conduct the Bell inequality test on the bipartite phononic cat states.

2.1 System Model and Brief Analysis

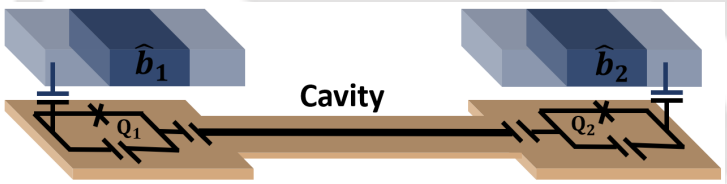

Figure 2.2: Schematic of the hybrid qubit-resonator system. Two qubits denoted by Q_1 and Q_2 are capacitively coupled to the phononic crystal resonators $\hat{b}_1$ and $\hat{b}_2$, respectively. The qubits interact piezoelectrically with the resonators. The two qubits are coupled to each other via a microwave cavity resonator. This coupling enables the interaction between the two qubits by exchanging virtual excitations of the cavity photons.

We consider two hybrid electromechanical systems, each comprising a mechanical resonator dispersively coupled to a superconducting qubit as shown in Fig. 2.2. The Hamiltonian of the two hybrid systems are given by

$$\hat{H}_{bq1} = \frac{\hbar}{2}\Omega_1|e_1\rangle\langle e_1| + \frac{\hbar\omega_1}{2}\hat{b}_1^\dagger\hat{b}_1 + \hbar\lambda_1\,\hat{b}_1^\dagger\hat{b}_1\,|e_1\rangle\langle e_1|, \tag{2.1a}$$

$$\hat{H}_{bq2} = \frac{\hbar}{2}\Omega_2|e_2\rangle\langle e_2| + \frac{\hbar\omega_2}{2}\hat{b}_2^\dagger\hat{b}_2 + \hbar\lambda_2\,\hat{b}_2^\dagger\hat{b}_2\,|e_2\rangle\langle e_2|. \tag{2.1b}$$

Here, Ω_1 (Ω_2) and ω_1 (ω_2) are the qubit and mechanical frequencies of the first (second) hybrid system. $\hat{b}_1$ and $\hat{b}_2$ are the operators of the two mechanical resonators. $\lambda_1 = g_1^2/\delta_1$ and $\lambda_2 = g_2^2/\delta_2$ are the dispersive shift of the qubits. In dispersive coupling, the detuning $\delta_1 = \omega_1 - \Omega_1$ ($\delta_2 = \omega_2 - \Omega_2$) is much larger than the resonant coupling strength between the qubit and the mechanical resonator. The two superconducting qubits are connected through a microwave cavity. By detuning the qubits with respect to the cavity, we can realize the $\sqrt{iSWAP}$ gate.

$$\hat{H}_s = \hbar(\eta_1\hat{\sigma}_z^1 + \eta_2\hat{\sigma}_z^2)\hat{a}^\dagger\hat{a} + \hbar J(\hat{\sigma}_1^-\hat{\sigma}_2^+ + \hat{\sigma}_1^+\hat{\sigma}_2^-) \tag{2.2}$$

where $\eta_1 = G_1^2/\Delta_1$, $\eta_2 = G_2^2/\Delta_2$ and $J = G_1G_2(1/\Delta_1 - 1/\Delta_2)$ (($\delta_1 = \omega_1 - \Omega_1$) and ($\Delta_2 = \omega - \Omega_2$)). $\hat{a}$ and $\hat{a}^\dagger$ are the creation and annihilation operators of the cavity resonator. $\hat{\sigma}_z^i$, $\hat{\sigma}_i^-$ and $\hat{\sigma}_i^+$ where $i = 1, 2$ are the operators of the two qubits. If we start the cavity in the vacuum state, the terms containing $\hat{a}^\dagger\hat{a}$ can be ignored. The Hamiltonian (2.1) and (2.2) can be realized in separate instances by tuning the qubits at different frequencies at different times (Fig. 2.5(c). We first entangle the qubit-mechanical pair using the Hamiltonian (2.1), and then perform a Bell state measurement on the qubits by switching on the interaction (2.2). This measurement induces entanglement of the two resonators, even though they were not initially interacting. A schematic of this protocol is shown in Fig. 2.3. In the following sections, we provide a detailed explanation of how this protocol is realized.

2.2 Qubit-Mechanical Entanglement.

We first prepare two entangled Bell-cat states by evolving the Hamiltonian (2.1). Initiating the qubits in the superposition state and the mechanical resonators in the coherent state, the state of the first hybrid system ($\hat{H}_{bq1}$) in the interaction frame after some time t becomes

$$|\psi\rangle_1 = (|\beta_1 e^{i\lambda_1 t}\rangle|e_1\rangle + |\beta_1\rangle|g_1\rangle)/\sqrt{2}, \tag{2.3}$$

where $|\beta_1\rangle$ is the coherent state of the first mechanical resonator, while $|e_1\rangle$ and $|g_1\rangle$ refer to the excited and the ground states of the first qubit, respectively. We get a similar state $|\psi\rangle_2$ for the second hybrid system. In the time interval $t = (2n-1)\pi/\lambda_1$, where $n = 1, 2, 3...$, we get the Bell-cat state of the qubit-mechanical system.

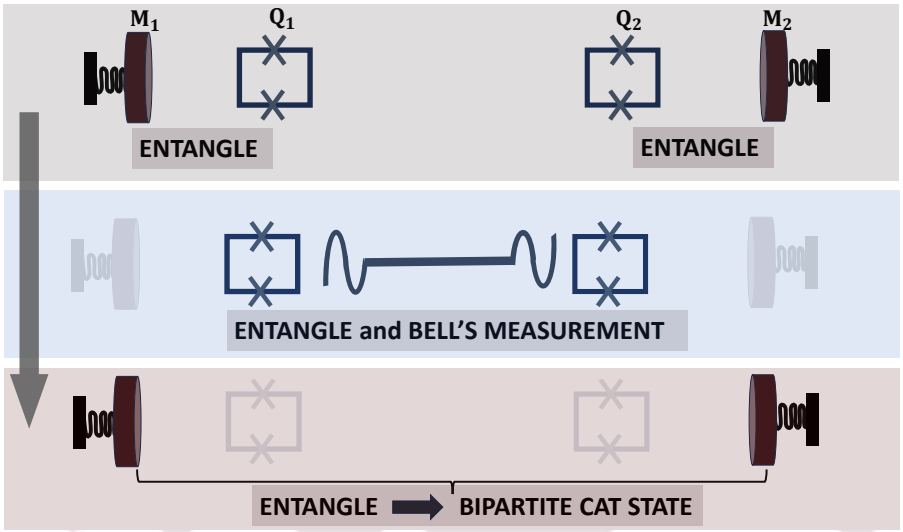

Figure 2.3: The schematic illustrates different qubit operations used for generating the bipartite cat state. The qubit-mechanical system pairs are first entangled separately. Next, the interaction between the mechanical resonator and the qubit is switched off, allowing for qubit-qubit interaction. By performing a projective Bell state measurement on the entangled qubits, the two resonators are projected onto different bipartite cat states.

The fidelity and entanglement of the bipartite state $|\psi\rangle_1$ in the presence of a noisy environment is shown in Fig. 2.3. The noisy environment is included by solving the Lindblad master equation.

$$\begin{aligned}\dot{\hat{\rho}}_1 &= -\frac{i}{\hbar}[\hat{H}_{int}, \hat{\rho}_1] + \gamma_1(n_1+1)\mathcal{L}[\hat{b}_1] + \gamma_1 n_1 \mathcal{L}[\hat{b}_1^\dagger] \\ &\quad + \Gamma_1 \mathcal{L}\left[\hat{\sigma}_-\right] + \Gamma_1 \mathcal{L}\left[\hat{\sigma}_+\right] + \Gamma_1 \mathcal{L}\left[\hat{\sigma}_z\right], \end{aligned} \tag{2.4}$$

where $\mathcal{L}[\hat{o}] = (2\hat{o}\hat{\rho}\hat{o}^\dagger - \hat{o}^\dagger\hat{o}\hat{\rho} - \hat{\rho}\hat{o}^\dagger\hat{o})/2$ with $\hat{o} \in \{\hat{b}_1, \hat{\sigma}_-, \hat{\sigma}_z\}$. γ_1 and Γ_1 are the decay rates of the mechanical resonator and the qubit, respectively. The entanglement of the mechanical bipartite qubit system is computed using the relation $E_N(\hat{\rho}_1) = log_2||\hat{\rho}_1^{T_A}||$, where $\hat{\rho}_1^{T_A}$ is the trace norm of the partial transpose of the mixed bipartite state $\hat{\rho}_1$ [138, 139]. As shown in the figure, the fidelity (F) reaches near one at the interval $t = 0.39\mu s$, $1.18\mu s$, and so on for coupling constant $\lambda_1 = 8$MHz. Therefore, the qubit-mechanical bipartite system evolves into a Bell-cat state at the interval of π.

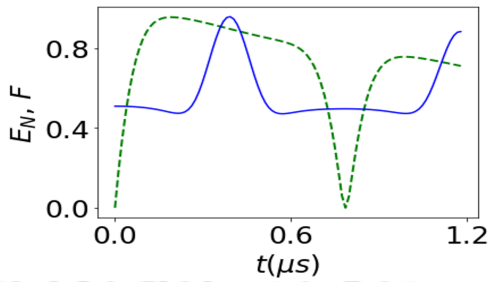

Figure 2.4: Entanglement E_N (green dotted line) and fidelity F (solid blue line) measurement of the state $|\psi\rangle_1$ in the presence of thermal noise. As expected, the state $|\psi\rangle_1$ evolves into the Bell cat state $|\psi\rangle_1 = (|-\beta_1\rangle|e_1\rangle + |\beta_1\rangle|g_1\rangle)/\sqrt{2}$ at the interval π/λ_1, $3\pi/\lambda_1$,... etc. The parameters used are $\beta_1 = \sqrt{2}$, $\gamma_1 = 0.1$MHz, $\Gamma_1 = 0.1$MHz, $n_{th} = 0.03$, and $\lambda_1 = 8$MHz.

2.3 Generation of Bipartite Cat State.

After the interaction time of $t_1 = \pi/\lambda_1$ ($t_2 = \pi/\lambda_2$), the state of the qubit-mechanical bipartite state (Eq.(2.3)) become $|\psi\rangle_1 = (|-\beta_1\rangle|e_1\rangle + |\beta_1\rangle|g_1\rangle)/\sqrt{2}$ ($|\psi\rangle_2 = (|-\beta_2\rangle|e_2\rangle + |\beta_2\rangle|g_2\rangle)/\sqrt{2}$). The state of the combined system $|\Psi\rangle$ is then given by the tensor product of the states of the two hybrid systems, i.e.,$|\Psi\rangle = |\psi\rangle_1|\psi\rangle_2$

$$\begin{aligned} |\Psi\rangle \;=\; & \frac{1}{2\sqrt{2}}[|\phi^+\rangle(|-\beta_1-\beta_2\rangle - i|\beta_1\,\beta_2\rangle) \\ & +|\phi^-\rangle(|-\beta_1-\beta_2\rangle + i|\beta_1\,\beta_2\rangle) \\ & +|\psi^+\rangle(|-\beta_1\,\beta_2\rangle - i|\beta_1-\beta_2\rangle) \\ & +|\psi^-\rangle(|-\beta_1\,\beta_2\rangle + i|\beta_1-\beta_2\rangle)]. \end{aligned} \tag{2.5}$$

where $|\beta_2\rangle$ is the coherent amplitude of the second resonator. We have written the state in terms of Bell's basis, $|\phi^\pm\rangle = (1/\sqrt{2})(|e_1e_2\rangle \pm i|g_1g_2\rangle)$ and $|\psi^\pm\rangle = (1/\sqrt{2})(|e_1g_2\rangle \pm i|g_1e_2\rangle)$. By measuring the Bell's states $|\phi^\pm\rangle$ and $|\psi^\pm\rangle$, the two mechanical resonators are projected into the bipartite cat states $|C'_\mp\rangle = \mathcal{N}'_\mp(|-\beta_1-\beta_2\rangle \mp i|\beta_1\,\beta_2\rangle)$ and $|C_\mp\rangle = \mathcal{N}_\mp(|-\beta_1\,\beta_2\rangle \mp i|\beta_1-\beta_2\rangle)$, respectively. We perform the Bell state measurement by switching on the interaction (2.2). This interaction only produces two of the four Bell states, $|\psi^\pm\rangle$. To generate all four Bell states, we continuously drive the two qubits, resulting in two dressed states $|\pm\rangle_j = (1/\sqrt{(2)})(|g\rangle_j \pm e^{i\Phi_j}|e\rangle_j)$, $j = 1, 2$. The qubit cannot go into transitions between different dressed states under the

conditions $\Phi_1 = \Phi_2 = \Phi$ and $|A_1 - A_2| >> |J'|$, where A_j and Φ_j are the drive amplitude and phase. When the phases of both the driving fields are reversed right in the middle of the two-qubit interaction time, then the dressed state of the two qubit evolves to $|++\rangle_\tau = (1/2)(i|\phi^-\rangle + |\phi^+\rangle + i|\psi^-\rangle + |\psi^+\rangle)$, where $\tau = \pi/(2J')$. The above protocol for producing the dressed state $|++\rangle_\tau$ is known as dressed-state phase gate. In Fig. 2.5(a)(b), we plot the fidelity of the dressed state generated through the dressed-state phase gate. The four Bell state generated through the dressed-state phase gate can be mapped onto the computational basis as $|\phi^+\rangle \rightarrow (0_1 0_2)$, $|\phi^-\rangle \rightarrow (1_1 1_2)$, $|\psi^+\rangle \rightarrow (1_1 0_2)$, and $|\psi^-\rangle \rightarrow (0_1 1_2)$ [134, 140] (Appendix (A.2)). Therefore, based on the measurement outcomes of the two qubits in the computational basis, all four bipartite cat states of the resonators are generated.

The sequence of operations to generate the bipartite cat state is illustrated in Fig. 2.5(c). As shown in the figure, the qubits Q_1 and Q_2 are initially prepared in a superposition state by applying a $\pi/2$ pulse. Similarly, the mechanical resonators M_1 and M_2 are prepared in coherent states $|\beta_1\rangle$ and $|\beta_2\rangle$ by driving them on resonance with a microwave drive. The qubit-mechanical dispersive interaction is then initiated by detuning the qubits to δ_1 and δ_2 with respect to the resonators. After a time $t_1 = t_2 = \pi/\lambda_{1,2}$, the qubits are returned to their idle frequencies, terminating the dispersive interaction. Next, the qubit-qubit interaction is activated by detuning the qubits to Δ_1 and Δ_2 with respect to the microwave resonator R. After a time $\tau = \pi/2J'$, the qubits are again returned to their idle frequencies, and Bell state measurements commence. During this time τ, the qubits are continuously driven, generating the Dressed-state phase gate.

The above protocol is realized in the noisy environment by first independently evolving the two qubit-mechanical hybrid systems under the Lindblad master equation and then performing the projective measurement on the density matrix of the combined system, $\hat{\rho} = \hat{\rho}_1 \hat{\rho}_2$. The reduced density matrices of the four bipartite Bell-cat states after the projective Bell state measurement on the two qubits read as,

$$\begin{aligned} \hat{\rho}_{C'_\mp} &= \frac{\langle \phi^\pm | \hat{\rho} | \phi^\pm \rangle}{tr(\langle \phi^\pm | \hat{\rho} | \phi^\pm \rangle)}, \\ \hat{\rho}_{C_\mp} &= \frac{\langle \psi^\pm | \hat{\rho} | \psi^\pm \rangle}{tr(\langle \psi^\pm | \hat{\rho} | \psi^\pm \rangle)}. \end{aligned} \tag{2.6}$$

We now reconstruct the density matrix into a two-level system subspace by projecting into the basis state $(|\beta_{1,2}\rangle, |-\beta_{1,2}\rangle)$. The Pauli operators for the

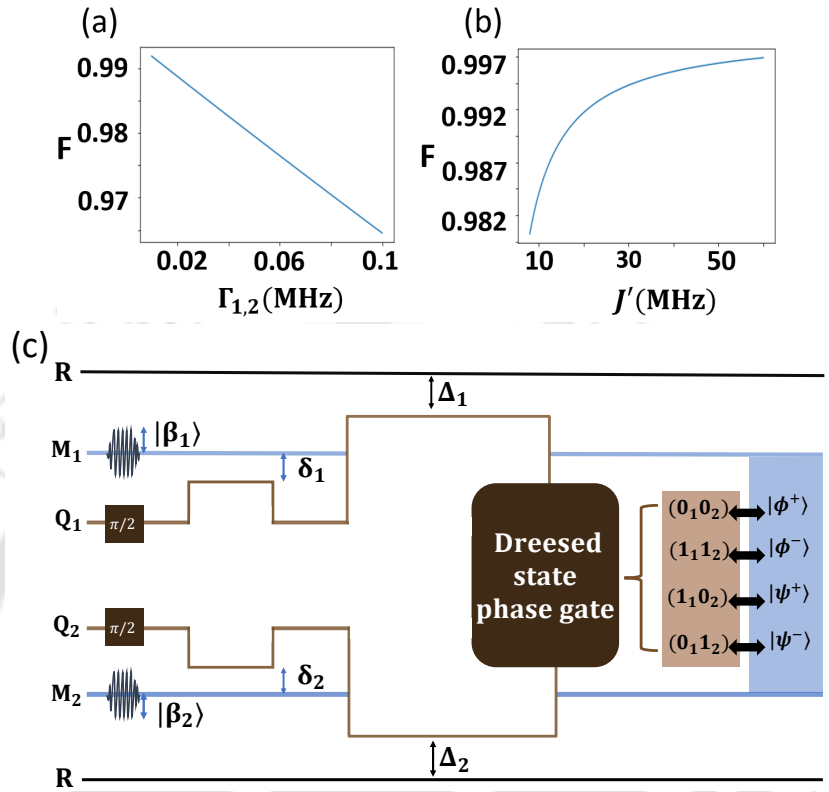

Figure 2.5: The change in fidelity of the dressed-state $|++\rangle_\tau$ with respect to decay rate $\Gamma_{1,2}$ and coupling strength J' are shown in (a) and (b), respectively. The coupling strength in (a) is $J' = 8$MHz and decay rates in (b) are $\Gamma_{1,2} = 0.1$MHz. (c) Sequence of qubit detuning and Bell state preparation and measurement.

resonator can be obtained by measuring the displaced phonon number parity observable $\hat{P}_{\beta_1} = \hat{D}_{\beta_1}\hat{P}\hat{D}^\dagger_{\beta_1}$, where $\hat{D}_{\beta_1}$ is the displacement operator and $\hat{P}$ the phonon number parity operator [27, 128]. The Pauli operators for the resonator mode become

$$\begin{aligned} \hat{X}_{\beta_1} &= \hat{P}_0, \quad \hat{I}_{\beta_1} = [\hat{P}_{\beta_1} + \hat{P}_{-\beta_1}], \\ \hat{Y}_{\beta_1} &= \hat{P}_{\frac{-i\pi}{8\beta_1^*}}, \quad \hat{Z}_{\beta_1} = [\hat{P}_{\beta_1} - \hat{P}_{-\beta_1}]. \end{aligned} \tag{2.7}$$

We have assumed a large orthonormal cat state, i.e., $\langle\beta_1| - \beta_1\rangle << 1$. Four Wigner functions ($W(\alpha) = \frac{2}{\pi}\langle P_\alpha\rangle$), where ($\alpha = 0, \beta, -\beta, -i\pi/8\beta^*$) are required to reconstruct the state. The basis for the Pauli operators is ($|\beta_1\rangle$, $|-\beta_1\rangle$) which is analogous to the qubit basis ($|e\rangle$, $|g\rangle$). Similar Pauli

operators and basis ($|\beta_2\rangle$, $|-\beta_2\rangle$) can be generated for the second resonator using the same approach. In Fig. 2.6, we plot the joint density matrix of the two resonators in the joint basis states ($|\beta_1\,\beta_2\rangle$, $|-\beta_1\,\beta_2\rangle$, $|\beta_1\,-\beta_2\rangle$, and $|-\beta_1\,-\beta_2\rangle$).

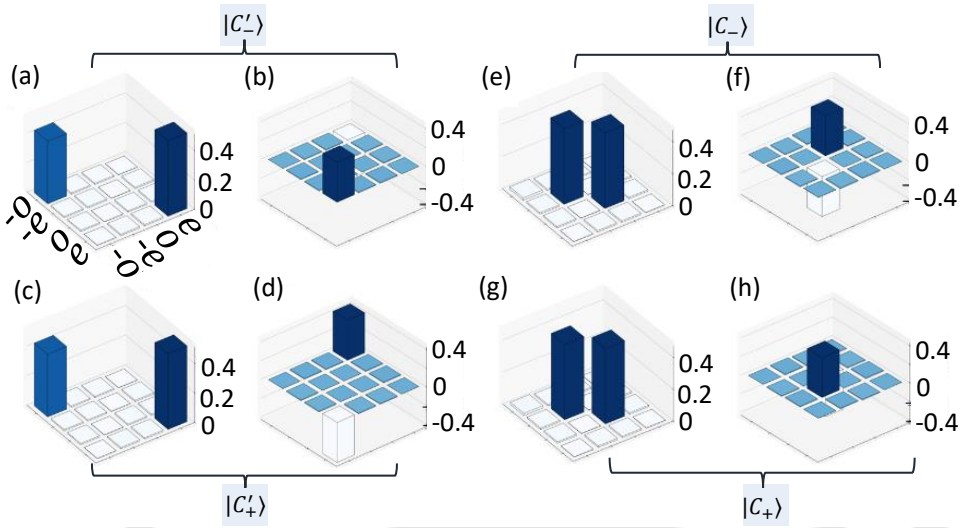

Figure 2.6: Construction of the four bipartite phononic cat states density matrices in the two-level subspace. The basis e, o, $-e$, and $-o$ represents the states $|\beta_1, \beta_2\rangle$, $|\beta_1, -\beta_2\rangle$, $|-\beta_1, \beta_2\rangle$, and $|-\beta_1, -\beta_2\rangle$, respectively. The density matrices resemble those of the two-qubit Bell state [134]. We have used the resonator coherent amplitudes $\beta_{1,2} = \sqrt{2}$.

We observe four bipartite cat states having fidelities $F_{C'_-} = 0.919$, $F_{C'_+} = 0.919$, $F_{C_-} = 0.92$, and $F_{C_+} = 0.92$ and entanglements $E_{C'_-} = 0.799$, $E_{C'_+} = 0.799$, $E_{C_-} = 0.799$, and $E_{C_+} = 0.799$. The dip in the density matrix element is mainly attributed to the relaxation and decoherence effect of the two qubits as well as the relaxation of the two resonators. As shown in Fig. 2.7, the fidelity of the bipartite cat state can be significantly improved by improving the decay rates of both the qubit and the phononic resonator. For example, we get $F_{C'_-} = 0.9581$, $F_{C'_+} = 0.9581$, $F_{C_-} = 0.9581$, and $F_{C_+} = 0.9581$ and entanglements $E_{C'_-} = 0.895$, $E_{C'_+} = 0.895$, $E_{C_-} = 0.895$, and $E_{C_+} = 0.895$ for decay rates $\gamma_{1,2} = 0.05$MHz and $\Gamma_{1,2} = 0.05$MHz. In Fig. 2.7, we have generated the fidelity variation for $|C_+\rangle$ state. We get similar plots for the other cat states too.

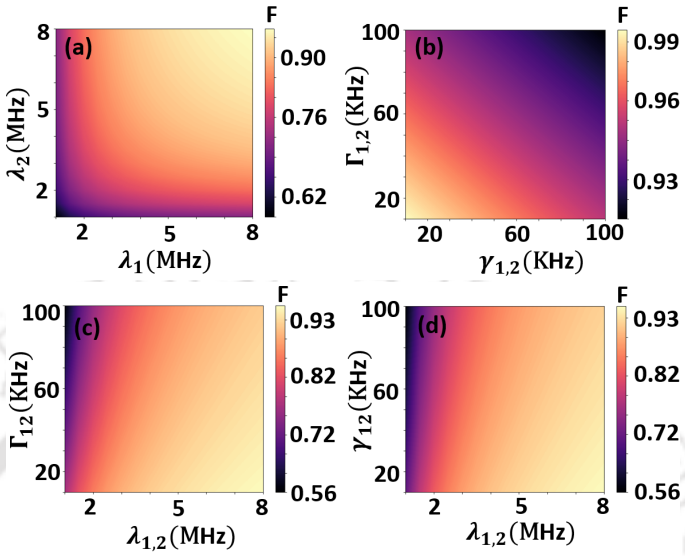

Figure 2.7: Fidelity of the bipartite cat state $|C_+\rangle$ as a function of (a) λ_1 and λ_2, (b) γ_1 and Γ_1, (c) Γ_1 and λ_1, (d) λ_1 and γ_1. The decay rates in (a) are $\gamma_{1,2} = 0.1$MHz and $\Gamma_{1,2} = 0.1$MHz. The coupling strength in (b) are $\lambda_{1,2} = 8$MHz. In (c), the decay rates of first and second resonators are $\gamma_{1,2} = 0.1$MHz. The qubits decay rate in (d) are $\Gamma_{1,2} = 0.1$MHz.

2.4 Bell's Test of the Resonator Bipartite Cat State

We perform Bell's inequality test by calculating the expectation values of all the correlations of the measurement outcomes measured locally at the two resonators and then determine the Clauser–Horne–Shimony–Holt (CHSH) value $S = \langle X_1 X_2\rangle + \langle X_1 Y_2\rangle - \langle Y_1 X_2\rangle + \langle Y_1 Y_2\rangle$, where, X_1 (X_2) and Y_1 (Y_2) are the observables of the first (second) resonator. As per CHSH inequality, a system is said to be classically correlated if $|S| \leq 2$ and quantumly if $2 < |S| \leq 2\sqrt{2}$. The correlation of the observables is measured by first choosing two arbitrary values of β_1' and β_2' corresponding to X_1, Y_1 and X_2, Y_2, respectively. We then rotate the resonator detector basis by coherently displacing the observables X_1 and Y_1 to $X_\alpha = D_{-i\alpha} X_1 D_{i\alpha}$ and $Y_\alpha = D_{-i\alpha} Y_1 D_{i\alpha}$ or

$$\begin{aligned} X_\alpha &= X_1\, cos2(\alpha\beta_1'^{*} + \alpha^*\beta_1') + Y_1 sin2(\alpha\beta_1'^{*} + \alpha^*\beta_1'), \\ Y_\alpha &= Y_1\, cos2(\alpha\beta_1'^{*} + \alpha^*\beta_1') - X_1 sin2(\alpha\beta_1'^{*} + \alpha^*\beta_1'). \end{aligned} \tag{2.8}$$

Here, α is the coherent displacement amplitude of the resonator. By changing the amplitude α, we are able to rotate the measurement basis direction and perform measurements at all possible orientations of the detectors. The $|S|$ value for the state $|C_+\rangle$ is shown in Fig. 2.8(b).

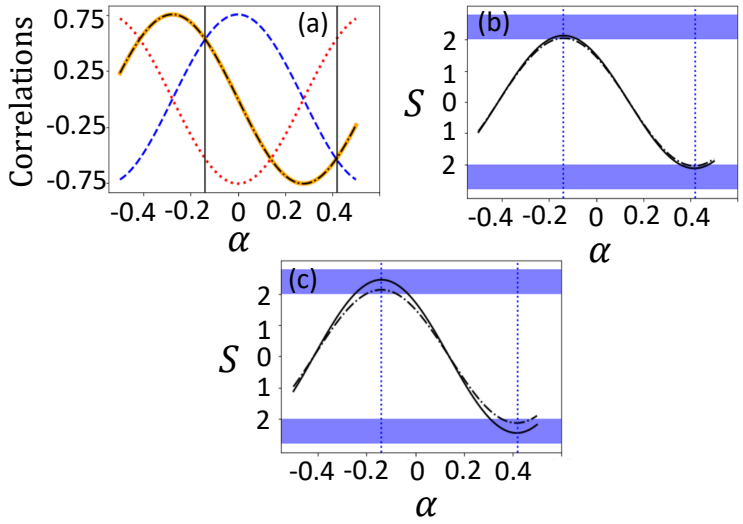

Figure 2.8: (a) The expectation values of all the joint measurement correlations between the two resonators. The red dotted, blue dashed, black dashed-dotted, and solid orange lines represent the measurement correlations $\langle Y_\alpha X_2\rangle$, $\langle X_\alpha Y_2\rangle$, $\langle Y_\alpha Y_2\rangle$, and $\langle X_\alpha X_2\rangle$, respectively. In (b), the CHSH value S of the Bell inequality is shown. The solid and dashed-dotted lines correspond to the coupling strengths $\lambda_1 = \lambda_2 = 8$ MHz and $\lambda_1 = \lambda_2 = 7$ MHz, respectively. For both cases, the maximum $|S|$ values occur at $\alpha_1 = -0.14$ and $\alpha_2 = 0.41$, denoted by the two dotted vertical lines, with corresponding values of 2.132 and 2.049. The decay rates in (b) are $\gamma_{1,2} = 0.1$MHz and $\Gamma_{1,2} = 0.1$MHz. For different decay rates $\gamma_{1,2} = 0.05$MHz and $\Gamma_{1,2} = 0.05$MHz, we get $|S| = 2.454$ for $\lambda_1 = \lambda_2 = 8$ MHz, as shown in (c) (solid line). The dashed-dotted line in (c) is for $\gamma_{1,2} = 0.1$MHz, $\Gamma_{1,2} = 0.1$MHz and $\lambda_1 = \lambda_2 = 8$ MHz, which is similar to the solid line in (b). The shaded horizontal lines represent the regions of the quantum limit.

We observe maximum $|S|$ value when $\beta'_{1,2} = \beta_{1,2}$ and at the displacement amplitude $\alpha_1 = -0.14$ and $\alpha_2 = 0.41$. Furthermore, the α_1, α_2 and β'_1 amplitudes corresponding to the maximum $|S|$ value satisfy the relations $4\alpha_2\beta'_1 = 3\pi/4$ and $4\alpha_1\beta'_1 = -\pi/4$. The corresponding observables (Eq. 2.8)

at these amplitudes become $X_{\alpha_1} = (X_1 - Y_1)/\sqrt{2}$ and $Y_{\alpha_1} = (X_1 + Y_1)/\sqrt{2}$. Therefore, the $|S|$ value observed in the figure exceeds the classical bound limit and attains a value which is less than the ideal quantum bound limit $2\sqrt{2}$ (see Fig 2.8(b)(c)).

As we decrease the decay rates of the resonators and the qubits, the maximum attainable $|S|$ value also increases, as shown in Fig 2.8(c). The expectation values of all the joint measurement correlations between the two resonators are also shown in Fig. 2.8(a). The behaviour of these correlations as we change the displacement amplitude α resembles the one observed in two-qubit Bell test experiments [132].

2.5 Conclusion

In this chapter, we have studied a scheme to generate four bipartite phononic cat states by performing a projective Bell state measurement on two superconducting qubits. Initially uncoupled phononic crystal resonators, each coupled to a different superconducting qubit, become entangled through entanglement swapping from qubit-mechanical to mechanical-mechanical interactions. A displaced phonon parity measurement is conducted to generate the joint density matrix of the two resonators in the two-level subspace. These joint density matrices resemble those of traditional qubit Bell states generated using a Hadamard gate and a CNOT gate in a quantum circuit. Subsequently, we investigate the Bell inequality test using the CHSH formulation. The expectation values of the measurement correlations and the S values obtained in this work are akin to those observed in [132] for two superconducting qubits. The bipartite phononic cat states generated through entanglement swapping may be useful for implementing quantum network processors based on continuous variable resonators. Furthermore, the scheme presented here also serves as a platform for studying Bell inequality tests in continuous variable systems.

3

Ground State Cooling of Mechanical Resonator.

In this chapter, we study the ground state cooling of a mechanical resonator in a hybrid electro-optomechanical system. This hybrid system consist of a mechanical resonator (few Mhz frequency) simultaneously coupled to a superconducting qubit made up of a split Cooper pair box (CPB) and an optical cavity. The cooling process is driven by a red-detuned ac drive on the qubit and a laser drive on the optomechanical cavity. We analyze the cooling in the weak and strong coupling regimes for both individual mechanisms—qubit-assisted cooling and optomechanical cooling—as well as for the hybrid cooling, and we compare the results.

The realization of a macroscopic mechanical oscillator in the quantum regime has wide-ranging applications in studying fundamental physics and developing quantum technologies, from high-precision measurements to quantum information processing. To achieve this, the mechanical oscillator must be cooled to its quantum ground state. This process typically begins with cryogenic pre-cooling to a few thousand initial phonons, followed by further cooling through coupling to external dissipation sources.

Two particular sources of dissipation have been extensively studied both theoretically and experimentally: one from the interaction with a cavity field

An article based on this chapter is published in Phys. Rev. A **104**, 023509 (2021), titled "*Ground-state cooling of a mechanical oscillator via a hybrid electro-optomechanical system*" and authored by Roson Nongthombam, Ambaresh Sahoo, and Amarendra K. Sarma.(©2021 American Physical Society). The contents in this chapter are used with permission.

in an optomechanical system, and the other from coupling with a Cooper pair box (CPB) qubit. The first experimental demonstration of radiation-pressure cooling—or optomechanical cooling—of a mechanical oscillator using optical feedback was conducted by Cohadon, Heidmann, and Pinard in 1999 [141, 142], with subsequent experiments achieving much lower temperatures using the same approach [143–145]. In 2006, radiation pressure cooling of a micromechanical resonator down to an effective temperature of 10 mK was realized [146, 147]. Cooling in the resolved sideband regime was achieved in 2008 [148], and close-to-ground-state cooling in a cryogenically pre-cooled environment was later demonstrated [149–151].

Conversely, cooling a mechanical resonator using a superconducting qubit has also been studied [95, 152, 153]. Ground-state cooling of mechanical resonators using two transmon qubits relying on flux-mediated interactions has been theoretically investigated in [156]. Furthermore, it has been shown that cooling to the ground state is feasible with just one transmon coupled to the mechanical oscillator in the ultrastrong coupling regime [98]. In a recent experimental work, a superconducting qubit was used to cool a drumhead mechanical oscillator close to its ground state [157]. Here, we combine the two cooling approaches discussed above, studying the ground-state cooling of a mechanical resonator by simultaneously coupling it to an optical cavity field via radiation pressure and to a CPB qubit via a movable capacitive plate. We also compared the individual cooling methods—qubit-mechanical and mechanical-cavity cooling—with hybrid cooling. In the weak coupling regime, hybrid cooling proved to be more efficient than the individual systems within the resolved sideband resonator. Similarly, in the strong coupling regime, hybrid cooling also demonstrated greater effectiveness.

3.1 System Model and Brief Analysis

We consider a hybrid electro-optomechanical system consisting of a mechanical resonator that is simultaneously coupled to a superconducting qubit, formed by a split Cooper pair box (CPB), and an optical cavity. The interaction between the qubit and the resonator is achieved by suspending one of the capacitor plates connected to the qubit, allowing it to move. This movable plate serves as the mechanical resonator and acts as a movable mirror in a Fabry-Perot optomechanical cavity. Consequently, the mechanical resonator interacts with the optical photons in the cavity through the radiation pressure force exerted by the photons on the resonator. A schematic of the hybrid

system is shown in Fig. 3.1. The Hamiltonian of the system is given by

$$\begin{aligned}\hat{H} =& -\hbar\frac{\Delta_q}{2}\hat{\sigma}_z + \frac{1}{2}\hbar\Omega_R\,\sigma_x + \hbar G(\hat{b}^\dagger + \hat{b})\sigma_z + \hbar\Omega\,\hat{b}^\dagger\hat{b} \\ & - \hbar\Delta_c\hat{a}^\dagger\hat{a} + \hbar G_o(\hat{a}^\dagger + \hat{a})(\hat{b}^\dagger + \hat{b}),\end{aligned} \tag{3.1}$$

Here, $\Delta_q(\Delta_c)$, Ω_R and $\sigma_{x,z}$ are the detuning of the qubit (optical cavity), amplitude of the drive given to the qubit and Pauli operators of the qubit, respectively. $\hat{b}(\hat{a})$ and $\hat{b}^\dagger(\hat{a}^\dagger)$ are the operators of the mechanical resonator (optical cavity). G is the coupling strength between the qubit and the mechanical resonator, while G_0 is the coupling strength between the resonator and the optical cavity. Ω is the bare frequency of the resonator. Cooling of the resonator is achieved by applying a red-detuned drive to both the qubit and the optical cavity. Due to this red detuning, the qubit is excited to a higher energy level by absorbing incoming photons from the external drive as well as phonons from the mechanical oscillator. As a result, the mechanical resonator loses phonons to the qubit, leading to cooling. Simultaneously, optical photons enter the cavity by absorbing a phonon from the oscillator, further contributing to the cooling of the resonator. These two processes occur concurrently, enabling us to achieve ground state cooling of the mechanical resonator within the hybrid electro-optomechanical system.

Another way to understand the cooling mechanism is through the forces exerted on the mechanical resonator. From the Hamiltonian, the force exerted on the resonator by the qubit and the cavity is given by $\partial\hat{H}/\partial x = \hbar(G\hat{\sigma}_z + G_o(\hat{a} + \hat{a}^\dagger))/x_{zpf}$. This force can either amplify or decay the amplitude of the resonator. For weak coupling, the rates of these processes can be computed using the Fermi golden rule. The decay rate is given by $\Gamma_- = G^2S_{zz}(\Omega) + G_o^2S_{a+a^\dagger}(\Omega)$, where S_{zz} and $S_{a+a^\dagger}$ are the spectral noise density of qubit and the cavity at the resonator frequency. Conversely, the amplification rate is $\Gamma_+ = G^2S_{zz}(-\Omega) + G_o^2S_{a+a^\dagger}(-\Omega)$. Note that amplification occurs at the negative frequency of the spectral noise density. Cooling will happen when the decay rate exceeds the amplification rate, which can be achieved by driving the qubit and cavity at a frequency slightly less than their resonant frequency, equal to the mechanical frequency—this is known as red-detuned driving.

In the next section, we systematically derive the Eq. (3.1) and discuss the cooling process in detail.

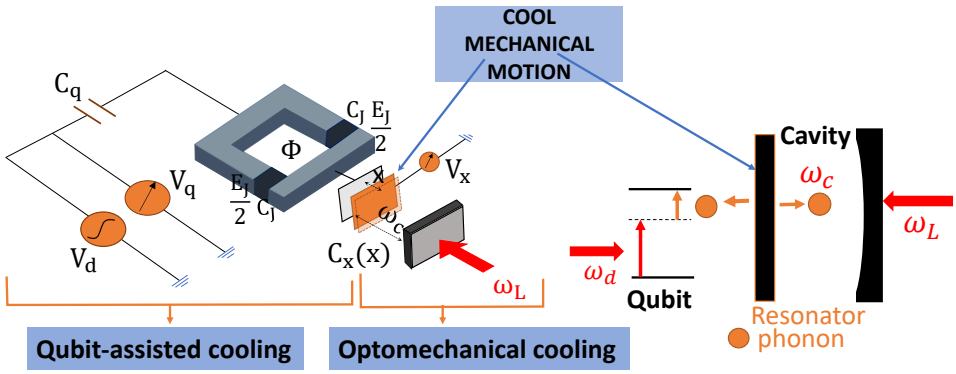

Figure 3.1: Hybrid CPB qubit-and optomechanical system. A split Cooper pair box (CPB) that is electrostatically biased by voltages V_q and V_x, and driven by a voltage V_d, is capacitively coupled to a mechanical mode via a movable capacitor $C_x(x)$. By applying an external flux Φ, the energy levels of the CPB qubit can be tuned. The mechanical mode is coupled to an optical cavity field ω_c, which is formed by placing a partially reflecting mirror in front of the movable capacitor plate. The optical cavity is driven by bright coherent light. On the right, a schematic description of the cooling process is shown.

3.2 System Hamiltonian Derivation.

The qubit-mechanical interaction arises from capacitive coupling, while the mechanical-optical cavity interaction originates from the radiation pressure force exerted by the cavity photons. The effective Hamiltonian can be expressed as follows:

$$\hat{H} = \frac{\left[\hat{Q} - Q_{xq}(x)\right]^2}{2C_\Sigma(x)} - E_J(\Phi_{\text{ext}})\cos\theta + \hbar\Omega\,\hat{b}^\dagger\hat{b} - \hbar\Delta_c\,\hat{a}^\dagger\hat{a} + \hbar g_o\,\hat{a}^\dagger\hat{a}\left(\hat{b}^\dagger + \hat{b}\right) + \hbar\eta\left(\hat{a}^\dagger + \hat{a}\right). \tag{3.2}$$

Here, $\hat{Q} = 2e\hat{N}$ (in the number basis), where $\hat{N}$ is the number operator for the Cooper pairs transferred across the Josephson junction in the superconducting qubit (Cooper pair box). $Q_{xq}(x) = 2eN_{xq}(x)$, where $N_{xq}(x) = N_x(x) + N_q$, is the offset charge or gate charge produced by external gate voltages $V_x = 2eN_x(x)/C_x(x)$ and $V_q = 2eN_q/C_q$ which induces Cooper pairs to tunnel

through the Josephson junction, and hence control the charge and state of the CPB. It is apparent that this offset charge is dependent on the resonator displacement x. $C_\Sigma(x) = 2C_J + C_q + C_x(x)$ is the total capacitance of the qubit. $E_J(\Phi_{\text{ext}})\cos\theta$ is the effective field in the two parallel junctions, each with energy $E_J/2$. Φ_{ext} is the external flux applied in the loop formed by the two junctions. Here, θ is the phase difference between the junction and $E_J(\Phi_{\text{ext}}) = E_J\cos(\pi\Phi_{\text{ext}}/\Phi_o)$. The movable capacitor in the system acts as a mechanical oscillator with frequency Ω and is described by the third term in the Hamiltonian. This movable capacitor and a partially reflecting mirror placed in front of it form an optomechanical system. The last three terms in Eq. (3.2) describe the optomechanical system in the driven frame. Here, $\Delta_c(=\omega_L - \omega_c)$ is the detuning between the laser drive (ω_L) and the cavity (ω_c). The last-second term describes the coupling between an optical mode ($\hat{a}$) in the cavity and a mechanical mode ($\hat{b}$) via optomechanical coupling rate g_o. The last term is the laser drive with amplitude η.

At the gate charge close to an odd number of electron charges, i.e., $N_{xq}(x) = N_x(x) + N_q + 1/2 - \Delta N$, where $|\Delta N| \ll 1/2$, the first two energy levels of the Josephson junction are very close compared to the higher ones. Therefore, we can use a two-level approximation in this region, thereby forming a qubit. If we coherently drive the qubit at frequency ω_d and amplitude Ω_R, then we obtain the Hamiltonian of the hybrid system as (Appendix (A.1))

$$\begin{aligned}\hat{H} = &-\frac{\hbar\Delta_q}{2}\sigma_z + \frac{1}{2}\hbar\Omega_R\,\sigma_x\cos\varphi + \hbar g(\hat{b}^\dagger + \hat{b})\sigma_z\sin\varphi \\ &+ \hbar\frac{g^2}{\omega_q}(2\hat{b}^\dagger\hat{b} + 1)\sigma_z\cos^2\varphi + \hbar\Omega\,\hat{b}^\dagger\hat{b} - \hbar\Delta_c\,\hat{a}^\dagger\hat{a} \\ &+ g_o\hbar\hat{a}^\dagger\hat{a}(\hat{b}^\dagger + \hat{b}) + \hbar\eta(\hat{a}^\dagger + \hat{a}).\end{aligned} \tag{3.3}$$

The optomechanical coupling rate g_o is usually smaller than the mechanical and optical decay rates γ and κ. One common approach to address this issue is to drive the optical cavity using strong coherent light. This drive significantly increases the radiation pressure force, and hence the optomechanical coupling rate. It also induces a classical steady-state displacement of both the intracavity field and, through the optomechanical coupling, the mechanical mode. In order to remove this steady-state displacement and retain only the quantum fluctuation part, the following transformation can be performed

$$\hat{a} \to \alpha + \hat{a} \quad \text{and} \quad \hat{b} \to \beta + \hat{b}, \tag{3.4}$$

where α and β are the steady-state displacements of the intracavity field and mechanical mode. Substituting Eq. (3.4) into Eq. (3.3) and removing the constant terms, we get

$$\begin{aligned}\hat{H} = &-\hbar\frac{\Delta_q}{2}\sigma_z + \frac{1}{2}\hbar\Omega_R\,\sigma_x\cos\varphi + \hbar g(\hat{b}^\dagger + \hat{b})\sigma_z\sin\varphi \\ &+ \frac{2\hbar g^2\beta}{\omega_q}(\hat{b}^\dagger + \hat{b})\sigma_z\cos^2\varphi + \frac{2\hbar g^2}{\omega_q}\hat{b}^\dagger\hat{b}\sigma_z\cos^2\varphi - \hbar\Delta_c\hat{a}^\dagger\hat{a} \\ &+ \hbar g_o[\alpha(\hat{a}^\dagger + \hat{a}) + \hat{a}^\dagger\hat{a}](\hat{b}^\dagger + \hat{b}) + \hbar\Omega\,\hat{b}^\dagger\hat{b} + H_a + H_b, \end{aligned} \tag{3.5}$$

where

$$\begin{aligned}\Delta_q &\Rightarrow \Delta_q - \frac{4g^2\beta}{\omega_q}\cos^2\varphi|\beta|^2 - 2g\beta\sin\varphi \\ \Delta_c &\Rightarrow \Delta_c - 2g_o\beta. \end{aligned} \tag{3.6}$$

Here, α and β are real values (see below). The last two terms in Eq. (3.5) constitute the terms that are proportional to $\hat{a}$, $\hat{a}^\dagger$, $\hat{b}$ and $\hat{b}^\dagger$. The fourth and fifth terms are the qubit and oscillator interaction terms. Two observations can be made when we compare these two interacting terms. Firstly, the fourth term is amplified by the steady-state displacement of the mechanical oscillator β. Secondly, while the fourth term involves the product of two operators and therefore constitutes a second-order nonlinearity, the fifth term involves the product of three operators and therefore constitutes a third-order nonlinearity. The same observations can also be deduced for the seventh term. However, in this case, the coupling is between the optical photon and mechanical phonon, and the second-order nonlinear coupling is amplified by the coherent amplitude α. Because the second-order nonlinear interaction terms are amplified, we neglect the third-order interaction. The resultant Hamilonian is known as the *linearized Hamiltonian:*

$$\begin{aligned}\hat{H} = &-\hbar\frac{\Delta_q}{2}\sigma_z + \frac{1}{2}\hbar\Omega_R\,\sigma_x + \hbar G(\hat{b}^\dagger + \hat{b})\sigma_z + \hbar\Omega\,\hat{b}^\dagger\hat{b} \\ &- \hbar\Delta_c\hat{a}^\dagger\hat{a} + \hbar G_o(\hat{a}^\dagger + \hat{a})(\hat{b}^\dagger + \hat{b}) + H_a + H_b, \end{aligned} \tag{3.7}$$

where $G = g\sin\varphi + \frac{2g^2\beta}{\omega_q}\cos^2\varphi$, $G_o = g_o\alpha$, and $\Omega_R \to \Omega_R\cos\varphi$. We observe that in the presence of the steady-state mechanical displacement β - induced through optical drive - the coupling rate between the qubit and the oscillator increases by a factor $(2g^2\beta/\omega_q)\cos^2\varphi$. Similarly, the optomechanical coupling rate is amplified to $g_o\alpha$.

3.3 Cooling

We analyze the cooling of the resonator by considering the Hamiltonian presented in Eq. (3.7) and examining two distinct regimes: the weak coupling regime and the strong coupling regime. To understand the system dynamics in the presence of a thermal environment, we employ the Lindblad master equation. Therefore, the Lindblad master equation for the hybrid system in the shifted frame ($\hat{a} \to \alpha + \hat{a}$, $\hat{b} \to \beta + \hat{b}$) reads

$$\begin{aligned}\frac{d\hat{\rho}}{dt} = -\frac{i}{\hbar}[\hat{H}, \hat{\rho}] + (\mathcal{L}_q + \mathcal{L}_m + \mathcal{L}_c)\hat{\rho} \\ + \frac{\kappa}{2}\alpha[\hat{a} - \hat{a}^\dagger, \hat{\rho}] + \frac{\gamma}{2}\beta[\hat{b} - \hat{b}^\dagger, \hat{\rho}],\end{aligned} \tag{3.8}$$

where

$$\begin{aligned}&\mathcal{L}_q = \Gamma(n_q + 1)D[\sigma_-](\hat{\rho}) + \Gamma n_q D[\sigma_+](\hat{\rho}) + \frac{\Gamma_d}{2}(\sigma_z\hat{\rho}\sigma_z - \hat{\rho}),\\ &\mathcal{L}_m = \gamma(n_{th} + 1)D[\hat{b}](\hat{\rho}) + \gamma n_{th}D[\hat{b}^\dagger](\hat{\rho}), \quad \mathcal{L}_c = \kappa D[\hat{a}](\hat{\rho}),\\ &\text{and} \quad D[\hat{A}] = \frac{1}{2}(2\hat{A}\hat{\rho}\hat{A}^\dagger - \hat{A}^\dagger\hat{A}\hat{\rho} - \hat{\rho}\hat{A}^\dagger\hat{A}).\end{aligned} \tag{3.9}$$

The density operator $\hat{\rho}$ is in the shifted frame. The decay rates Γ_d, Γ_d and γ can be found out from the noise correlations of gate voltage fluctuations or charge number fluctuations; $\delta\hat{N}_x$ and $\delta\hat{N}_q$. Similarly, the optical cavity decay rate κ can be derived from the noise correlation of tthe optical bath.

3.3.1 Weak Coupling

The weak coupling regime assumes $G_o \ll \kappa$ and $G \ll \Gamma$. The cavity optical field and the qubit can be adiabatical eliminated using the Nakajima-Zwanzig formalism [153–155]. Since the qubit and the cavity field are not coupled, we can eliminate them seperately. To eliminate the qubit, we first split the total density operator by means of a projection operator P and Q

$$\hat{\rho} = (P + Q)\hat{\rho}, \quad \text{and} \quad P + Q = I, \tag{3.10}$$

with P defined by

$$P\hat{\rho} = \hat{\rho}_{qss} \otimes \hat{\rho}_{om}, \qquad \hat{\rho}_{om} = tr_q[\hat{\rho}], \tag{3.11}$$

where $\hat{\rho}_{qss}$ is the steady-state density operator of the qubit, and $\hat{\rho}_{om}$ is the optomechanical density operator. Projecting Eq. (3.8) into P-space, the master equation reads

$$\begin{aligned} P\partial_t\hat{\rho} =& P[-i\Omega\hat{b}^\dagger\hat{b}, P\hat{\rho}] - \frac{i}{\hbar}P[H_a + H_b, P\hat{\rho}] \\ &+ P[i\Delta_c\hat{a}^\dagger\hat{a} - iG_o(\hat{a}^\dagger + \hat{a})(\hat{b}^\dagger + \hat{b}), P\hat{\rho}] \\ &+ P[-iG(\hat{b}^\dagger + \hat{b})\sigma_z, Q\hat{\rho} + P\hat{\rho}] \\ &+ P(\mathcal{L}_m + \mathcal{L}_c)P\hat{\rho} + P\frac{\gamma}{2}\beta[\hat{b} - \hat{b}^\dagger, P\hat{\rho}] \\ &+ P\frac{\kappa}{2}\alpha[\hat{a} - \hat{a}^\dagger, P\hat{\rho}]. \end{aligned} \tag{3.12}$$

Similarly, the master equation in the Q-space can be obtained by projecting Q operator. The steady-state displacements α and β are determined by equating the terms that are proportional to $\hat{a}$, $\hat{a}^\dagger$, $\hat{b}$ and $\hat{b}^\dagger$ to zero, separately

$$\alpha = \frac{\eta}{\Delta_c + i\kappa/2 - g_o(\beta + \beta^*)},\ \beta = \frac{g_o|\alpha|^2 + G\langle\sigma_z\rangle_s}{i\gamma/2 - \Omega}. \tag{3.13}$$

Here, $\langle\sigma_z\rangle_s = P\sigma_z$ is the steady-state expectation value of σ_z. For $g_o \ll 1$, $\Delta_c \gg \kappa$ and $\gamma/2 \ll \Omega$, we obtain $\beta = -(g_o|\alpha|^2 + G\langle\sigma_z\rangle_s)/\Omega$ and $\alpha = \eta/[\Delta_c - g_o(\beta + \beta^*)]$ which are real values. The master equation for the optomechanical system ($\hat{\rho}_{om}$) can be obtained by solving the coupled rate equations for $P\hat{\rho}$ and $Q\hat{\rho}$ [153]

$$\begin{aligned} \frac{d\hat{\rho}_{om}}{dt} =& -\frac{i}{\hbar}[\hat{H}_{om}, \hat{\rho}_{om}] + \{\Gamma_q^+ + \gamma n_{th}\}D[\hat{b}^\dagger](\hat{\rho}) \\ &+ \{\Gamma_q^- + \gamma(n_{th} + 1)\}D[\hat{b}](\hat{\rho}) + \kappa D[\hat{a}](\hat{\rho}), \end{aligned} \tag{3.14}$$

where

$$\begin{aligned} &\hat{H}_{om} = \hbar\Omega'\hat{b}^\dagger\hat{b} - \hbar\Delta_c\hat{a}^\dagger\hat{a} + \hbar G_o(\hat{a}^\dagger + \hat{a})(\hat{b}^\dagger + \hat{b}), \\ &\Gamma_q^- = 2G^2 Re\{S(\Omega)\},\ \ \Gamma_q^+ = 2G^2 Re\{S(-\Omega)\}, \\ &\text{and}\ \ \Omega' = \Omega + Im\{S(\Omega) + S(-\Omega)\}. \end{aligned} \tag{3.15}$$

The master equation (3.14) is correct only upto to the $O\{(G/\Gamma)^2, (\gamma\, n_m/\Gamma)^2\}$. The decay rate Γ_q^+ is responsible for heating, whereas Γ_q^- contributes to cooling. The half-sided spectral noise density $S(\omega)$ is defined as

$$S(\omega) = \int_0^\infty dt\, \mathrm{e}^{i\omega t}\langle\Delta\sigma_z(t)\Delta\sigma_z(0)\rangle, \tag{3.16}$$

where $\Delta\sigma_z = \sigma_z - \langle\sigma_z\rangle_s$. An approximate analytical expression for $Re\{S(\omega)\}$ near resonance condition $\sqrt{\Delta_q^2 + \Omega_R^2} = \Omega$ is derived in [153]. Fig. 3.2(a) shows the plot of $Re\{S(\omega)\}$ under red-detuning ($\Delta_q < 0$) and resonance condition. Two plots are shown in the figure, one for $\Gamma \gg \Gamma_d$, and the other for $\Gamma \approx \Gamma_d$. As shown in the figure, the difference between the peaks at $\pm\Omega$ is more when the relaxation rate Γ is much greater than the dephasing rate Γ_d. The master

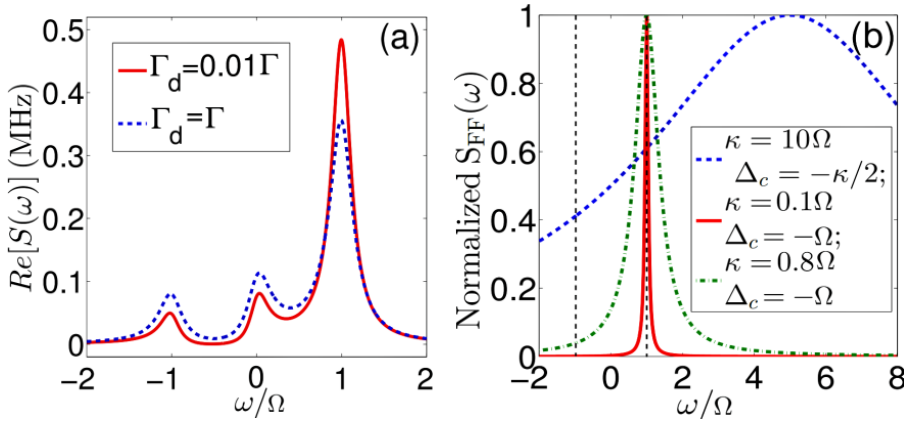

Figure 3.2: (a) The real part of the qubit spectral noise density is shown at the optimal cooling drive strength $\Omega_R = 0.85\Omega$ and resonance frequency $\bar{\Delta}_q = \Omega$. The parameters used for the plot are $\Omega = 10$ MHz and $\Gamma = 2$ MHz. The red solid curve represents the dephasing rate $\Gamma_d = 0.01\Gamma$, while the blue dotted curve corresponds to $\Gamma_d = \Gamma$ MHz. When $\Gamma \gg \Gamma_d$, the difference between the peaks at $\pm\Omega$ is larger, and the heating peak at $\Omega = -10$ MHz is smaller, indicating greater cooling. (b) The spectral noise density of the radiation force is depicted in both the resolved (solid red and dotted green curves) and unresolved sideband (dotted blue curve) regimes. The parameters used here correspond to those at the minimum quantum limit for cooling. The minimum quantum limit is attained at $\Delta_c = -\kappa/2$ in the unresolved sideband regime ($\kappa \gg \Omega$) and at $\Delta_c = -\Omega$ in the resolved sideband regime ($\kappa \ll \Omega$).

equation (3.14) contains the dynamics of both the mechanical oscillator and cavity optical field. The cavity field can be traced out and adiabatically eliminated using the same P and Q formalism

$$P\hat{\rho}_{om} = \hat{\rho}_{oss} \otimes \hat{\rho}_m, \qquad \hat{\rho}_m = tr_o[\hat{\rho}], \tag{3.17}$$

where $\hat{\rho}_{oss}$ is the steady-state density operator of the optical field, and $\hat{\rho}_m$ is the mechanical density operator. Analogous with the qubit elimination result, the elimination of the cavity field coherently shifts the mechanical frequency and adds two decay rates (Γ_o^- and Γ_o^+). The reduced master equation of the mechanical resonator in the interaction picture reads [154]

$$\begin{aligned}\frac{d\hat{\rho}_m}{dt} =&\{\Gamma_o^+ + \Gamma_q^+ + \gamma n_{th}\}D[\hat{b}^\dagger](\hat{\rho}) \\ &+ \{\Gamma_q^- + \Gamma_q^- + \gamma(n_{th}+1)\}D[\hat{b}](\hat{\rho})\end{aligned} \tag{3.18}$$

with

$$\Gamma_o^- = \frac{x_{ZPF}^2}{\hbar^2}S_{\rm FF}(\Omega), \text{ and } \Gamma_o^+ = \frac{x_{ZPF}^2}{\hbar^2}S_{\rm FF}(-\Omega), \tag{3.19}$$

where $S_{\rm FF}(\omega)$ is the spectral noise density of the radiative force $\hat{F}$ [$= (\hbar G/x_{\rm ZPF})(\hat{a}+\hat{a}^\dagger)$] acting on the mechanical oscillator.

$$S_{\rm FF}(\omega) = \int_{-\infty}^{\infty} dt\, e^{i\omega t}\langle \hat{F}(t)\hat{F}(0)\rangle \tag{3.20}$$

In Fig. 3.2(b), we plot $S_{\rm FF}(\omega)$ for the resolved ($\kappa = 0.1\,\Omega$, $\kappa = 0.8\,\Omega$) and unresolved ($\kappa = 10\,\Omega$) sideband in the red-detuning case. The expectation value of the phonon occupation number can be calculated from Eq. (3.18)

$$\langle \dot{\hat{n}}_m\rangle = -(\gamma + \Gamma_o + \Gamma_q)\langle \hat{n}_m\rangle + \gamma n_{th} + \Gamma_o^+ + \Gamma_q^-, \tag{3.21}$$

where $\Gamma_q = \Gamma_q^- - \Gamma_q^+$ and $\Gamma_o = \Gamma_o^- - \Gamma_o^+$ are the cooling rates contributed from the qubit and optical cavity field, respectively.

$$\begin{aligned}\Gamma_q =&2G^2[Re\{S(\Omega)\} - Re\{S(-\Omega)\}], \\ \Gamma_o =&\frac{x_{\rm ZPF}^2}{\hbar^2}[S_{\rm FF}(\Omega) - S_{\rm FF}(-\Omega)]\end{aligned} \tag{3.22}$$

For effective cooling, the cooling rates [Eq. (3.22)] must be positive. This condition is met if the external drive of the qubit and optical cavity are red-detuned with respect to the qubit energy level and optical resonance, respectively (see Fig. 3.2). Therefore, in both the cases, phonons are emitted, thereby cooling the mechanical oscillator. However, there is also a finite probability for phonon absorption, thus heating the oscillator. The phonons

are absorbed at the rate $\Gamma_q^+ + \Gamma_o^+$. Cooling happens when the emission rate is faster than the absorption rate, which is generally the case in the red-detuning. The dynamic at the red-detuning is schematically shown in Fig. 3.1(b). The steady-state phonon number of the mechanical oscillator is given by

$$\langle \hat{n}_m \rangle_{ss} = \frac{\gamma\, n_{th} + \Gamma_o^+ + \Gamma_q^+}{\gamma + \Gamma_o + \Gamma_q} \tag{3.23}$$

It is clear from Eq. (3.23) that cooling is prominent when the cooling rates Γ_q and Γ_o are maximum, and the heating rates Γ_q^+ and Γ_o^+ are minimum. The quantum limit of bare qubit cooling is given by

$$\langle \hat{n}_m \rangle_q = \Gamma_q^+ / \Gamma_q. \tag{3.24}$$

The minimum value of this quantum limit turns out to be zero at drive strength $\Omega_R = 0$. However, with no drive, the qubit is neither heating nor cooling the oscillator since the spectral noise density responsible for these processes is zero for all frequencies. In the following, we find the minimum quantum limit in the presence of drive. Using Eq. (3.22) and Eq. (3.16), we derive the decay rate Γ_q for $\Gamma \gg \Gamma_d$ and $\bar{\Delta}_q = \Omega$.

$$\Gamma_q = \beta f\left(\Omega_R/\bar{\Delta}_q\right), \tag{3.25}$$

where $\beta = 2G^2/\Gamma$, $\bar{\Delta}_q = \sqrt{\Omega_R^2 + \Delta_c^2}$, and

$$f\left(\Omega_R/\bar{\Delta}_q\right) = 4\frac{\left(\Omega_R/\bar{\Delta}_q\right)^2\sqrt{1-\left(\Omega_R/\bar{\Delta}_q\right)^2}}{4-\left(\Omega_R/\bar{\Delta}_q\right)^4}. \tag{3.26}$$

The maximum cooling rate is achieved for a large value of β and the value of Ω_R which maximize the function $f(\Omega_R/\bar{\Delta}_c)$, i,e., $\Omega_R = 0.85\,\Omega$. At the optimal drive strength, $\Omega_R = 0.85\,\Omega$, the detuning is not absolute, i.e., $\Delta_q = -0.53\,\Omega$. The spectral noise density $Re\{S(\omega)\}$ at the optimal drive is plotted in Fig. 3.2(a). The minimum quantum limit for the optimal drive strength is $\langle \hat{n}_m \rangle_{q,min} = 0.106$. The optomechanical cooling rate Γ_o is given by

$$\Gamma_o = |G_0|^2\left\{\frac{\kappa}{(\Omega+\Delta_c)^2+\kappa^2/4} - \frac{\kappa}{(-\Omega+\Delta_c)^2+\kappa^2/4}\right\} \tag{3.27}$$

The quantum limit of cooling induced by the optical cavity field is given by

$$\langle \hat{n}_m \rangle_o = \Gamma_o^+ / \Gamma_o \tag{3.28}$$

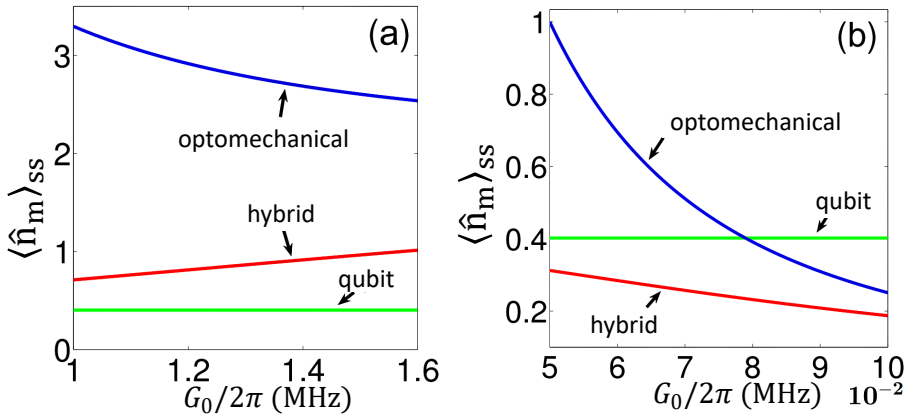

Figure 3.3: (a) Steady-state mean phonon number in the unresolved sideband regime, with $\kappa = 10\,\Omega$ and $\Delta_c = -\kappa/2$. The red, green, and blue curves represent hybrid, qubit, and optomechanical cooling, respectively. Ground state cooling is achievable, but it comes at the cost of bare qubit cooling.(b) Cooling in the resolved sideband regime, where $\kappa = 0.1\,\Omega$ and $\Delta_c = -\Omega$. The hybrid case demonstrates more effective cooling. Other parameters include $\Omega = 10\,\text{MHz}$, $G = 0.2\,\text{MHz}$, $\gamma = 10^{-5}\,\text{MHz}$, and $n_{th} = 10^3$.

Using Eq. (3.19) and Eq. (3.22), we have

$$\langle \hat{n}_m \rangle_o = -\frac{4(\Omega + \Delta_c)^2 + \kappa^2}{16\,\Omega\,\Delta_c}. \tag{3.29}$$

The mininmum cooling limit $\langle \hat{n}_m \rangle_{o,min}$ is reached at a detuning $\Delta_c = -\sqrt{\Omega^2 + \kappa^2/4}$.

$$\langle \hat{n}_m \rangle_{o,min} = \frac{1}{2}\left(\sqrt{1 + \left(\frac{\kappa}{2\Omega}\right)^2} - 1\right) \tag{3.30}$$

For slow oscillators, referred to as unresolved sideband regime, $\Omega \ll \kappa$, the minimum cooling limit is $\langle \hat{n}_m \rangle_{o,min} = \kappa/(4\Omega)$ for $\Delta_c = -\kappa/2$. Ground-state cooling is not possible in this regime. The minimum cooling for fast oscillators, or resolved sideband regime, $\Omega \ll \kappa$, is $\langle \hat{n}_m \rangle_{o,min} = \kappa^2/(4\Omega)^2$ for $\Delta_c = -\Omega$. Thus, ground-state cooling is possible for the high-frequency oscillator. The corresponding spectral noise density $S_{\text{FF}}(\omega)$ for the minimum cooling limit is shown in Fig. 3.2(b). The effective minimum cooling, $\langle \hat{n}_m \rangle_{ss}$ [Eq. (3.23)],

for different optomechanical coupling rates G_0 and the qubit coupling rate $G = 0.2\,\text{MHz}$ is shown in Fig. 3.3(a) and 3.3(b).

3.3.2 Strong Coupling

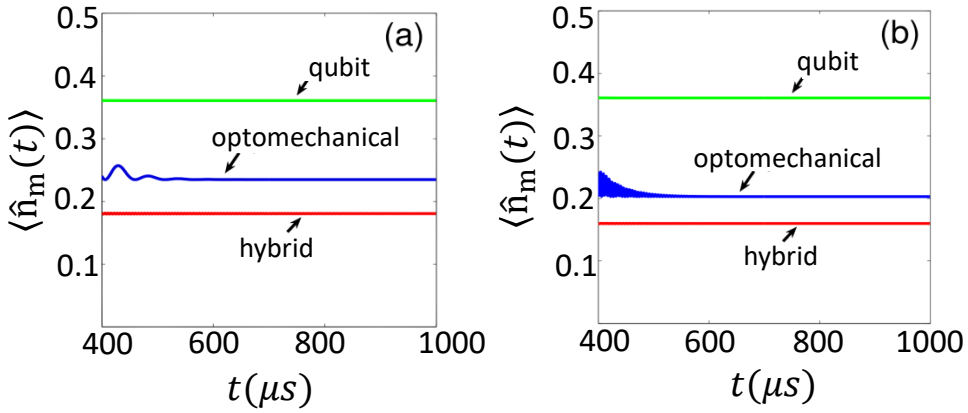

Figure 3.4: (a) Time evolution of the mean phonon number $\langle \hat{n}_m \rangle(t)$ for $G_o = 0.06\,\text{MHz}$, $\kappa = 0.05\,\text{MHz}$, and $G = 0.2\,\text{MHz}$.(b) The mean phonon number $\langle \hat{n}_m \rangle(t)$ for $G_o = 0.6\,\text{MHz}$, $\kappa = 0.05\,\text{MHz}$, and $G = 0.2\,\text{MHz}$.Other parameters include $\Omega = 10\,\text{MHz}$, $\gamma = 10^{-5}\,\text{MHz}$, and $n_{th} = 10^3$.

The strong coupling here refers to the coupling between the optical cavity field and the mechanical oscillator. We will assume that the qubit state is hardly affected by the mechanical interaction and goes to steady-state quickly, and hence adiabatically eliminate from the dynamics of the hybrid system. The reduced master equation of the resultant optomechanical system is given by Eq. (3.14). For determining the steady-state phonon occupation number, we have to solve a linear system of differential equations involving all the the second-order moments: $\partial_t\langle \hat{a}^\dagger \hat{a} \rangle$, $\partial_t\langle \hat{b}^\dagger \hat{b} \rangle$, $\partial_t\langle \hat{a}^\dagger \hat{b} \rangle$, $\partial_t\langle \hat{a} \hat{b} \rangle$, $\partial_t\langle \hat{a}^2 \rangle$, and $\partial_t\langle \hat{b}^2 \rangle$ [158]. Time evolution of the mean phonon number for two coupling cases, $G_o = 1.2\,\kappa$ and $G_o = 12\,\kappa$, are shown in Fig. 3.4. The thermal and initial phonon numbers are assumed to be 10^3. Initial values of all the other moments are kept at zero.

3.4 Conclusion

In conclusion, we have studied the cooling of a mechanical oscillator in a hybrid electro-optomechanical system. We systematically derived the dynamics of the hybrid system and discussed the cooling effects in two specific regimes: weak and strong coupling. In the weak coupling regime, the dynamics of the qubit and the optical cavity field are adiabatically eliminated, leading to an additional factor in the steady-state displacement of the resonator. We also examined the quantum limit of cooling for both individual qubit and optomechanical cooling under this regime. We found that in the weak coupling and resolved sideband regime, cooling is more efficient in the hybrid case for a specific choice of parameters. In the unresolved sideband regime, ground-state cooling remains achievable, but it comes at the expense of qubit cooling. Additionally, we explored cooling in the strong optomechanical coupling case and observed that cooling remains effective in the hybrid configuration.

4

Synchronization of Qubit and Optical Field

In this chapter, we study the synchronization of a superconducting qubit to an external optical field in a hybrid electro-optomechanical system using quantum trajectory method. In a single quantum trajectory run, bistability of the qubit is observed, with the qubit exhibiting rotation in the bistable states. The rotation in one of the stable states is synchronized with the external optical drive. As the number of trajectories is significantly increased, the qubit no longer displays bistability. However, synchronization persists with reduced quantum fluctuations. The scheme proposed here could be used to prepare and monitor the state of the microwave qubit using long-lived optical photons through synchronization, which may find applications in long-distance quantum communication. Additionally, this hybrid system can be utilized to study quantum synchronization.

Information transfer between microwave systems, such as superconducting qubits, and optical signals is essential for realizing long-distance quantum communication. One advantage of encoding information in optical photons is their ability to retain quantum properties even at room temperature, facilitating long-distance quantum state transfer. Naturally, encoding the qubit state in an optical photon paves the way for building efficient quantum

An article based on this chapter is published in Phys. Rev. A **107**, 013528 (2023), titled "*Synchronization of a superconducting qubit to an optical field mediated by a mechanical resonator*" and authored by Roson Nongthombam, Sampreet Kalita, and Amarendra K. Sarma.(©2023 American Physical Society). The contents in this chapter are used with permission.

networks. In this work, we present a scheme in which a long-lived optical signal can be used to prepare, control, and monitor superconducting qubit states through synchronization—the natural tendency of oscillators to adjust their rhythms sympathetically [159]. This approach may have significant applications in long-distance quantum communication. Classical synchronization [160] has garnered considerable interest across various quantum systems [161–167]. Previous studies have explored the synchronization of superconducting qubits with driven microwave cavities [168] and mechanical oscillators with external drives in optomechanical systems [169].

Here, we investigate synchronization in a hybrid system comprising a microwave circuit with a superconducting qubit mechanically coupled to a driven optomechanical cavity. In a single quantum trajectory run, we observe bistability in one of the qubit's polarization vectors, where the qubit rotates around this polarization vector. Through the coupling between the qubit-mechanical system and the mechanical-optical cavity, the phase of the qubit's rotation in one stable state synchronizes with the phase of the reference laser. We further analyze the dynamics of our system across a larger number of quantum trajectories and observe a similar synchronization pattern, albeit with reduced fluctuations. However, in this scenario, bistability in the qubit state is no longer observed.

4.1 System Model and Brief Analysis

We consider a hybrid electro-optomechanical system as shown in the Fig 4.1. whose Hamiltonian is given by

$$\begin{aligned}\hat{H}_{qm} = &-\frac{E_J}{2}\sigma_x + g_q\left(\hat{b}^\dagger + \hat{b}\right)\sigma_z + \omega_m \hat{b}^\dagger\hat{b}, \\ &- \Delta\hat{a}^\dagger\hat{a} - g_o\hat{a}^\dagger\hat{a}\left(\hat{b}^\dagger + \hat{b}\right) + iA_{lp}\left(\hat{a}^\dagger - \hat{a}\right).\end{aligned} \tag{4.1}$$

Here, $\hat{a}$ ($\hat{a}^\dagger$) and $\hat{b}$ ($\hat{b}^\dagger$) are the annihilation (creation) operators of the optical photons inside the cavity and the phonons of the mechanical oscillator, respectively. The first term represents the qubit state with Josephson energy E_J; the second term accounts for the qubit-phonon interaction with coupling strength g_q; the third term describes the energy of the mechanical mode oscillating at frequency ω_m. The fourth and the final terms of Eq. (4.1) denote the energies of the optical cavity and the driving laser, where $\Delta = \omega_{lp} - \omega_c$ is

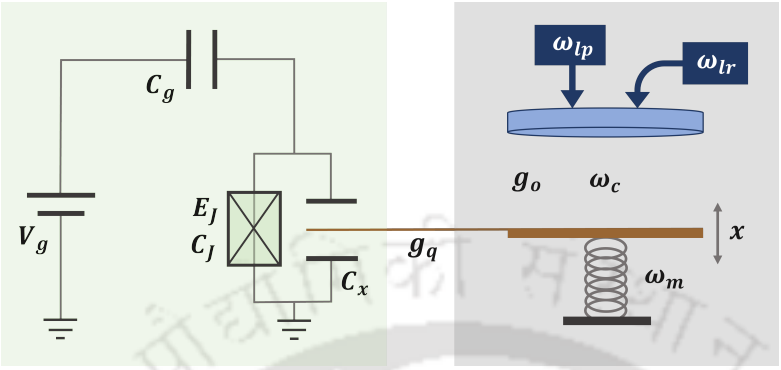

Figure 4.1: Schematics of a mechanically-mediated EOM system with a superconducting qubit (left) and an optomechanical cavity (right). The qubit is capacitively coupled to a mechanical oscillator, which acts as an end-mirror of an optical cavity.

the detuning of the laser frequency ω_{lp} from the cavity resonance frequency ω_c, and A_{lp} is the laser amplitude. The optomechanical interaction of strength g_o between the optical cavity and mechanical resonator is given by the fifth term. In addition to the primary laser drive (A_{lp}, ω_{lp}), we add a reference drive (A_{lr}, ω_{lr}). The corresponding Hamiltonian (in units of $\hbar$) in the rotating frame of the primary laser drive is given by

$$\hat{H}_{lr} = iA_{lr}\left(\hat{a}^{\dagger}e^{-i\Omega t} - \hat{a}e^{i\Omega t}\right), \tag{4.2}$$

where $\Omega = \omega_{lr} - \omega_{lp}$ is the detuning of the reference laser. By blue-detuning the primary laser drive ($\Delta = \omega_m$), the mechanical resonator undergoes self-oscillation, which induces a rotation of the qubit's polarization vector on the Bloch sphere. For a single quantum trajectory, we observe that the mechanical resonator oscillates in two closely spaced circular motions in phase space. Each of these rotations corresponds to a circular rotation of the qubit polarization vector. As a result, we see bistability in one of the components of the qubit polarization vector, with each bistability point corresponding to a rotation of the mechanical resonator.

By applying a reference drive, we can synchronize or lock the phases of the qubit rotation with the phase of the reference drive through the mechanical resonator. Since the state of a qubit is determined by the phase of its polarization vector, as illustrated in Fig. 4.2, we can associate each state of the qubit with the phase of the reference drive due to this synchronization.

Therefore, we can infer the state of the superconducting qubit from the optical drive phase. In the following section, we will numerically derive the bistability

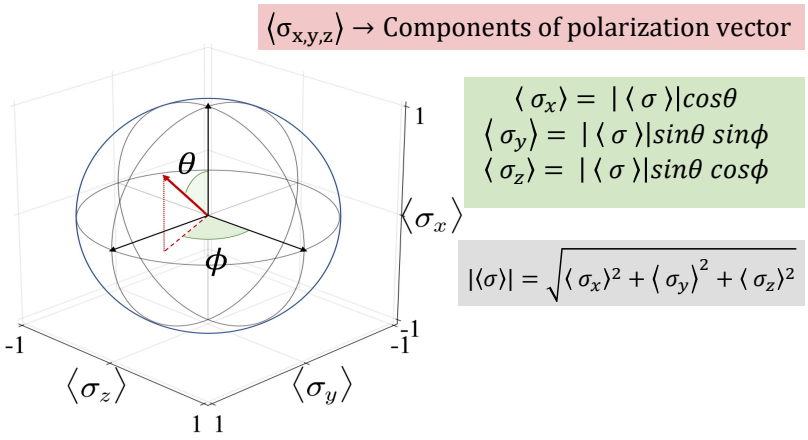

Figure 4.2: Schematic of the Bloch sphere for the qubit. Every point on the sphere represents a state of the qubit. Each point can be determined by knowing the phases (θ, ϕ) of the qubit since $|\langle\sigma\rangle| = \sqrt{\langle\sigma_x\rangle^2 + \langle\sigma_y\rangle^2 + \langle\sigma_z\rangle^2} = 1$.

and synchronization of the qubit in detail.

4.2 Bistability of the Qubit

The system dynamics are numerically evolved using the quantum trajectory method [170–172]. The results are obtained at irrational moments of the optical drive phase Ωt for a single quantum trajectory, with each trajectory evolution corresponding to one experimental run.

The mechanical resonator undergoes self-sustained oscillations due to the blue-detuned laser drive ($\Delta = \omega_m$) of the optomechanical cavity, as shown in Fig. 4.3 (b) and (d). Two self-sustained oscillations of the mechanical resonator are observed, corresponding to which the qubit exhibits bistable behavior—two metastable states of its polarization vector $\langle\sigma_x\rangle$. The other polarization vectors $\langle\sigma_y\rangle$ and $\langle\sigma_z\rangle$ oscillate about the origin. When the qubit is in either of the metastable states, its Bloch vector precesses about the x-axis with $|\langle\sigma\rangle| \approx 1$, as can be seen in Fig. 4.3 (c).

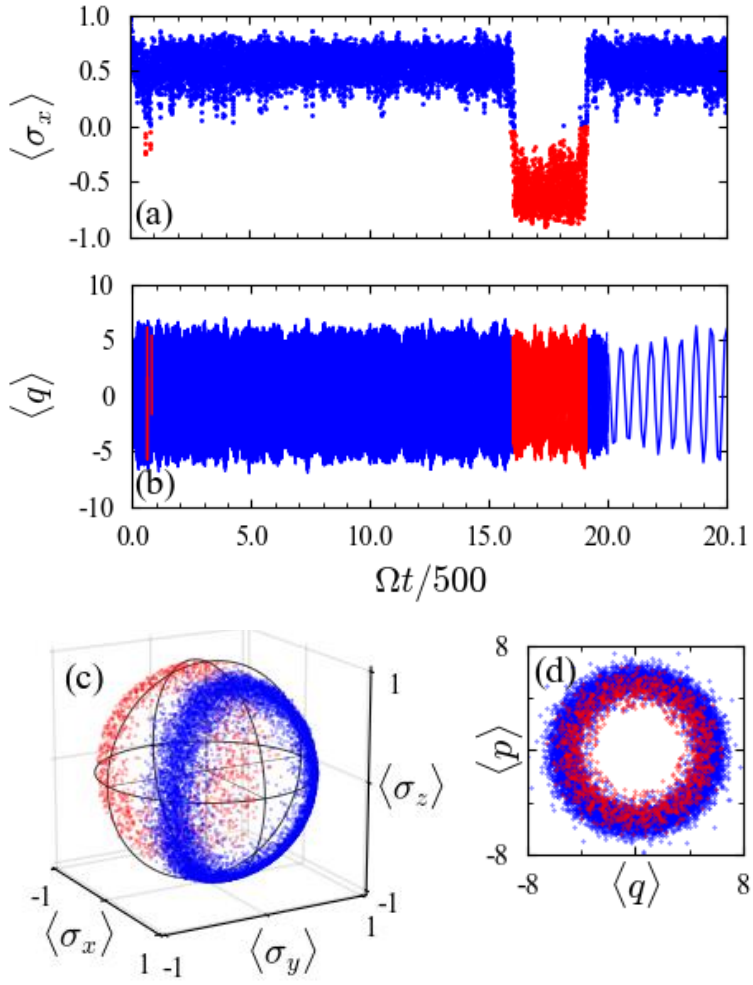

Figure 4.3: (a) Bistability of the qubit along the polarization vector $\langle\sigma_x\rangle$. (b) Fluctuating amplitude oscillation of the mechanical resonator. (c) Bloch sphere representation of the qubit rotation in the two stable states (blue and red states). (d) Overlapping limit cycles of the mechanical oscillator corresponding to the two bistable states of the qubit. The parameters used are $(E_J, g_q, \Delta, g_o, A_{lp}, A_{lr}, \Omega, \kappa, \gamma) = (1.2, 0.04, 1.0, 0.38, 0.6, 0.08, 1.0, 1.4, 0.015) \times \omega_m$.

The occurrence of bistability resembles the process of vacuum Rabi splitting, where a two-level system placed inside a cavity forms a dressed state [168]. In Fig. 4.3, we also observe broad oscillations in the qubit and the

mechanical dynamics. The occurrence of this broadness can be attributed to two reasons. Firstly, the fluctuating radiation pressure force imparted by the external laser via the cavity photons induces fluctuations in the self-sustained motion of the mechanical oscillator. This results in the broadness of the phase-space limit cycles, which in turn, invokes the spreading of the qubit's metastable states via the qubit-mechanical coupling.

When the mechanical oscillator is independently driven without the presence of an optical cavity, depicted by the Hamiltonian $\hat{H} = \hat{H}_{qm} + \hat{H}_m$, we find two well-separated and distinct limit cycles in the mechanical phase space as shown in Fig. 4.4 (a). The metastable states of the qubit polarization vector $\langle \sigma_x \rangle$ are also thinner. Nevertheless, some fluctuation noises still remain due to the quantum jumps from one bistable state to another. Secondly, we have used a single trajectory run to obtain our results in Fig. 4.3.

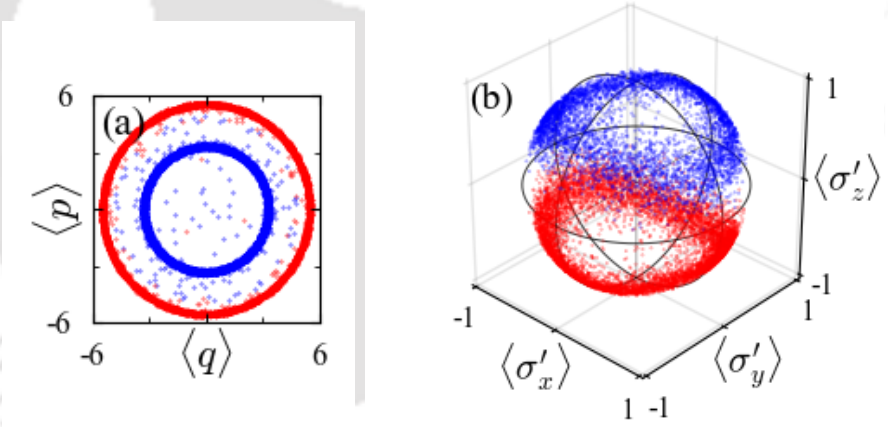

Figure 4.4: (a) Two well-separated and distinct limit cycles of the mechanical oscillator when it is directly driven. In the absence of the optical cavity, the mechanical-qubit system shows less fluctuation. (b) Rotation in the qubit basis. The parameters used are same as those in Fig. 4.3.

As we increase the number of trajectories, we get less scattered and thinner limit cycles. The fluctuations (thickness) of the synchronization phase plot is also reduced. This is for the fact that considering a larger number of trajectories is equivalent to taking the ensemble average of the trajectories which significantly cancels out the fluctuating noises. The effect of a large

number of quantum trajectories in our hybrid system is also discussed in Sec. 4.3. In Fig. 4.4 (b), we plot the Bloch vector in the frame of reference of the qubit, $\hat{H}'_{qm} = \frac{E_J}{2}\sigma'_z + g_q(\hat{b}^\dagger + \hat{b})\sigma'_x$. Here too, we observe bistability along $\langle\sigma'_z\rangle$ and rotation of the qubit about the z-axis.

It is also worth mentioning that even though we are bound by the fluctuating radiation force of the optical photons, we are able to observe quantum synchronization of the qubit with the external optical field within this bound quantum noise. In what follows, we discuss this synchronous behaviour of the qubit rotation phase with the phase of the mechanical oscillation, which in turn, is in sync with that of the reference laser field.

4.3 Synchronization with the External Drive

The synchronization of qubit-mechanical, mechanical-optical and qubit-optical is shown in Figs. 4.5 (a)-(b). We have used the phase relations of the qubit, $\phi = \tan^{-1}(\langle\sigma_y\rangle/\langle\sigma_z\rangle)$, $\theta = \tan^{-1}(\langle\sigma_y\rangle/\{\langle\sigma_x\rangle \sin(\phi)\})$, and that of the mechanical oscillator, $\psi = \tan^{-1}(\langle p\rangle/\langle q\rangle)$. It can be seen that the rotation of the $\langle\sigma_x\rangle > 0$ stable state (blue state) and the rotation of the $\langle\sigma_x\rangle < 0$ stable state (red state) are synced to the corresponding red and blue limit cycles of the mechanical oscillator. Also, we plot the variation in the phase of the qubit rotation and that of the mechanical oscillator with the phase of the reference laser field (mod 2π) in Figs. 4.5 (c)-(f). Here, we observe that the reference drive is synced only to one of the phases of the mechanical oscillator, and subsequently to one of the phases of the qubit rotation. For the same parameters as Fig. 4.3, we observe that the optical drive is synced to the blue stable state of the qubit rotation (Fig. 4.5 (c)) and blue limit cycle of the mechanical oscillator (Fig. 4.5 (d)). This synchronization is found to be more prominent, i.e., having less quantum noise, when the qubit spends more time in the blue state. For every single quantum trajectory run, we get different time span of the bistable states due to the inherent stochastic behaviour of quantum trajectories, and when the time span of blue state is more than the red one, we get a clear synchronization. The corresponding scenario when the drive is not synchronized (red state) is shown in Figs. 4.5 (e)-(f). A similar behaviour of synchronization is observed in the qubit basis. Here, the phase relations change to $\phi = \tan^{-1}(\langle\sigma'_y\rangle/\langle\sigma'_x\rangle)$ and $\theta = tan^{-1}(\langle\sigma'_y\rangle/\{\langle\sigma'_z\rangle \sin(\phi)\})$.

In Fig. 4.6, we show our results for a large number of quantum trajectories. The qubit polarization state $\langle\sigma_x\rangle$ averages out to a near-zero state and the

quantum noise in the synchronization plot is also significantly reduced.

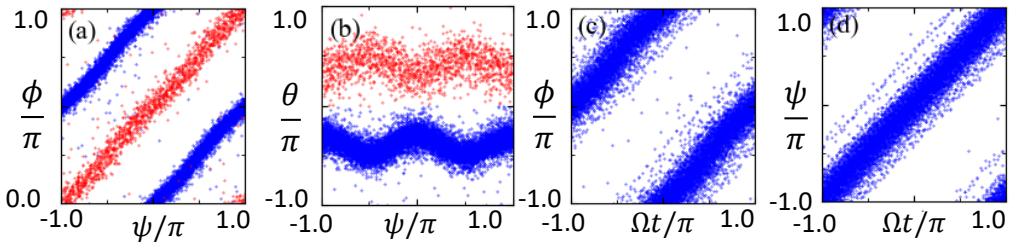

Figure 4.5: Synchronization of the hybrid system. (a) Qubit phase (ϕ) versus mechanical phase (ψ) plot. (b) Qubit phase (θ) versus mechanical phase (ψ) plot. Synchronization of the qubit blue state with the external optical drive is shown in (c). Similarly, phase plot of the mechanical oscillator in the blue limit cycle and the external drive is plotted in (d). (d) Phase of the red limit cycle versus phase of the external drive phase. The parameters used are same as those in Fig. 4.3.

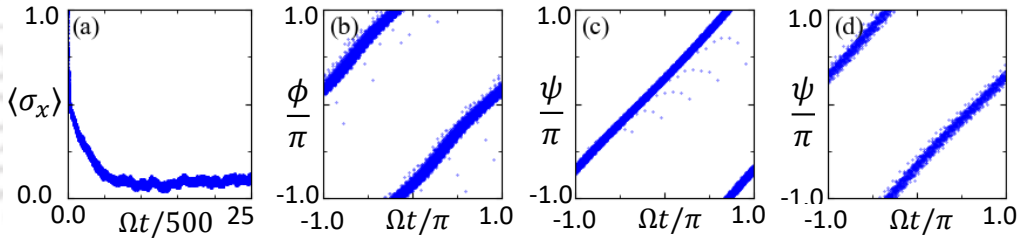

Figure 4.6: Results for a large number of trajectories run. (a) Time evolution of qubit vector $\langle\sigma_x\rangle$. We no longer observe bistability. The qubit vector decays to a near zero state. (b) and (c) shows the less fluctuating synchronization of the qubit and the mechanical oscillator with the reference field, respectively. The parameters used are same as those in Fig. 4.3. (d) Phase plot of the mechanical oscillator and the drive field in a pure optomechanical system. In this case also we observe less fluctuations due to the large number of trajectories.

The amplitude of the qubit rotation decreases and the limit cycle of the mechanical oscillator shrinks towards the origin as the number of trajectories increases. It is also worth mentioning here that although the actual dynamics of the system can follow a very complicated periodic structure, yet at specific intervals of time, simple patterns emerge. Our results also indicate that

at irrational moments of Ωt, a limit-cycle dynamics is observed leading to synchronization between the qubit rotation and the reference drive.

In this work, we observe that a blue-detuned optical drive induces bistability in a qubit, and in one of the bistable states, the qubit rotates in sync with the phase of a reference drive. In addition to this, since the qubit also remains in the pure state, the complete state of the qubit can be monitored and controlled by the laser, as for every phase of the driving field, there exists a corresponding state of the qubit. This scheme can be used to send coherent optical photons from far-off distance, drive the hybrid system, prepare the qubit state and then monitor it. As an important application of this monitoring protocol, the correlation between the states of two distant qubits connected through an optical channel can be explored. A similar idea was theoretically studied in [173] where two qubits are synced and entangled through a driven dissipative microwave resonator. They observe that because of the synchronization, the qubits are maximally entangled. So, by applying the results obtained in our work on the schemes introduced in [37, 174], one can study if synchronization gives rise to maximally entangled qubits placed at distant locations.

4.4 Conclusion

In conclusion, we have numerically demonstrated the synchronization of a superconducting qubit to an external optical field via a mechanical resonator. For a single quantum trajectory, bistability and rotation of the qubit were observed when driven through the optomechanical system. The rotation in one of the bistable states is synchronized with the external optical reference drive, maintaining the purity of the state throughout the process. This setup allows for monitoring and controlling the qubit state via the optical drive, within the fluctuation limits introduced by quantum jumps and the optical drive itself. As the number of trajectories is significantly increased, the qubit no longer exhibits bistability, and while quantum fluctuations decrease, synchronization remains evident.

5

Quantum Transduction of Superconducting Qubit

In this chapter, we investigate the quantum transduction of a superconducting qubit to an optical photon within an electro-optomechanical system. This system consists of a flux-tunable transmon qubit coupled to a suspended mechanical beam, which in turn is coupled to an optical cavity. The transduction process unfolds in a sequence. In the first step, the qubit states are encoded in coherent excitations of phonon modes through a non-demolition qubit interaction. In the second step, we measure the phonon excitations, which reveal the qubit states by counting the average number of photons in the optical cavities.

Quantum transduction is a process that transfers quantum information from one type of quantum system to another, typically involving systems that are very different from each other and do not interact easily. This process often requires an interface that facilitates interaction between different quantum systems. Here, we study quantum transduction that converts quantum information from a superconducting qubit to an optical photon via an intermediate mechanical resonator, allowing the qubit information

An article based on this chapter is published in Phys. Rev. A **108**, 043501 (2023), titled "*Quantum transduction of a superconducting qubit in an electro-optomechanical and an electro-optomagnonical systemr*" and authored by Roson Nongthombam, Pooja Kumari Gupta, and Amarendra K. Sarma.(©2023 American Physical Society). The contents in this chapter are used with permission.

to be transmitted through optical fibers or other communication channels. Achieving high efficient quantum transduction in such settings are essential for realizing long distance quantum communication and modular quantum computers. Recently, much research has been initiated on developing a modular quantum computer based on linking multiple superconducting chips where each chip has a few high-quality qubits. Instead of cramping more qubits onto a single chip, which will result in high error rates and complex hardware, creating a network of modules containing few high-quality qubits on a single chip is better [175–179]. The transduction of the qubit to the optical photon cannot be achieved directly due to the vast separation of the frequencies between the two (qubit in GHz and optical photon in THz). One way to achieve transduction is by introducing a bosonic system as a mediator that couples both the qubit and the optical photon, forming a hybrid qubit-boson-optical system. In this chapter, we discuss transduction in an electro-optomechanical system. In recent years, hybrid electro-optomechanical system has been extensively studied experimentally [47–51, 180–183] and theoretically [107, 184–188] for microwave-to-optical photon transduction. Here, we consider a flux tunable transmon qubit that is coupled to a suspended mechanical beam [97]. The mechanical beam is then integrated as an end mirror of an optomechanical cavity forming the required hybrid system [37].

5.1 System Model and Brief Analysis

The Hamiltonian of the hybrid system considered (Fig 5.1) is given by

$$\begin{aligned}\hat{H}_0 = \; & \hbar\Delta_c\hat{a}^\dagger\hat{a} + \hbar\omega_m\hat{b}^\dagger\hat{b} + \tfrac{\hbar}{2}\omega_t\hat{\sigma}_z + \hbar g_{tm}\hat{\sigma}_z(\hat{b}+\hat{b}^\dagger) \\ & + \hbar g_{om}\hat{a}^\dagger\hat{a}(\hat{b}+\hat{b}^\dagger) + \hbar E_0\left(\hat{a}+\hat{a}^\dagger\right).\end{aligned} \tag{5.1}$$

Here, $\hat{a}(\hat{a}^\dagger)$ and $\hat{b}(\hat{b}^\dagger)$ are the annihilation (creation) operators of the optical photon and the mechanical phonon, respectively. The optomechanical interaction strength, g_{om}, is generally quite small (approximately 1 Hz), so the optomechanical cavity is driven to enhance this coupling strength, as represented by the last term. The Hamiltonian $\hat{H}_0$ is expressed in the optomechanical drive frame, where $\Delta_c = \omega_c - \omega_d$ (with ω_c as the cavity frequency and ω_d as the drive frequency). Although higher-order nonlinear interaction terms are present, as shown in [97], they are excluded here due to their negligible effect on system dynamics. The qubit-mechanical and optomechanical interactions

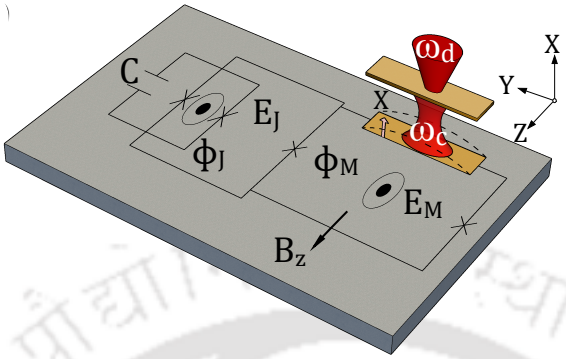

Figure 5.1: Schematic diagram of an electro-optomechanical system. Upon the application of an in-plane magnetic field B_z, the transmon qubit formed by a SQUID loop (E_J, Φ_J) is coupled to a mechanical beam suspended at one arm of the loop (E_M, Φ_M) [**?**]. The mechanical resonator is integrated as a movable plate of an optomechanical cavity with a resonance frequency ω_c. The optomechanical cavity is driven by a red-detuned laser light.

arise from the displacement of the mechanical resonator. When an in-plane magnetic field B_z is applied (see Fig. 5.1), the resonator's displacement induces a flux in the Josephson energy, resulting in the qubit-mechanical interaction [97]. This mechanical motion also alters the resonator frequency of the optomechanical cavity, leading to the optomechanical interaction. We consider small simple harmonic motion (SHM) displacements of the resonator. The transduction of the qubit state occurs in two stages. In the first stage, the focus is on the qubit-mechanical interaction, where the qubit information is coherently encoded into the mechanical resonator while neglecting the optomechanical interaction. This assumption holds because, for an undriven optical cavity ($E_0 = 0$), the optomechanical coupling strength g_{om} is significantly smaller compared to g_{tm}. In the second stage, the qubit-mechanical interaction is turned off using an external flux bias, and the optical cavity is driven ($E_0 \neq 0$), greatly enhancing the optomechanical strength (where $g_{om} \rightarrow \alpha g_{om}$, and α is the boost factor). The mechanical resonator, now containing the encoded qubit information, transfers its state to the optical cavity photons. Consequently, measuring the photon number in the optical cavity allows for decoding the qubit state. A schematic of this transduction sequence is illustrated in Fig. 5.2.

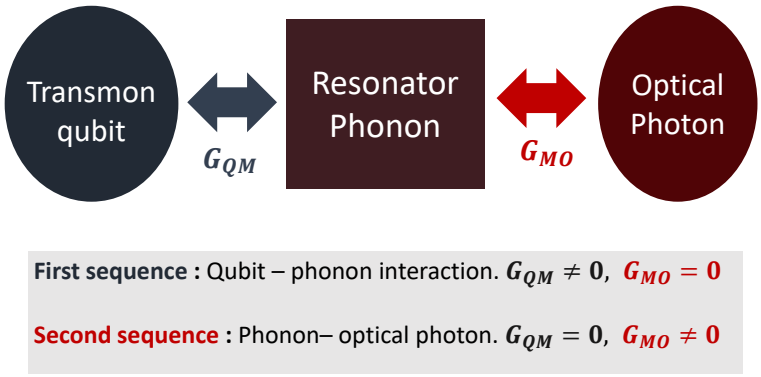

Figure 5.2: Outline of the qubit transduction scheme.

5.2 Encoding the Qubit State into the Mechanical Resonator

In the first stage of the transduction, the qubit state is encoded into the mechanical resonator via the qubit-mechanical interaction. Because the qubit-mechanical coupling rate is much larger than the single-photon optomechanical coupling rate, the optomechanical interaction can be neglected when there is no optomechanical cavity drive. Consequently, only the electromechanical part of the hybrid system remains, which is given by:

$$\hat{H}_{em} = \hbar\omega_m \hat{b}^\dagger \hat{b} + \frac{\hbar}{2}\omega_t \hat{\sigma}_z + \hbar g_{tm} \hat{\sigma}_z (\hat{b} + \hat{b}^\dagger). \tag{5.2}$$

Here, the coupling constant g_{tm} is dependent on the external flux bias Φ_m [97],

$$g_{tm} = g_0 sin(\phi_b), \tag{5.3}$$

where, $\phi_b = \frac{\pi\Phi_m}{\Phi_0}$ and $\Phi_0 = \frac{h}{2e}$ is the flux quantum. g_0 is coupling constant. It is dependent on the transmon impedance, SQUID asymmetry and the applied magnetic field [97]. Next, we enhance the coupling rate by modulating it parametrically by applying a weak ac bias $\phi_b = \phi_{ac} cos(\omega_{ac} t)$ ($\phi_{ac} << 1$) [98].

$$g_{tm} = g_0 \phi_{ac} cos(\omega_{ac} t). \tag{5.4}$$

By substituting this modulated time dependent coupling constant in the Hamiltonian (5.2), and then transforming the resultant Hamiltonian in the

reference frame of the ac drive ($U = e^{i\omega_{ac}tb^\dagger b}$), we get

$$\hat{H}'_{em} = \hbar\omega_m \hat{b}^\dagger\hat{b} + \frac{\hbar}{2}\omega_t\hat{\sigma}_z + \hbar g_0\phi_{ac}\hat{\sigma}_z(\hat{b} + \hat{b}^\dagger) - \omega_{ac}\hat{b}^\dagger\hat{b}. \tag{5.5}$$

Here, fast rotating terms have been ignored since $2\omega_{ac} >> g_0\phi_{ac}$. We evolve the system under resonant modulation ($\omega_m = \omega_{ac}$). If the qubit is initially in the ground state $|g\rangle$ and the mechanical resonator is in the vacuum state $|0_b\rangle$, after some time t, the qubit remains in the ground state, while the mechanical resonator evolves into a coherent state $|\beta_b = ig_0\phi_{ac}t\rangle$. Conversely, if the qubit starts in the excited state $|e\rangle$ and the resonator is initially in the vacuum state, the qubit will remain in the excited state, and the mechanical resonator will evolve into another coherent state with the same amplitude but a different phase $|\beta_b = -ig_0\phi_{ac}t\rangle$ after time t.

$$|g, 0_b\rangle_0 \longrightarrow |g, \beta_b = g_0\phi_{ac}t\rangle_t$$

$$|e, 0_b\rangle_0 \longrightarrow |e, \beta_b = -ig_0\phi_{ac}t\rangle_t$$

An overall phase term induced by the intrinsic qubit Hamiltonian is not included, as it does not contribute to the transduction process. As the system evolves, the mechanical resonator transitions from a vacuum state to a coherent state, while the qubit state remains unchanged. This is due to the fact that the interaction between the qubit and the mechanical resonator commutes with the intrinsic Hamiltonian of the qubit, indicating that the interaction is "non-demolition" for the qubit.

In the presence of a thermal environment, the system evolves according to the Lindblad master equation.

$$\begin{aligned}\dot{\hat{\rho}}_{em} &= -i[\hat{H}_{em}, \hat{\rho}_{em}] + \Gamma\mathcal{L}[\hat{\sigma_z}] + \Gamma\mathcal{L}[\hat{\sigma}^-] \\ &\quad +\gamma_b(n_{th}+1)\mathcal{L}[\hat{b}] + \gamma_b n_{th}\mathcal{L}[\hat{b}^\dagger],\end{aligned} \tag{5.6}$$

where $\mathcal{L}[\hat{o}] = (2\hat{o}\hat{\rho}\hat{o}^\dagger - \hat{o}^\dagger\hat{o}\hat{\rho} - \hat{\rho}\hat{o}^\dagger\hat{o})/2$. Here, Γ is the decoherence and dephasing rate of the transmon qubit , γ_b is the decay rate of phonon, $n_{th}(n'_{th})$ is the thermal phonon number, and $\hat{\rho}_{em}$ is the density operator of the qubit-mechanical system. We have neglected the thermal photons of the optical cavity due to the high frequency of the optical photon. To observe the coherent excitations of mechanical resonator in the dissipating environment, we plot the Wigner functions in Fig 5.3. We observe that the Wigner functions of the

phonon and magnon at some time $\tau = (3/2\pi)\ \mu s$ and for coupling constants $g_0\phi_{ac} = g_0'\phi_{ac}' = 2\pi$ MHz show coherent state profile. The amplitude of the coherent states when the qubit is in the ground state is $|\beta_b = ig_0\phi_{ac}\tau\rangle = |3i\rangle$ for the phonon, as shown in the figure.

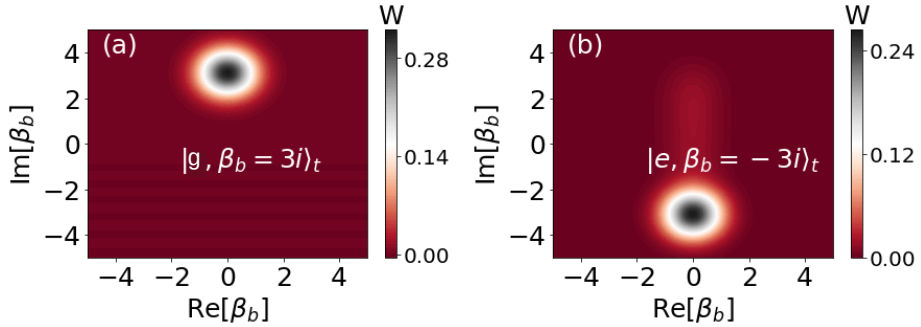

Figure 5.3: Wigner function representation of the coherent states of phonon. (a) The phonon excites to the coherent states $|\beta_b = 3i\rangle_t$ when the qubit is in the ground state $|g\rangle$. The coherent states of the phonon $|\beta_b = -3i\rangle_t$ when the qubit is in the exited state $|e\rangle$ is shown in (b). The coherent states are taken at time $t = \tau = (3/2\pi)\ \mu s$ for coupling constants $g_0\phi_{ac} = 2\pi$ MHz. The other parameters are $\gamma_b/2\pi = 1$ Hz, $n_{th} = 400$, $\Gamma/2\pi = 0.1$ GHz

On the other hand, when the qubit is in the excited state, the coherent amplitudes are $|\beta_b = -ig_0\phi_{ac}\tau\rangle = |3i\rangle$. These changes in the amplitude of the coherent states corresponding to the qubit ground and excited states are similar to the ones that are observed in the non-dissipative case. So, in both the dissipative and non-dissipative qubit-mechanical systems, we observe that the ground state of the qubit is encoded or associated with a coherent excitation of the phonon and the excited state of the qubit is encoded in another coherent excitation of the same phonon having amplitudes exactly opposite to that of the excitation associated with qubit ground state.

5.3 Exchange of Mechanical and Optical States.

In the first stage, the qubit state was encoded into the coherent excitations of a phonon. Now, we will transfer this qubit-encoded state from the mechanical resonator to an optical photon through optomechanical interaction, thereby completing the second stage. From the previous analysis of the electro-

mechanical interaction, it is clear that the mechanical resonator can be coherently excited to different amplitudes depending on the initial state of the qubit. We will first consider the qubit in the excited state, which coherently excites the mechanical resonator to $|\beta_b = \pm i g_0 \phi_{ac} t\rangle$. After this excitation, the interaction $g_0\phi_{ac}$ is switched off by turning off the flux bias ϕ_{ac}. The remaining interacting system is then the optomechanical system.

$$\hat{H} = \hbar\Delta_c \hat{a}^\dagger \hat{a} + \hbar\omega_m \hat{b}^\dagger \hat{b} + \hbar g_{om} \hat{a}^\dagger \hat{a}(\hat{b}^\dagger + \hat{b}) + \hbar E_0(\hat{a}^\dagger + \hat{a}). \tag{5.7}$$

Since $g_{om} \approx 1$Hz is very weak, we drive the cavity with an intense laser. Because of this strong drive, we can separate the amplitudes of the mechanical resonator and optical cavity into a semi-classical coherent part (β, α) and a small quantum fluctuation $(\delta\hat{a}, \delta\hat{b})$ around it, i.e., $\hat{a} \to \delta\hat{a} + \alpha$ and $\hat{b} \to \delta\hat{b} + \beta$. We substitute this separation in Eq.(5.7). At the steady state, the semi-classical coherent parts are given by

$$\alpha = \frac{E_0}{\kappa/2 - i\Delta_c + i(\beta + \beta^*) g_{om}} \tag{5.8a}$$

$$\beta = \frac{i g_{om} |\alpha|^2}{\gamma_b/2 + i\omega_m} \tag{5.8b}$$

By retaining only the interacting term, which is multiplied by the factor $\alpha(|\alpha| \approx 10^3)$, the Hamiltonian 5.7 reads

$$\hat{H}_{om} = \hbar\Delta' \hat{a}^\dagger \hat{a} + \hbar\omega_m \hat{b}^\dagger \hat{b} + \hbar G_{om}(\hat{a}^\dagger + \hat{a})(\hat{b}^\dagger + \hat{b}), \tag{5.9}$$

where $\Delta = \Delta_c - (\beta + \beta^*) g_{om}$ and $G_{om} = g_{om}|\alpha|$ for a constant phase preference of alpha. For simplicity we have rewritten $\delta\hat{a}$ to $\hat{a}$ and $\delta\hat{b}$ to $\hat{b}$. Note that while writing Eq.5.9, we have ignored all the constant terms and all the linear terms containing $\hat{a}$, $\hat{a}^\dagger$, $\hat{b}$ and $\hat{b}^\dagger$ are equated to zero. The coherent state of the mechanical resonator prepared from the electro-mechanical interaction is in the mechanical frame $\omega_m = \omega_{ac}$. So, we transform the Hamiltonian (5.9) in the mechanical frame. We further transform the system in the cavity detuning frame Δ. Therefore, for a red-detuned laser drive $\Delta = \omega_m$, Eq.(5.9) becomes

$$\hat{H}_{om} = \hbar G_{om}(\hat{a}^\dagger \hat{b} + \hat{b}^\dagger \hat{a}). \tag{5.10}$$

Here, the fast rotating terms are ignored provided $G_{om} << 2\omega_m$. For studying the state transfer from mechanical phonon to optical photon, we write down

the dynamics of average number of photon and phonon in the presence of dissipation.

$$\frac{d\langle\hat{a}^\dagger\hat{a}\rangle}{dt} = -i(\langle\hat{a}^\dagger\hat{b}\rangle - \langle\hat{b}^\dagger\hat{a}\rangle)G_{om} - \kappa\langle\hat{a}^\dagger\hat{a}\rangle \tag{5.11a}$$

$$\frac{d\langle\hat{b}^\dagger\hat{b}\rangle}{dt} = -i(\langle\hat{b}^\dagger\hat{a}\rangle - \langle\hat{a}^\dagger\hat{b}\rangle)G_{om} - \gamma_b\langle\hat{b}^\dagger\hat{b}\rangle + \gamma_b n_{th} \tag{5.11b}$$

$$\frac{d\langle\hat{b}^\dagger\hat{a}\rangle}{dt} = \frac{-(\kappa+\gamma_b)}{2}\langle\hat{b}^\dagger\hat{a}\rangle - iG_{om}(\langle\hat{a}^\dagger\hat{a}\rangle - \langle\hat{b}^\dagger\hat{b}\rangle) \tag{5.11c}$$

The analytical solution of Eq. 5.11 in the absence of dissipation is given by

$$\langle\hat{a}^\dagger\hat{a}\rangle = \frac{1}{2}\{|\alpha_0|^2 + |\beta_0|^2 + (|\alpha_0|^2 - |\beta_0|^2)\,cos(2G_{om}t) - i(\alpha_0^*\beta_0 - \alpha_0\beta_0^*)\,sin(2G_{om}t)\} \tag{5.12}$$

Here, $|\alpha_0|^2 = \langle\hat{a}^\dagger\hat{a}\rangle_0$ and $|\beta_0|^2 = \langle\hat{b}^\dagger\hat{b}\rangle_0$ are the initial values of photon and phonon/magnon. The above equation can be further simplified by simply choosing $|\alpha_0|^2 = |\beta_0|^2$.

$$\langle\hat{a}^\dagger\hat{a}\rangle = |\alpha_0|^2 - Im(\alpha_0^*\beta_0)\,sin(2G_{om}t) \tag{5.13}$$

The initial coherent amplitudes of phonon is fixed at $\beta_0 = \pm ig_0\phi_{ac}\tau$. To keep the oscillatory part in Eq. (5.13), which is necessary for the transduction, we require that the initial coherent amplitude of the cavity photon α_0 should have a non-zero real part. Therefore, we choose $\alpha_0 = g_0\phi_{ac}\tau$. The oscillation of Eq. 5.13 then becomes

$$\langle\hat{a}^\dagger\hat{a}\rangle = (g_0\phi_{ac}\tau)^2\{1 - sin(2G_{om}t)\}, \tag{5.14}$$

when the qubit is in the excited state ($\beta_0 = -ig_0\phi_{ac}\tau$), and

$$\langle\hat{a}^\dagger\hat{a}\rangle = (g_0\phi_{ac}\tau)^2\{1 + sin(2G_{om}t)\}, \tag{5.15}$$

when the qubit is in the ground state ($\beta_0 = ig_0\phi_{ac}\tau$). The evolution of the average photon number is depicted in Fig. 5.4(a). The figure illustrates that measuring the average photon number in the cavity at intervals of $t = \pi/2G_{om}$ (starting from $t = \pi/4G_{om}$) allows us to detect the presence or absence of

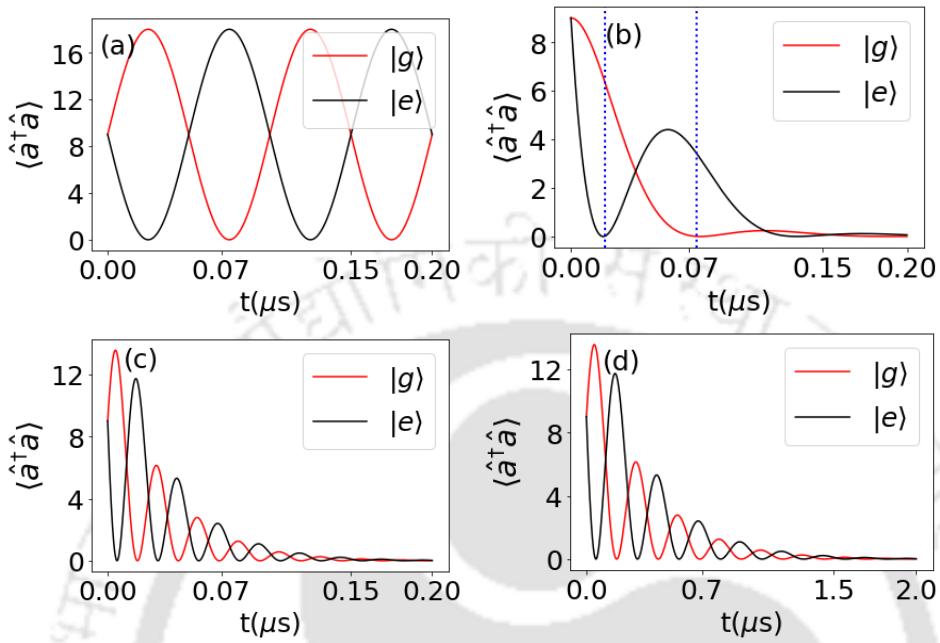

Figure 5.4: Evolution of the average number of photon $\langle \hat{a}^\dagger \hat{a} \rangle$ in the optical cavity. (a) In the absence of dissipation, the oscillatory evolution of $\langle \hat{a}^\dagger \hat{a} \rangle$ keeps on going. When the qubit is in the ground state, the oscillation is represented by the red colour, and when the qubit is in the ground state, the oscillation is represented by the black colour. The evolution of average photon number in the presence of dissipation is shown in (b) for $\kappa = 2G_{om}$, (c) and (d) for $\kappa = G_{om}$. In (a), (b), and (c), $\kappa/2\pi = 0.01$ GHz is used, and in (d), $\kappa/2\pi = 1$ MHz is used. The other common parameters are $\gamma = 1$ Hz and $n_{th} = 400$.

photons, depending on the state of the qubit. If photons are detected in the cavity at intervals of $t = (2n+1)\pi/4G_{om}$, where $n = 0, 2, 4, \ldots$, it indicates that the qubit is in the ground state. Conversely, if no photons are detected at the same intervals, the qubit is in the excited state. Similarly, if photons are detected at intervals of $t = (2n+1)\pi/4G_{om}$, where $n = 1, 3, 5, \ldots$, it indicates that the qubit is in the excited state, while the absence of photons at these intervals suggests the qubit is in the ground state. These specific intervals were chosen because the average photon numbers at these times are maximally separated, making it easier to determine the qubit states more accurately than at other intervals.

In the presence of dissipation, the oscillatory nature of $\langle \hat{a}^\dagger \hat{a} \rangle$(t) decays

over time. To accurately determine the state of the qubit by counting the photon number, the optomechanical coupling rate G_{om} should be comparable to the cavity decay rate κ. Figure 5.4(b) illustrates the decay of the cavity photon number for $\kappa = 2G_{om}$, representing a moderate coupling strength. At this strength, efficient qubit state measurements can be performed at just two intervals, $t = 0.02\,\mu s$ and $t = 0.075\,\mu s$, before the average photon number decays to zero. If the coupling strength is lower than this, identifying the qubit states from the optical photons becomes unfeasible. Figure 5.4(c) depicts the scenario where the coupling strength equals the decay rate. Here, more oscillations are visible, allowing for additional time intervals to measure the qubit states. Furthermore, as shown in Figure 5.4(d), reducing the decay rate κ enables an increase in the time period for the same number of oscillations.

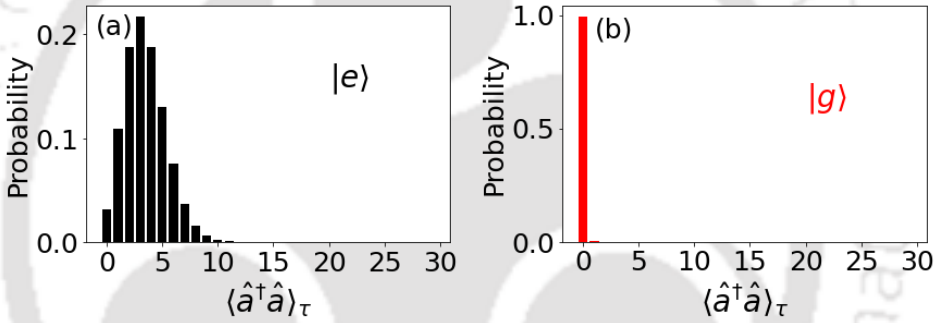

Figure 5.5: Probability distribution of coherent states of the optical photon number in the presence of dissipation. (a) and (b) shows the distribution when the qubit is in the ground and excited state, respectively. The coherent states are measured at time $\tau = 0.075$ μs. The average photon number in (a) is 3.4, and 0 in (b).

Since we are dealing with coherent states, it is possible to quantify how well the measured photon number indicates the qubit's particular state. In Fig. 5.5, we plot the probability distribution of the coherent state for the case of $\kappa = 2G_{om}$ (refer to Fig. 5.4(b)) at the measurement time $\tau = 0.075\,\mu s$. It is evident that even when the qubit is in the excited state, there remains some probability of not detecting any photons in the cavity. The difference in the probability of not finding photons when the qubit is in the excited state ($P_e = 0.035$) compared to the ground state ($P_g = 0.999$) provides the efficiency for determining the qubit state, given by $P = P_e - P_g = 0.964$. This efficiency tends to decrease with a lower average photon number and vice versa. Therefore, it is necessary to repeat the counting measurement several

times to reliably conclude the nature of the qubit state.

5.4 Conclusion

In conclusion, a scheme has been proposed to achieve quantum transduction of a superconducting flux-tunable transmon qubit within a hybrid electro-optomechanical system. The transduction process occurs in two stages. First, the qubit states are encoded into the coherent excitations of mechanical phonons without disturbing the qubit state, ensuring a non-demolition interaction. In the second stage, these excitations are identified by counting the average number of photons in the optomechanical cavity. The coherent interaction between the phonon and the optical photon results in oscillations of the average photon number over time. These oscillation patterns are exactly opposite when the qubit is in the ground state compared to when it is in the excited state. Consequently, multiple measurements of the photon number can be conducted at regular intervals, enabling the determination of the qubit's state at each time point. In the presence of dissipation, it is essential for the optomechanical coupling strength to be at least moderately strong to allow for measurements before the photon number decays to zero. The required coupling strength in the optomechanical system has been analyzed. Realizing quantum transduction in hybrid systems, such as the one studied here, is crucial for developing long-distance quantum communication and advancing quantum networks.

6 Conclusion

Hybrid systems implemented in circuit QED demonstrated significant potential for quantum technological applications, thanks to their design flexibility, advanced fabrication techniques, and strong coupling capabilities derived from the large zero-point field of superconducting circuits. In this thesis, we explored various quantum applications within two hybrid systems based on the circuit QED platform: electromechanical and electro-optomechanical systems. The introductory chapter provided an overview of how these systems were integrated on a superconducting chip. We outlined the fundamental concepts behind these hybrid systems and categorized them based on the interactions among their components. For example, in an electromechanical hybrid system, a suspended mechanical resonator coupled with the qubit via a movable capacitor or through flux induced in the qubit loop. Additionally, the qubit could couple with phononic crystal modes through the piezoelectric response. By introducing an optical mode, either via a Fabry-Pérot cavity or an optomechanical crystal, the electromechanical system evolved into an electro-optomechanical system. The subsequent chapters delved into various quantum phenomena and their applications within these two hybrid systems.

In Chapter 2, we considered two phononic crystal resonators coupled to two superconducting qubits separately through the piezoelectric response of the crystals. We first entangled the qubit-mechanical pairs by dispersively driving the qubits from the resonators and then performed a Bell state measurement on the qubits. This measurement induced entanglement, resulting in bipartite cat states of the two resonators, even though they did not initially interact. We showed that, based on the measurement outcome of the Bell test, four

bipartite cat states could be produced. Since the two qubits involved in the Bell test were linked through a microwave cavity, they could be placed far apart, enabling the remote generation of these cat states. Additionally, we performed a Bell inequality test using the CHSH formalism, which revealed a violation of the inequality. We also analyzed how the level of violation depended on coupling strength and decay rates.

In Chapter 3, we demonstrated the cooling of a suspended MHz frequency nanomechanical resonator in a hybrid electro-optomechanical system, which was realized by introducing a Fabry-Pérot cavity into an electromechanical system. The cooling of the resonator occurred by applying a red-detuned drive to both the qubit and the optical cavity. Due to the red detuning, the qubit was excited to a higher energy level by absorbing incoming photons from the external drive, as well as phonons from the mechanical oscillator. Consequently, the mechanical resonator lost phonons to the qubit, resulting in its cooling. Similarly, optical photons entered the cavity by absorbing a phonon from the oscillator, also due to the red-detuned drive, which further cooled the resonator. These two processes happened simultaneously, allowing us to achieve ground state cooling of the mechanical resonator within the hybrid electro-optomechanical system. We also compared the individual cooling methods, namely qubit-mechanical and mechanical-cavity cooling, with the hybrid cooling. In the weak coupling regime, hybrid cooling was shown to be more efficient than the individual systems within the resolved sideband resonator. Likewise, in the strong coupling regime, hybrid cooling also demonstrated greater effectiveness.

Using the same hybrid system employed for cooling, we investigated the synchronization of a superconducting qubit with an external optical drive in Chapter 4. The synchronization was studied under quantum trajectory evolution. In a single trajectory run, we observed that an optical blue-detuned drive induced two self-sustained oscillations in the resonator and two stable states of the qubit defined by its polarization vectors. The bistable states of the qubit appeared as two rotations about the stable vector on the Bloch sphere, with the phase of this rotation synchronized to the phase of the resonator's oscillation. By applying a reference drive to the optical cavity, we demonstrated that the phase of the qubit's rotation could be locked to the phase of the reference drive. We repeated these observations across a large number of trajectories and found that while the bistabilities vanished, the synchronization persisted.

In Chapter 5, we proposed a scheme to transduce qubit information to an

optical mode using an electro-optomechanical system, where the resonator is coupled to the qubit by modifying the qubit's flux loop. The transduction of the qubit state occurs in two stages. In the first stage, we focused solely on the qubit-mechanical interaction, coherently encoding the qubit information into the mechanical resonator. In the second stage, we disabled the qubit-mechanical interaction using an external flux bias and activated the optomechanical coupling by driving the optical cavity. The state of the mechanical resonator, which contains the encoded qubit information, was then swapped to the optical cavity photons. Thus, by measuring the state of the optical cavity photons, we were able to decode the state of the qubit.

While the quantum phenomena and applications such as the cooling of a resonator, synchronization of the qubit, and bipartite cat state generation were studied within a specific hybrid system, these investigations can also be extended to other hybrid systems. For instance, the generation of bipartite cat states could be expanded to two electro-optomechanical systems connected through the same optical channel, where the two qubits would be linked by long-lived photons. This arrangement could enhance long-distance quantum communication based on continuous variable phononic resonators. Additionally, synchronization and cooling phenomena could be explored within electromechanical systems by replacing the optical cavity with a microwave cavity. An advantage of confining the system to the circuit itself is the reduction of added noise, as well as the mitigation of large frequency differences between components, which is essential for achieving stronger coupling.Moreover, the hybrid systems studied in this thesis are frequently utilized for various technological applications, including practical long-distance quantum communication, the development of quantum networks using repeaters, and the realization of modular quantum computers. The primary challenges in all these applications involve managing the loss of quantum information due to decoherence from environmental noise. Extensive research is ongoing to mitigate the effects of noise and to achieve practical quantum technological applications.

A

Appendix

A.1 Derivation of Hamiltonian (3.3)

The qubit part of Eq. (3.2) in the number basis can be written as

$$\begin{aligned} H_q =& 4E_c(x) \sum_N \left[\hat{N} - N_{xq}(x)\right]^2 |N\rangle \langle N| \\ & - \frac{E_J}{2} \sum_N \left(|N+1\rangle \langle N| + |N\rangle \langle N+1|\right) \end{aligned} \tag{A.1}$$

where $E_c(x) = e^2/2C_\Sigma(x)$ is the charging energy of the CPB. Substituting the value of $N_{xq}(x)$, which is close to an odd number of electron charges, in Eq.(2.2), and restricting $|N\rangle$ to $|0\rangle$ and $|1\rangle$, we get the *two-level approximation* Hamiltonian,

$$\begin{aligned} H_q =& - E_c(x) \left[1 + 4\Delta N(x)^2\right] I \\ & + 4E_c(x)\Delta N(x)\sigma'_z - \frac{E_J}{2}\sigma'_x \end{aligned} \tag{A.2}$$

Here, all the states are eigenstates of the I operator, so the first term just add extra energy of $E_c(x)(1 + 4\Delta^2)$ to all the states. We can therefore omit this term.

$$H_q = -4E_c(x)\Delta N(x)\sigma'_z - \frac{E_J}{2}\sigma'_x \tag{A.3}$$

Assuming that the displacement x of the movable capacitor is relatively small compared to it's initial separation d, we approximate $C_x(x) \approx C_x - C_x(x/d)$, and hence $\Delta N(x) \approx \Delta N - N_x(x/d)$ and $E_c(x) \approx E_c + E_c(C_x/C_\Sigma)(x/d)$. Here, $C_x = 2eN_x/V_x$, $E_c = e^2/2C_\Sigma$ and $C_\Sigma = 2C_J + C_q + C_x$. Substituting in Eq. (A.3), we get

$$\hat{H}_q = -\frac{\epsilon}{2}\sigma'_z - \frac{E_J}{2}\sigma'_x - \hbar g\left(\hat{b}^\dagger + \hat{b}\right)\sigma'_z, \tag{A.4}$$

where $g = (4E_cX_{\rm ZPF}/\hbar d)[N_x - \Delta N(C_x/C_\Sigma)]$, $\epsilon = 8E_c\Delta N$ and $X_{\rm ZPF}$ is the zero-point field amplitude of the oscillator. For a large value of $N_x \gg 1$, the coupling rate can be approximated to $g \approx 4E_cX_{\rm ZPF}/(\hbar dN_x)$. Both the gate voltage V_q and V_x have quantum fluctuations ($\delta\hat{N}_x$ and $\delta\hat{N}_q$) which acts as a quantum dissipation to both the qubit and oscillator. This fluctuation is visible in ΔN, i.e., $\Delta N \to \Delta N + \delta\hat{N}_x + \delta\hat{N}_q$. Substituting these fluctuations in Eq.(2.5), and in the first term of Eq.(2.3), we obtain two additional terms, i.e., $4E_c(\delta\hat{N}_x+\delta\hat{N}_q)\sigma'_z$ and $4E_cX_{\rm ZPF}(\delta\hat{N}_x+\delta\hat{N}_q)(\hat{b}^\dagger+\hat{b})$. The first term causes dephasing of the qubit and the second term causes relaxation of the oscillator. These fluctuations can be included in the Lindblad master equation of the total hybrid system as a decay rates, and hence, can be omitted from the Hamiltonian. If we coherently drive the qubit at frequency ω_d and amplitude Ω_R, the qubit Hamiltonian with the driving term reads

$$\hat{H}_q = -\frac{\epsilon}{2}\sigma'_z - \frac{E_J}{2}\sigma'_x - \hbar g(\hat{b}^\dagger + \hat{b})\sigma'_z + \hbar\Omega_R\cos(\omega_d t)\sigma'_z. \tag{A.5}$$

After transforming to the eigenbasis of the qubit, the Hamiltonian H_q reads

$$\begin{aligned}\hat{H}_q =& \frac{\hbar\omega_q}{2}\sigma_z + \hbar\Omega_R\cos(\omega_d t)(\sigma_x\cos\varphi - \sigma_z\sin\varphi)\\ &- \hbar g(\hat{b}^\dagger + \hat{b})(\sigma_x\cos\varphi - \sigma_z\sin\varphi),\end{aligned} \tag{A.6}$$

where $\tan\varphi = \epsilon/E_J$ and $\hbar\omega_q = \sqrt{\epsilon^2 + E_J^2}$. Within the usual RWA approximation, the transverse coupling term $\hbar g(\hat{b}^\dagger + \hat{b})\sigma_x\cos\varphi$ can be dropped due to the significant difference in qubit and oscillator energy scales, i.e., $\omega_q \gg \Omega$. Near the charge symmetry point ($\Delta N \approx 0$ and $\sin\varphi \approx 0$), the longitudinal coupling is weak. So, we transform the transverse coupling term using Schrieffer-Wolff transformation [152] and retain the second-order coupling term $\hbar(g^2/\omega_q)\cos^2\varphi(\hat{b}^\dagger + \hat{b})^2\sigma_z$. Furthermore, due to $\omega_d \approx \omega_q$, we can drop

the driving term $\hbar\Omega_R \cos(\omega_d t)\sigma_z \sin\varphi$ under RWA. The Hamiltonian then simplifies to

$$\begin{aligned}\hat{H}_q =& \frac{\hbar\omega_q}{2}\sigma_z + \hbar\Omega_R \cos(\omega_d t)\sigma_x \cos\varphi \\ &+ \hbar g(\hat{b}^\dagger + \hat{b})\sigma_z \sin\varphi + \hbar\frac{g^2}{\omega_q}\cos^2\varphi(\hat{b}^\dagger + \hat{b})^2\sigma_z. \end{aligned} \tag{A.7}$$

In the drive frame (ω_d) of the qubit, we have

$$\begin{aligned}\hat{H}_q =& -\frac{\hbar\Delta_q}{2}\sigma_z + \frac{1}{2}\hbar\Omega_R\sigma_x \cos\varphi \\ &+ \hbar g(\hat{b}^\dagger + \hat{b})\sigma_z \sin\varphi + \hbar\frac{g^2}{\omega_q}\cos^2\varphi(\hat{b}^\dagger + \hat{b})^2\sigma_z, \end{aligned} \tag{A.8}$$

with $\Delta_q = \omega_d - \omega_q$. On expanding the last term, we get terms that are proportional to $\hat{a}\hat{a}^\dagger$, $\hat{a}^\dagger\hat{a}$, $\hat{a}^\dagger\hat{a}^\dagger$ and $\hat{a}\hat{a}$. By neglecting the two phonon interaction terms $\hat{a}\hat{a}$ and $\hat{a}^\dagger\hat{a}^\dagger$ under RWA we get the qubit part in Eq. (3.3)

A.2 Generation of Qubit Bell state

The interaction between the two qubits that generates the Bell state is given by

$$\hat{H} = \hbar J'(\hat{\sigma}_1^+\hat{\sigma}_2^- + \hat{\sigma}_2^+\hat{\sigma}_1^-). \tag{A.9}$$

This interaction is a by product of the dispersive transformation and the cavity photon connects the two qubit virtually. In order to distinguish all the Bell states of the two qubit, we resonantly drive the qubits individually.

$$\hat{H} = \hbar(J'\hat{\sigma}_1^+\hat{\sigma}_2^- + \sum_{j=1,2} A_j e^{-i\Phi_j}\sigma_j^+) + H.c. \tag{A.10}$$

Here, A_j and Φ_j are the Rabi frequency and phase, respectively, of the drive applied to the qubits. We have assumed that $J' >> \lambda_1, \lambda_2$. The drive produces two dressed states $|\pm\rangle_j = (1/\sqrt{(2)})(|g_j\rangle \pm e^{i\Phi_j}|e\rangle_j)$. The qubit cannot go into transitions between different dressed states under the conditions $\Phi_1 = \Phi_2 = \Phi$ and $|A_1 - A_2| >> |J'|$. Then the Hamiltonian (A.10) in the dressed state basis reduces to [134, 140].

$$\hat{H}_{eff} = \frac{1}{2}\hbar J' S_{z1}S_{z2} + \hbar\sum_{j=1,2} A_j S_{zj}. \tag{A.11}$$

Here, $S_zj = |+\rangle_j\langle+|_j - |-\rangle_j\langle-|_j$. If the phases of both the driving fields are reversed right in the middle of the two-qubit interaction time, then the dressed state $|+\rangle_1|+\rangle_2$ evolves to $|++\rangle_t = exp(iJ't/2)|+\rangle_1|+\rangle_2$. At time $\tau = \pi/2J'$, the dressed state become $|++\rangle_\tau = (1/2)(i|\phi^-\rangle + |\phi^+\rangle + i|\psi^-\rangle + |\psi^+\rangle)$. In the computational basis ($|0\rangle$, $|1\rangle$), the state $|++\rangle_\tau$ can be obtained by applying the unitary operator

$$U = \begin{bmatrix} 1 & 0 & 0 & i \\ 0 & 1 & i & 0 \\ 0 & i & 1 & 0 \\ i & 0 & 0 & 1 \end{bmatrix} \tag{A.12}$$

Therefore, in the computational basis the Bell state $|\phi^+\rangle$ is mapped to $|0_1 0_2\rangle$, i.e., $U|0_1 0_2\rangle = |\phi^+\rangle$. Similarly, $|\phi^-\rangle$, $|\psi^+\rangle$, and $|\psi^-\rangle$ are mapped onto $|1_1 1_2\rangle$, $|1_1 0_2\rangle$, $|0_1 1_2\rangle$.

Bibliography

[1] A. Wallraff, D. Schuster, A. Blais *et al. 'Strong coupling of a single photon to a superconducting qubit using circuit quantum electrodynamics'.* Nature **431**, 162–167 (2004).

[2] J. Koch, Terri M. Yu, Jay Gambetta *et al. 'Charge-insensitive qubit design derived from the Cooper pair box'.* Phys. Rev. A **76**, 042319 (2007).

[3] A. Blais, R Huang, A. Wallraff *et al. 'Cavity quantum electrodynamics for superconducting electrical circuits: An architecture for quantum computation'.* Phys. Rev. A **69**, 06232 (2004).

[4] J. Majer, J.M. Chow, J.M. Gambetta *et al. 'Coupling superconducting qubits via a cavity bus'.* Nature **499**, 443–447 (2007).

[5] L. DiCarlo, J. M. Chow, J. M. Gambetta *et al. 'Demonstration of two-qubit algorithms with a superconducting quantum processor'.* Nature **460**, 240–244 (2009).

[6] A. Blais, A. L. Grimsmo, S.M. Girvin and A. Wallraff *'Circuit quantum electrodynamics'.* Rev. Mod. Phys. **93**, 025005 (2021).

[7] A. Blais, J. Gambetta, A. Wallraff *et al. 'Quantum-information processing with circuit quantum electrodynamics'.* Phys. Rev. A **431**, 032329 (2007).

[8] R. J. Schoelkopf and S. M. Girvin *et al. 'Wiring up quantum systems'*. Nature **451**, 664–669 (2008).

[9] Y. Kubo, F. R. Ong, P. Bertet *et al. 'Strong Coupling of a Spin Ensemble to a Superconducting Resonator'*. Phys. Rev. Lett. 105, **105**, 140502 (2010).

[10] Qiong Chen, Jun Wen, W. L. Yang *et al. 'Nonlinear coupling between a nitrogen-vacancy-center ensemble and a superconducting qubit'*. Optics Express **23**, 1615-1626 (2015).

[11] Y. Chu and Simon Gröblacher *'A perspective on hybrid quantum opto- and electromechanical systems'*. Appl. Phys. Lett. **117**, 150503 (2020).

[12] M. Benito and Guido Burkard *'Hybrid superconductor-semiconductor systems for quantum technology'*. Appl. Phys. Lett. **116**, 190502 (2020).

[13] A. A. Clerk, K. W. Lehnert, P. Bertet *et al. 'Hybrid quantum systems with circuit quantum electrodynamics'*. Nature Physics **16**,257–267 (2020).

[14] Nikolai Lauk, Neil Sinclair1, Shabir Barzanjeh *et al. 'Perspectives on quantum transduction'*. Quantum Sci. Technol. **5** 020501 (2020).

[15] J.M. Pirkkalainen, S. U. Cho, Jian Li, G. S. Paraoanu *et al. 'Hybrid circuit cavity quantum electrodynamics with a micromechanical resonator'*. Nature **494**, 211–215 (2013).

[16] F. Lecocq, J. D. Teufel, J. Aumentado and R. W. Simmonds *'Resolving the vacuum fluctuations of an optomechanical system using an artificial atom'*. Nature Physics **11**, 635–639 (2015).

[17] T. A. Palomaki , J. D. Teufel, R. W. Simmonds, and K. W. Lehnert *'Entangling Mechanical Motion with Microwave Fields'*. Science **342**,710-713(2013).

[18] J. D. Teufel, T. Donner, Dale Li *et al. 'Sideband cooling of micromechanical motion to the quantum ground state'*. Nature **475**, 359–363 (2011).

[19] M. D. LaHaye, J. Suh, P. M. Echternach *et al. 'Nanomechanical measurements of a superconducting qubit'*. Nature **459**, 960–964 (2009.

[20] T. Bera, S. Majumder, S. K. Sahu and V. Singh *'Large flux-mediated coupling in hybrid electromechanical system with a transmon qubit'*. Communications Physics **4**,12 (2021).

[21] T. Bera, M. Kandpal1, G. S. Agarwal and V. Singh *'Single-photon induced instabilities in a cavity electromechanical device'*. Nature Communications **15**, 7115 (2024).

[22] I. C. Rodrigues, D. Bothner and G. A. Steele *'Coupling microwave photons to a mechanical resonator using quantum interference'*. Nature Communications **10**, 5359 (2019).

[23] A. Bienfait, K. J. Satzinger, Y. P. Zhong *et al. 'Phonon-mediated quantum state transfer and remote qubit entanglement'*. Science **364**, 368-371, (2019).

[24] R. Manenti, A. F. Kockum, A. Patterson *et al. 'Circuit quantum acoustodynamics with surface acoustic waves'*. Nature Communications **8**, 975 (2017).

[25] Y. Chu, P. Khare, W. H. Renninger, *et al. 'Quantum acoustics with superconducting qubits'*. Science **358**, 199-202 (2017).

[26] A. D. O'Connell, M. Hofheinz, M. Ansmann *et al. 'Quantum ground state and single-phonon control of a mechanical resonator'*. Nature **464**, 697–703 (2010).

[27] U. v. Lüpke, Y. Yang, M. Bild *et al. 'Parity measurement in the strong dispersive regime of circuit quantum acoustodynamics'*. Nature Physics **18**, 794–799 (2022).

[28] E. A. Wollack, A. Y. Cleland, R. G. Gruenke *et al. 'Quantum state preparation and tomography of entangled mechanical resonators'*. Nature **604**, 463–467 (2022).

[29] Y. Chu, P. Kharel, T. Yoon *et al. 'Creation and control of multi-phonon Fock states in a bulk acoustic-wave resonator'*. Nature **563**, 666-670 (2018).

[30] N.R.A. Lee, Y. Guo, A. Y. Cleland *et al. 'Strong Dispersive Coupling Between a Mechanical Resonator and a Fluxonium Superconducting Qubit'*. PRX Quantum **4**, 040342 (2023).

[31] K. J. Satzinger, Y. P. Zhong, H.-S. Chang *et al. 'Quantum control of surface acoustic-wave phonons'*. Nature **563**, 661–665 (2018).

[32] A. Noguchi, R. Yamazaki, Y. Tabuchi *et al. 'Qubit-Assisted Transduction for a Detection of Surface Acoustic Waves near the Quantum Limit'*. Phys. Rev. Lett. **119**, 180505 (2017).

[33] L.R. Sletten, B.A. Moores, J.J. Viennot *et al. 'Resolving Phonon Fock States in a Multimode Cavity with a Double-Slit Qubit'*. Phys. Rev. X **9**, 021056 (2019).

[34] S. Gröblacher, K. Hammerer, M. R. Vanner and M. Aspelmeyer *'Observation of strong coupling between a micromechanical resonator and an optical cavity field'*. Nature **460**, 724–727 (2009).

[35] S. Gröblacher, A. Trubarov, N. Prigge *et al. 'Observation of non-Markovian micromechanical Brownian motion'*. Nature Communications **6**, 7606 (2015).

[36] R. W. Andrews, R. W. Peterson, T. P. Purdy *et al. 'Bidirectional and efficient conversion between microwave and optical light'*. Nature Physics **10**, 321–326 (2014).

[37] O. Černotík and K. Hammerer *'Measurement-induced long-distance entanglement of superconducting qubits using optomechanical transducers'*. Phys. Rev. A **94**, 012340 (2016).

[38] J. Chan, T. P. M. Alegre, A. H. Safavi-Naeini *et al. 'Laser cooling of a nanomechanical oscillator into its quantum ground state'*. Nature **478**, 89–92 (2011).

[39] R. Riedinger, S. Hong, R. A. Norte *et al. 'Non-classical correlations between single photons and phonons from a mechanical oscillator'*. Nature **530**, 313–316 (2016).

[40] I. Marinković, A. Wallucks, R. Riedinger *et al. 'Optomechanical Bell Test'*. Phys. Rev. Lett. **121**, 220404 (2018).

[41] J. D. Cohen, S. M. Meenehan, G. S. MacCabe *et al. 'Phonon counting and intensity interferometry of a nanomechanical resonator'*. Nature **520**, 522–525 (2015).

[42] A. H. Safavi-Naeini, S. Gröblacher, J. T. Hill *et al. 'Squeezed light from a silicon micromechanical resonator'*. Nature **500**, 185–189 (2013).

[43] R. Stockill, M. Forsch, G. Beaudoin *et al. 'Gallium Phosphide as a Piezoelectric Platform for Quantum Optomechanics'*. Phys. Rev. Lett. **123**, 163602 (2019).

[44] K. Schneider, Y. Baumgartner, S. Hönl *et al. 'Optomechanics with one-dimensional gallium phosphide photonic crystal cavities'*. Optica Vol. **6**, 577-584 (2019).

[45] A. Vainsencher, K. J. Satzinger, G. A. Peairs and A. N. Cleland *'Bi-directional conversion between microwave and optical frequencies in a piezoelectric optomechanical device '*. Appl. Phys. Lett. **109**, 033107 (2016).

[46] K. C. Balram, M. I. Davanço, J. D. Song and K. Srinivasan *'Coherent coupling between radiofrequency, optical and acoustic waves in piezo-optomechanical circuits'*. Nature Photonics **10**, 346–352 (2016).

[47] W. Jiang, C. J. Sarabalis, Y. D. Dahmani *et al. 'Efficient bidirectional piezo-optomechanical transduction between microwave and optical frequency'*. Nature Communications **11**, 1166 (2020).

[48] M. Mirhosseini, A. Sipahigil, M. Kalaee and O. Painter *'Superconducting qubit to optical photon transduction'*. Nature **588**, 599–603 (2020).

[49] X. Han, W. Fu, C. Zhong *et al. 'Cavity piezo-mechanics for superconducting-nanophotonic quantum interface'*. Nature Communications**11**, 3237 (2020).

[50] L. Shao, M. Yu, S. Maity *et al. 'Microwave-to-optical conversion using lithium niobate thin-film acoustic resonators'*. Optica **6**1498-1505 (2019).

[51] M. Forsch, R. Stockill, A. Wallucks *et al. 'Microwave-to-optics conversion using a mechanical oscillator in its quantum ground state'*. Nature Physics **16**, 69–74 (2020).

[52] S. Goldstein, Proc. R. Soc. Edinburgh 49, 210 (1929).

[53] G. Blanch, in Handbook of Mathematical Functions, edited by M. Abramowitz and I. A. Stegun Dover, New York (1972)

[54] J. N. L. Connor, T. Uzer, R. A. Marcus, and A. D. Smith, *'Eigenvalues of the Schrödinger equation for a periodic potential with nonperiodic boundary conditions: A uniform semiclassical analysis'* J. Chem. Phys. **80**, 5095 (1984).

[55] M.A. Rol, F. Battistel, F.K. Malinowski *et al. 'Fast, High-Fidelity Conditional-Phase Gate Exploiting Leakage Interference in Weakly Anharmonic Superconducting Qubits'*. Phys. Rev. Lett. **123**, 120502 (2019).

[56] M. Tinkham. *'Introduction to Superconductivity'*, 2nd ed. (Dover Publications, Mineola, NY, (2004)).

[57] M. A. Rol, L. Ciorciaro, F. K. Malinowski *et al. 'Time-domain characterization and correction of on-chip distortion of control pulses in a quantum processor'*. Appl. Phys. Lett. **116**, 054001 (2020).

[58] M.D. Hutchings, J.B. Hertzberg, Y. Liu, N.T. Bronn *et al. 'Tunable Superconducting Qubits with Flux-Independent Coherence'*. Phys. Rev. Applied **8**, 044003 (2017).

[59] J. M. Martinis, S. Nam, J. Aumentado, and C. Urbina *'Rabi Oscillations in a Large Josephson-Junction Qubit'*. Phys. Rev. Lett. **89**, 117901 (2002).

[60] J. E. Mooij, T. P. Orlando, L. Levitov *et al. 'Josephson Persistent-Current Qubit'*. Science **285**, 1036-1039 (1999).

[61] F. Yan, S. Gustavsson, A. Kamal *et al. 'The flux qubit revisited to enhance coherence and reproducibility'*. Phys. Rev. B **75**, 140515 (2007).

[62] J. Q. You, Xuedong Hu, S. Ashhab, and Franco Nori *'Low-decoherence flux qubit'*. Phys. Rev. B **75**, 140515 (2007).

[63] V. E. Manucharyan, J. Koch, L. I. Glazman, and M. H. Devoret *'Fluxonium: Single Cooper-Pair Circuit Free of Charge Offsets'*. Science **326**, 113-116, (2009).

[64] A. Gyenis, P. S. Mundada, A. Di Paolo *et al. 'Experimental Realization of a Protected Superconducting Circuit Derived from the 0–π Qubit'*. PRX Quantum **2**, 010339 (2021).

[65] P. Brooks, A. Kitaev, and J. Preskill *'Protected gates for superconducting qubits'*. Phys. Rev. A **87**, 052306 (2013).

[66] M. Göppl, A. Fragner, M. Baur *et al. 'Coplanar waveguide resonators for circuit quantum electrodynamics'*. J. Appl. Phys. **104**, 113904 (2008).

[67] R. N. Simon. *'Coplanar Waveguide Circuits, Components and Systems'*. Wiley InterScience, New York (2001).

[68] D. M. Pozar. *'Microwave Engineering'*, **4th ed.** John Wiley and Sons, New York (2001).

[69] P. K. Day, H. G. LeDuc, B. A. Mazin *et al. 'A broadband superconducting detector suitable for use in large arrays'*. Nature v**425**, 817–821 (2003).

[70] A. Nersisyan, S. Poletto, N. Alidoust *et al. 'Manufacturing low dissipation superconducting quantum processors'*. 2019 IEEE International Electron Devices Meeting (IEDM), San Francisco, CA, USA, 2019, pp. 31.1.1-31.1.4,.

[71] C. R. H. McRae, H. Wang, J. Gao *et al. 'Materials loss measurements using superconducting microwave resonators'*. Rev. Sci. Instrum. **91**, 091101 (2020).

[72] G. Calusine, A. Melville, W. Woods *et al. 'Analysis and mitigation of interface losses in trenched superconducting coplanar waveguide resonators'*. Appl. Phys. Lett. **112**, 062601 (2018).

[73] C. Wang, C. Axline, Y. Y. Gao *et al. 'Surface participation and dielectric loss in superconducting qubits'*. Appl. Phys. Lett. **107**, 162601 (2015).

[74] J. M. Sage, V. Bolkhovsky, W. D. Oliver *et al. 'Study of loss in superconducting coplanar waveguide resonators'*. J. Appl. Phys. 109, 063915 (2011).

[75] S. Haroche, and J.M. Raimond *'Exploring the Quantum: Atoms, Cavities, and Photons'* (Oxford University Press, New York (2006))

[76] H. Paik, D. I. Schuster, L. S. Bishop *et al. 'Observation of High Coherence in Josephson Junction Qubits Measured in a Three-Dimensional Circuit QED Architecture'*. Phys. Rev. Lett. **107**, 240501 (2011).

[77] S. Kuhr, S. Gleyzes, C. Guerlin *et al. 'Ultrahigh finesse Fabry-Pérot superconducting resonator'*. Appl. Phys. Lett. **90**, 164101 (2007).

[78] A. Romanenko, R. Pilipenko, S. Zorzetti *et al. 'Three-Dimensional Superconducting Resonators at $T < 20mK$ with Photon Lifetimes up to $\tau = 2s$'*. Phys. Rev. Applied 13, 034032 (2020).

[79] C. Rigetti, J. M. Gambetta, S. Poletto *et al. 'Superconducting qubit in a waveguide cavity with a coherence time approaching 0.1 ms'*. Phys. Rev. B **86**, 100506 (2012).

[80] B. T. H. Varcoe, S. Brattke, M. Weidinger and H. Walther *'Preparing pure photon number states of the radiation field'*. Nature **403**, 743–746 (2000).

[81] M.Boissonneault, J. M. Gambetta, and A. Blais *'Dispersive regime of circuit QED: Photon-dependent qubit dephasing and relaxation rates'*. Phys. Rev. A **79**, 013819 (2009).

[82] P. Carbonaro, G. Compagno, F. Persico *'Canonical dressing of atoms by intense radiation fields'*. Physics Letters A **73**, 97-99 (1979).

[83] W. D. Oliver and P. B. Welander *'Materials in superconducting quantum bits'*. MRS Bulletin **38**, 816–825 (2013).

[84] C.W. Gardiner, and P. Zoller. *'Quantum Noise'*, 2nd ed. (Springer, Berlin (1999)).

[85] H.P. Breuer, and F. Petruccione. *' The Theory of Open Quantum Systems'*, (Oxford University Press, New York (2002)).

[86] H.J. Carmichael. *'Statistical Methods in Quantum Optics 1: Master Equations and Fokker-Planck Equations'*, 2nd ed. (Springer, Berlin (2002)).

[87] C. Müller, J. H. Cole and J. Lisenfeld *'Towards understanding two-level-systems in amorphous solids: insights from quantum circuits'*. Rep. Prog. Phys. **82** 124501 (2019).

[88] L. I. Glazman and G. Catelani *'Bogoliubov quasiparticles in superconducting qubits'*. SciPost Phys. Lect. Notes **31** (2021).

[89] J. Gambetta, A. Blais, D. I. Schuster *et al. 'Qubit-photon interactions in a cavity: Measurement-induced dephasing and number splitting'*. Phys. Rev. A **74**, 042318 (2006).

[90] D. I. Schuster, A. Wallraff, A. Blais *et al. 'ac Stark Shift and Dephasing of a Superconducting Qubit Strongly Coupled to a Cavity Field'*. Phys. Rev. Lett. **94**, 123602 (2005).

[91] P. Bertet, I. Chiorescu, G. Burkard *et al. 'Dephasing of a Superconducting Qubit Induced by Photon Noise'*. Phys. Rev. Lett. **95**, 257002 (2005).

[92] E.M. Purcell. *'Spontaneous Emission Probabilities at Radio Frequencies'*, Phys. Rev. 69, 681 (1946)

[93] B. P. Bowen, G. J. Milburn. *'Quantum Optomechanics'*, (Taylor and Francis, (2015))

[94] B. Yurke. *'Input-Output Theory*, (Springer, New York (2004))

[95] I. Martin, A. Shnirman, L. Tian, and P. Zoller *'Ground-state cooling of mechanical resonators'*. Phys. Rev. B **69**, 125339 (2004).

[96] H. J. Carmichael, P. Kochan, and B. C. Sanders *'Photon Correlation Spectroscopy'*. Phys. Rev. Lett. **77**, 631 (1996).

[97] M. Kounalakis, Y. M. Blanter, and G. A. Steele *'Flux-mediated optomechanics with a transmon qubit in the single-photon ultrastrong-coupling regime'*. Phys. Rev. Research **2**, 023335 (2020).

[98] M. Kounalakis, G. E.W. Bauer, and Y. M. Blanter *'Analog Quantum Control of Magnonic Cat States on a Chip by a Superconducting Qubit'*. Phys. Rev. Lett. **129**, 037205 (2022).

[99] D. C. McKay, S. Filipp, A. Mezzacapo *et al. 'Universal Gate for Fixed-Frequency Qubits via a Tunable Bus'*. Phys. Rev. Applied **6**, 064007 (2016).

[100] M. Aspelmeyer, T. J. Kippenberg, and F. Marquardt *'Cavity optomechanics'*. Rev. Mod. Phys. **86**, 1391 (2014).

[101] S. Barzanjeh, A. Xuereb, S. Gröblacher *'Optomechanics for quantum technologies'*. Nature Physics **18**, 15–24 (2022).

[102] Braginsky, V. B., and F. Y. A. Khalili, 1995, *'Quantum Measurements'* (Cambridge University Press, Cambridge, England).

[103] Braginsky, V. B., and A. B. Manukin. Sov. Phys. JETP **25**, 653 (1967)

[104] Braginsky, V. B., A. B. Manukin, and M. Y. Tikhonov, Sov. Phys. JETP **31**, 829 (1970)

[105] A. Dorsel, J. D. McCullen, P. Meystre, E. Vignes, and H. Walther *'Optical Bistability and Mirror Confinement Induced by Radiation Pressure'*. Phys. Rev. Lett. **51**, 1550 (1983).

[106] Y.-D. Wang and A. A. Clerk *'Using dark modes for high-fidelity optomechanical quantum state transfer'*. New J. Phys. **14** 105010 (2012).

[107] C. Zhong, X. Han, and L. Jiang *'Microwave and Optical Entanglement for Quantum Transduction with Electro-Optomechanics'*. Phys. Rev. Applied **18**, 054061 (2022).

[108] R. Hisatomi, A. Osada, Y. Tabuchi *'Bidirectional conversion between microwave and light via ferromagnetic magnons'*. Phys. Rev. B **93**, 174427 (2016).

[109] R. Riedinger, S. Hong, R. A. Norte *et al. 'Non-classical correlations between single photons and phonons from a mechanical oscillator'*. Nature **530**, 313–316 (2016).

[110] D. Vitali, S. Gigan, A. Ferreira *et al. 'Optomechanical Entanglement between a Movable Mirror and a Cavity Field'*. Phys. Rev. Lett. **98**, 030405 (2007).

[111] W.-J. Gu, Z. Yi, L.-H. Sun, and Y. Yan *'Generation of mechanical squeezing and entanglement via mechanical modulations'*. Optics Express **26**, 30773-30785 (2018).

[112] Y. Xia, A.R. Agrawal, C.M. Pluchar *et al. 'Entanglement-enhanced optomechanical sensing'*. Nat. Photon. **17**, 470–477 (2023).

[113] S. G. Hofer, W. Wieczorek, M. Aspelmeyer, and K.s Hammerer *'Quantum entanglement and teleportation in pulsed cavity optomechanics'*. Phys. Rev. A **84**, 052327 (2011).

[114] C. Zhong, Z. Wang, C. Zou *et al. 'Proposal for Heralded Generation and Detection of Entangled Microwave–Optical-Photon Pairs'*. Phys. Rev. Lett. **124**, 010511 (2020).

[115] S. Kotler, G. A. Peterson, E. Shojaee *et al. 'Direct observation of deterministic macroscopic entanglement'*. Science **372**, 622-625(2021).

[116] C. F. Ockeloen-Korppi, E. Damskägg, J.-M. Pirkkalainen *et al. 'Stabilized entanglement of massive mechanical oscillators'*. Nature **556**, 478–482 (2018).

[117] G. S. MacCabe, H. Ren, J. Luo *et al. 'Nano-acoustic resonator with ultralong phonon lifetime'*. Science **370**, 840-843(2020).

[118] M. Bild, M. Fadel, Y. Yang *et al. 'Schrödinger cat states of a 16-microgram mechanical oscillator'*. Science **380**, 274-278 (2023).

[119] D. Radić, S.-J. Choi *et al. 'Nanomechanical cat states generated by a dc voltage-driven Cooper pair box qubit'*. npj Quantum Inf **8**, 74 (2022).

[120] B. Vlastakis, G. Kirchmair, Z. Leghta *et al. 'Deterministically Encoding Quantum Information Using 100-Photon Schrödinger Cat States'*. Science **342**, 607 (2013).

[121] C. Wang , Y. Y. Gao, P. Reinhold *et al. 'A Schrödinger cat living in two boxes'*. Science **352**, 1087-1091(2016).

[122] David J. Wineland *'Nobel Lecture: Superposition, entanglement, and raising Schrödinger's cat'*. Rev. Mod. Phys. **85**, 1103 (2013).

[123] B. Hacker, S. Welte, S. Dais *et al. 'Deterministic creation of entangled atom–light Schrödinger-cat states'*. Nature Photonics **13**, 110 (2019).

[124] A. Ourjoumtsev, R. Tualle-Brouri, J. Laurat and P. Grangier. *'Generating Optical Schrodinger Kittens for Quantum Information Processing'*. Science **312**, 83 (2006).

[125] Z. Wang, Z. Bao, Y. Wu *et al. 'A flying Schrödinger's cat in multipartite entangled states'*. Science advances **8**, 1778 (2022).

[126] M. Tatsuta, Y. Matsuzaki, and A. Shimizu *'Quantum metrology with generalized cat states'*. Phys. Rev. **A** 100, 032318 (2019).

[127] J. Guillaud and M. Mirrahimi *'Repetition Cat Qubits for Fault-Tolerant Quantum Computation'*. Phys. Rev. X **9**, 041053 (2019).

[128] B. Vlastakis, A. Petrenko, N. Ofek *et al. 'Characterizing entanglement of an artificial atom and a cavity cat state with Bell's inequality'*. Nat Commun **6**, 8970 (2015).

[129] B. Hensen, H. Bernien, A. E. Dr´eau *et al. 'Loophole-free Bell inequality violation using electron spins separated by 1.3 kilometres'*. Nature **526**, 682 (2015).

[130] M. Giustina, M. A. M. Versteegh, S. Wengerowsky *et al. 'Significant-Loophole-Free Test of Bell's Theorem with Entangled Photons'*. Phys. Rev. Lett. **115**, 250401 (2015).

[131] L. K. Shalm, E. Meyer-Scott, B. G. Christensen *et al. 'Strong Loophole-Free Test of Local Realism'*. Phys. Rev. Lett. **115**, 250402 (2015).

[132] S. Storz, J. Schar, A. Kulikov *et al. 'Loophole-free Bell inequality violation with superconducting circuits'*. Nature **617**, 265 (2023).

[133] J. F. Clauser, M. A. Horne, A. Shimony, and R. A. Holt *'Proposed Experiment to Test Local Hidden-Variable Theories'*. Phys. Rev. Lett. **23**, 880 (1969).

[134] W. Ning, X.-J. Huang, P.-R. Han *et al. 'Deterministic Entanglement Swapping in a Superconducting Circuit'*. Phys. Rev. Lett. **123**, 060502 (2019).

[135] M. Mastriani *'Simplified entanglement swapping protocol for the quantum Internet'*. Sci Rep **13**, 21998 (2023).

[136] E. Shchukin and P. v. Loock *'Optimal Entanglement Swapping in Quantum Repeaters'*. Phys. Rev. Lett. **128**, 150502 (2022).

[137] N. Sangouard, C. Simon, N. Gisin *et al. 'Quantum repeaters with entangled coherent states'*. JOSA B **27**, A137 (2010).

[138] M. B. Plenio *'Logarithmic Negativity: A Full Entanglement Monotone That is not Convex'*. Phys. Rev. Lett. **95**, 090503 (2005).

[139] G. Vidal and R. F. Werner *'Computable measure of entanglement'*. Phys. Rev. A **65**, 032314 (2002).

[140] Q. Guo, S.-B. Zheng, J. Wang *et al. 'Dephasing-Insensitive Quantum Information Storage and Processing with Superconducting Qubits'*. Phys. Rev. Lett. **121**, 130501 (2018).

[141] P. F. Cohadon, A. Heidmann, and M. Pinard *'Cooling of a Mirror by Radiation Pressure'*. Phys. Rev. Lett. **83**, 3174 (1999).

[142] S. Mancini, D. Vitali, and P. Tombesi, *'Optomechanical Cooling of a Macroscopic Oscillator by Homodyne Feedback'*. Phys. Rev. Lett. **80**, 688 (1998).

[143] D. Kleckner and D. Bouwmeester, *'Sub-kelvin optical cooling of a micromechanical resonator'*. Nature **444**, 75–78 (2006).

[144] T. Corbitt, C. Wipf, T. Bodiya, D. Ottaway *et al. 'Optical Dilution and Feedback Cooling of a Gram-Scale Oscillator to 6.9 mK'*. Phys. Rev. Lett. **99**, 160801 (2007).

[145] M. Poggio, C. L. Degen, H. J. Mamin, and D. Rugar. *'Feedback Cooling of a Cantilever's Fundamental Mode below 5 mK'*. Phys. Rev. Lett. **99**, 017201 (2007).

[146] S. Gigan, H. R. Böhm, M. Paternostro *et al. 'Self-cooling of a micromirror by radiation pressure'*. Nature **444**, 67–70 (2006).

[147] O. Arcizet, P. F. Cohadon, T. Briant *et al. 'Radiation-pressure cooling and optomechanical instability of a micromirror'*. Nature **444**, 71–74 (2006).

[148] A. Schliesser, R. Rivière, G. Anetsberger *et al. 'Resolved-sideband cooling of a micromechanical oscillator'*. Nature Phys **4**, 415–419 (2008).

[149] S. Gröblacher, J. B. Hertzberg, M. R. Vanner *et al.* *'Demonstration of an ultracold micro-optomechanical oscillator in a cryogenic cavity'*. Nature Phys **5**, 485–488 (2009).

[150] Y. S. Park and H. Wang *'Resolved-sideband and cryogenic cooling of an optomechanical resonator'*. Nature Phys. **5**, 489 (2009)..

[151] A. Schliesser, O. Arcizet, R. Rivere *et al.* *'Resolved-sideband cooling and position measurement of a micromechanical oscillator close to the Heisenberg uncertainty limit'*. Nature Phys. **5**, 509 (2009).

[152] J. Hauss, A. Fedorov, S. André *et al.* *'Dissipation in circuit quantum electrodynamics: lasing and cooling of a low-frequency oscillator'*. New J. Phys. **10**, 095018 (2008).

[153] K. Jaehne, K. Hammerer and M. Wallquist *'Ground-state cooling of a nanomechanical resonator via a Cooper-pair box qubit'*. New J. Phys. **10**, 095019 (2008).

[154] I. Wilson-Rae, N. Nooshi, W. Zwerger, and T. J. Kippenberg *'Theory of Ground State Cooling of a Mechanical Oscillator Using Dynamical Backaction'*. Phys. Rev. Lett. **99**, 093901 (2007).

[155] Robert Zwanzig *'On the identity of three generalized master equations'*. Physica **30**, 1109 (1964).

[156] M. Kounalakis, Y. M. Blanter, and G. A. Steele *'Sisyphus cooling and amplification by a superconducting qubit'*. npj Quantum Inf **5**, 100 (2019).

[157] J.J. Viennot, X. Ma, and K.W. Lehnert *'Phonon-Number-Sensitive Electromechanics'*. Phys. Rev. Lett. **121**, 183601 (2018).

[158] Y.-C. Liu, Y.-F. Xiao, X. Luan, and C. W. Wong *'Dynamic Dissipative Cooling of a Mechanical Resonator in Strong Coupling Optomechanics'*. Phys. Rev. Lett. **110**, 153606 (2013).

[159] S. H. Strogatz, *Sync: The Emerging Science of Spontaneous Order* (Penguin Books Limited, 2004).

[160] H. M. Oliveira and L. V. Melo, *'Huygens synchronization of two clocks'*. Sci Rep **5**, 11548 (2015).

[161] Tony E. Lee and H. R. Sadeghpour, *'Quantum Synchronization of Quantum van der Pol Oscillators with Trapped Ions'*. Phys. Rev. Lett. **111**, 234101 (2013).

[162] M. R. Hush, W. Li, S. Genway *et al. 'Spin correlations as a probe of quantum synchronization in trapped-ion phonon lasers'*. Phys. Rev. A **91**, 061401(R) (2015).

[163] S. Walter, A. Nunnenkamp, and C. Bruder, *'Quantum synchronization of two Van der Pol oscillators'*. Ann. Phys. **527**, 131 (2015).

[164] N. L¨orch, E. Amitai, A. Nunnenkamp, and C. Bruder, *'Genuine Quantum Signatures in Synchronization of Anharmonic Self-Oscillators'*. Phys. Rev. Lett. **117**, 073601 (2016)

[165] W. Li, F. Zhang, C. Li, and H. Song, *'Quantum synchronization in a star-type cavity QED network'*. Sci. Numer. Simulat. **42**, 121 (2017).

[166] M. Koppenh¨ofer and A. Roulet, *'Optimal synchronization deep in the quantum regime: Resource and fundamental limit'*. Phys. Rev. A **99**, 043804 (2019).

[167] M. Koppenh¨ofer, C. Bruder, and A. Roulet, *'Quantum synchronization on the IBM Q system'*. Phys. Rev. Research **2**, 023026 (2020).

[168] O. V. Zhirov and D. L. Shepelyansky, *'Synchronization and Bistability of a Qubit Coupled to a Driven Dissipative Oscillator'*. Phys. Rev. Lett. **100**, 014101 (2008).

[169] E. Amitai, N. L¨orch, A. Nunnenkamp, S. Walter, and C. Bruder, *'Synchronization of an optomechanical system to an external drive'*. Phys. Rev. A 95, 053858 (2017).

[170] Todd A. Brun, *'A simple model of quantum trajectories'*. Am. J. Phys. **70**, 719–737 (2002).

[171] J. R. Johansson, P. D. Nation, and F. Nori, *'QuTiP: An open-source Python framework for the dynamics of open quantum systems'*. Comput. Phys. Commun **183**, 1760 (2012).

[172] J. R. Johansson, P. D. Nation, and F. Nori, *'QuTiP 2: A Python framework for the dynamics of open quantum systems'*. Comput. Phys. Commun 184, 1234 (2013).

[173] O. V. Zhirov and D. L. Shepelyansky, *'Quantum synchronization and entanglement of two qubits coupled to a driven dissipative resonator'*. Phys. Rev. **B** 80, 014519 (2009).

[174] S. Krastanov, H. Raniwala, J. Holzgrafe *et al. 'Optically Heralded Entanglement of Superconducting Systems in Quantum Networks'*. Phys. Rev. Lett. **127**, 040503 (2021).

[175] G. Martin, MIT Technology Review (2019).

[176] M. Brooks, MIT Technology Review (2023).

[177] J. Gambetta, IBM Blog (2022).

[178] Z. Kuan, T. Jayne, Z. Xiang *et al. 'Modular quantum computation in a trapped ion system'*. Nat Commun **10**, 4692 (2019).

[179] C. Monroe, R. Raussendorf, A. Ruthven *et al. 'Large-scale modular quantum-computer architecture with atomic memory and photonic interconnects'*. Phys. Rev. A **89**, 0223172 (2014).

[180] M. J. Weaver, P. Duivestein, A. C. Bernasconi *et al. 'An integrated microwave-to-optics interface for scalable quantum computing'*. Nat. Nanotechnol. **19**, 166–172 (2024).

[181] Srujan Meesala, Steven Wood, David Lake *et al. 'Non-classical microwave–optical photon pair generation with a chip-scale transducer'*. Nat. Phys. **20**, 871–877 (2024).

[182] J. Bochmann, A. Vainsencher, D. D. Awschalom and A. N. Cleland *'Nanomechanical coupling between microwave and optical photons'*. Nature Phys **9**, 712–716 (2013).

[183] G. Arnold, M. Wulf, S. Barzanjeh *et al. 'Converting microwave and telecom photons with a silicon photonic nanomechanical interface'*. Nat Commun **11**, 4460 (2020).

[184] Sh. Barzanjeh, D. Vitali, P. Tombesi, and G. J. Milburn *'Entangling optical and microwave cavity modes by means of a nanomechanical resonator'*. Phys. Rev. A 84, 042342 (2011).

[185] Y.-D. Wang and A. A. Clerk *'Using Interference for High Fidelity Quantum State Transfer in Optomechanics'*. Phys. Rev. Lett. **108**, 153603 (2012).

[186] L. Tian, *'Optoelectromechanical transducer: Reversible conversion between microwave and optical photons'*, (2014) by WILEY-VCH Verlag GmbH and Co. KGaA, Weinheim

[187] T. Blésin, H. Tian, S. A. Bhave, and T. J. Kippenberg, *'Quantum coherent microwave-optical transduction using high-overtone bulk acoustic resonances'*, Phys. Rev. A **104**, 052601 (2021)

[188] N. J. Lambert, A. Rueda, F. Sedlmeir, and H. G. L. Schwefel, *'Coherent Conversion Between Microwave and Optical Photons—An Overview of Physical Implementations'*, (2019) Published by WILEY-VCH Verlag GmbH and Co. KGaA, Weinheim